Multiphase Modeling of a Flowing Electrolyte – Direct Methanol Fuel Cell

by

David Ouellette

A thesis submitted to the Faculty of Graduate Studies and Research

in partial fulfillment of the requirements for the degree of

Doctor of Philosophy

in

Mechanical Engineering

Ottawa-Carleton Institute for Mechanical and Aerospace Engineering

Department of Mechanical and Aerospace Engineering

Carleton University

Ottawa, Ontario, Canada

December, 2015

The undersigned hereby recommends to the

Faculty of Graduate Studies and Research

acceptance of the thesis

Multiphase Modeling of a Flowing Electrolyte – Direct Methanol Fuel Cell

submitted by **David Ouellette**

in partial fulfillment of the requirements for the degree of

Doctor of Philosophy

Dr. Edgar A. Matida, Co-supervisor

Dr. Cynthia A. Cruickshank, Co-supervisor

Dr. Metin I. Yaras, Chair,
Department of Mechanical and Aerospace Engineering

Ottawa-Carleton Institute for Mechanical and Aerospace Engineering

Department of Mechanical and Aerospace Engineering

Carleton University

December, 2015

Abstract

Direct methanol fuel cells (DMFCs) are considered one of the leading contenders for low power applications due to their energy dense, liquid fuel as well as low greenhouse gas emissions. However, DMFCs have lower than predicted performance due to methanol crossover. One proposed solution is to allow a liquid electrolyte, such as diluted sulfuric acid, to flow between the anode and cathode, thereby removing any methanol that attempts to crossover to the cathode. The corresponding fuel cell is named the flowing electrolyte - direct methanol fuel cell, or FE-DMFC. So far few researchers have examined the effectiveness of this fuel cell and none have explored the multiphase flow within the membrane electrode assembly (MEA) of this fuel cell.

In this study, the well-known Multiphase Mixture Model (MMM) was improved with a new single domain approach which was used to model the flow behaviour and performance of the FE-DMFC. Unlike the existing methods, the proposed model only requires the mixture variables, thereby removing the requirement for information about the gaseous state, when attempting to couple the porous and electrolyte layers together. Furthermore, the model's formulation gives the capability to resolve liquid saturation jumps in a single domain manner. The proposed approach is sufficiently flexible that it could be applied to other modeling methods, such as the Multi-Fluid Model (MFM). The corresponding derivation for the MFM is provided. The fidelity of the improved MMM is examined through 3 test cases, which include a comparison to: the analytical liquid saturation jump solution, the analytical single phase solution for the FE-DMFC, and to in-house FE-DMFC experimental

data. The numerical model was shown to be capable of accurately reproducing all three test cases.

To understand the FE-DMFC's underlying physics, the numerical model was applied under baseline operating conditions, and a series of parametric studies were conducted to understand the effect that: the anode and cathode membrane (AM and CM, respectively) thicknesses and the flowing electrolyte channel's (FEC) porosity and thickness each have on the fuel cell's performance. The findings of the parametric study were used to provide recommendations on conditions which yield maximum power density and minimal methanol and water crossover. The results from the baseline study suggest that the FE-DMFC is capable of effectively reducing methanol crossover by at least 20 fold, when compared to the DMFC. However it was found that the back pressure within the FEC is an important feature to consider, as this can cause the bulk fluid to flow from the FEC to the anode and cathode compartments, causing a counterflow condition. Although this aids in reducing methanol crossover even further, it was found that the anode activation polarization also increased, thereby reducing the fuel cell's performance. The results from the parametric study suggest that a thin AM and thick CM arrangement should be used; on the order of 88.9 μm and 177.8 μm respectively, corresponding to Nafion® 1135 and 117 membranes respectively; which is consistent with trends found in previous experimental studies. The results also suggest that a fully open FEC (porosity of one) will provide the greatest performance. Although this finding contradicts existing experimental data, considerations such as the choice of catalyst layer wettability and back pressure within the FEC are provided to achieve a membraneless FE-DMFC with a fully open FEC.

To my mother and late father, Pierrette and Denis, and to my older but little sisters, Céline and Sarah, for a lifetime of love, support and encouragement.

Acknowledgments

First and foremost, I would like to thank my supervisors, Dr. Edgar Matida and Dr. Cynthia Ann Cruickshank, for giving me the opportunity to work on this project. Their patience, support and guidance towards my work and their open door policy are greatly appreciated. Whenever we met, they always displayed enormous enthusiasm and passion towards teaching and research and I found it very contagious. I would also like to thank Dr. Feridun Hamdullahpur for his support and generosity in the initial years of my work and Dr. Glenn McRae for his invaluable input and for our many fruitful discussions in the area of electrochemistry. We would frequently lose track of time during these discussions. Over the years, he has been an incredible wealth of information in seemingly everything. I would also like to thank the technologists and machinists at Carleton University for their help and guidance in my experimental work. As well as Neil McFadyen for his help in giving me access to the computational resources on campus and for his technical support.

I would also like to extend a special thanks to my friend and colleague Dr. Can Ozgur Colpan from Dokuz Eylül University. His patience, invaluable guidance and expertise in fuel cell modeling helped make this work possible. I would not be where I am today without his help. I would also like to extend my thanks to the members of the Fuel Cell Energy Systems Laboratory, both past and present, for their advice and discussions on fuel cell modeling and experimentation. This includes: David Chan, Eric Duivesteyn, Yashar Kablou, Prameela Karumanchi and Nasim Sabet-Sharghri. I wish you all the very best in your undoubtedly bright futures. I would also like to thank my friends and past and present

lab mates: Christopher Baldwin, Sébastien Brideau, Jayson Bursill, Jenny Chu, Ryan Dickinson, Nina Dmytrenko, Phillip Droulliard, Ifaz Haider, Kenny Lee Slew, Mike Miller, Patrice Pinel, John Polansky, and Adam Wills for all their help and advice concerning my experimental and modeling work. They all helped me retain my sanity (or what's left of it) by periodically dragging me away from my work for a tea break.

I also thank the Ontario Centres of Excellence (OCE), Natural Sciences and Engineering Research Council of Canada (NSERC) and the Ontario Graduate Scholarship (OGS) for their financial support. Without their contributions, this work would not have been possible.

Table of Contents

List of Tables

List of Figures

Nomenclature

Abbreviations

ABL	Anode Backing Layer
ACL	Anode Catalyst Layer
AFC	Anode Fuel Channel
AM	Anode Membrane
CAC	Cathode Air Channel
CBL	Cathode Backing Layer
CCL	Cathode Catalyst Layer
CM	Cathode Membrane
DMFC	Direct Methanol Fuel Cell
EOD	Electro-osmotic Drag
FE-DMFC	Flowing Electrolyte – Direct Methanol Fuel Cell
FE	Flowing Electrolyte
FEC	Flowing Electrolyte Channel
MEA	Membrane Electrode Assembly

MFM	Multi-Fluid Model
MMM	Multiphase Mixture Model
MOR	Methanol Oxidation Reaction
NIST	National Institute of Standards and Technology
OCV	Open Circuit Voltage
ORR	Oxygen Reduction Reaction
Pt	Platinum
Ru	Ruthenium
SEM	Scanning Electron Micrography
TEM	Transmission Electron Micrography

Variable

A	Active Area	m^2
a	Activity	-
B_x	Bias Error of Variable x	-
C	Concentration	mol m^{-3}
D	Diffusion Coefficient	m^2 s^{-1}
d	Pore Diameter	m
E	Effectiveness Factor	-

F	Faraday's Constant (96 485)	C mol^{-1}
f	Mass Fraction/Interpolation Factor	-/-
g_f	Gibb's Free Energy of Formation	J mol^{-1}
h	Mass Transfer Resistance	s m^{-3}
I	Current	A
i	Current Density	A m^{-2}
i_{lim}	Limiting Current Density	A m^{-2}
J	Leverett J-Function	-
j	Volumetric Current Density	A m^{-3}
j_l	Capillary Diffusion Flux for the Liquid Phase	kg m^{-2} s^{-1}
k_c	Agglomerate Reaction Rate	s^{-1}
k_H	Henry's Constant	-
k_r	Relative Permeability	-
K	Absolute Permeability	m^2
K_a	Reaction Constant for Methanol Oxidation	mol m^{-3}
L	Length	m
M	Molecular Weight	kg mol^{-1}
m''	Mass Loading	kg m^{-2}
$\dot{N}$	Molar Flow Rate	mol s^{-1}

$\dot{N}''$	Molar Flux	mol m^{-2} s^{-1}
n	Number of Electrons Involved in Reaction	-
n_{agg}	Agglomerate Density	m^{-3}
n_d	Coefficient of Electro-osmotic Drag	-
P	Pressure	Pa
Pe	Peclet Number	-
R	Radius of Whole Agglomerate / Electrical Resistance	m / Ω m^2
$\bar{R}$	Universal Gas Constant (8.3144)	J mol^{-1} K^{-1}
R_x	Random Error of Variable x	-
Re	Reynolds Number	-
r_{agg}	Agglomerate Nucleus Radius	m
S_{gen}	Consumption/Generation Flux	kg m^{-3} s^{-1}
S_{gen}^k	Consumption/Generation Flux of Species k	mol m^{-3} s^{-1}
S_{trans}	Transport Source Term	kg m^{-3} s^{-1}
s	Liquid Saturation	-
t	Thickness	m
$t_{\nu,95\%}$	Student t-Distribution Factor at 95% Confidence	-
T	Temperature	K
u	Fluid Velocity in the x-Direction	m s^{-1}

V_{cell}	Cell Voltage	V
v	Fluid Velocity in the y-Direction	m s^{-1}
$\dot{Q}$	Volumetric Flowing Electrolyte Flow Rate	m^3 s^{-1}
x	Position in the x-direction / Mole fraction	m / -
y	Position in the y-direction	m

Greeks Letters

α	Transfer Coefficient / Water Transport Coefficient	-
γ	Advection Correction Factor	-
Γ	General Diffusion Coefficient	-
δ	Thickness / Pulse Diffusion Index	m / -
ε	Porosity / Volume Fraction	-
η	Overpotential	V
η_{fuel}	Fuel Efficiency	-
θ_c	Contact Angle	$^\circ$
ϑ	Pulse Function	-
Θ	Objective Function	-
κ	Electrical Conductance	S m^{-1}
λ	Mobility	-

λ_{wc}	Water Content	-
ν	Kinematic Viscosity / Degrees of Freedom	$m^2\ s^{-1}$ / -
ξ	Agglomerate Correction Factor	-
ρ	Density	$kg\ m^{-3}$
σ	Surface Tension	$N\ m^{-2}$
τ	Tortuosity	-
Φ	Electrical or Ionic Potential	V
ϕ	Arbitrary Variable	-
ϕ_R	Thiele's Modulus at Position R	-
ψ	Young-Laplace Coefficient	Pa
ω	Relaxation Factor	-

Subscript/Superscript

ABL	Anode Backing Layer
ACL	Anode Catalyst Layer
AFC	Anode Fuel Channel
AM	Anode Membrane
a	Anode
act	Activation Polarization

CAC	Cathode Air Channel
CBL	Cathode Backing Layer
CCL	Cathode Catalyst Layer
CM	Cathode Membrane
c	Cathode
cap	Capillary
$conc$	Concentration Polarization
$contact$	Contact Resistance
e	Electrolyte Phase
eff	Effective Value
eq	Equilibrium Value
FEC	Flowing Electrolyte Channel
g	Gaseous State
H_2O	Water
in	Inlet
k	Species k
l	Liquid State
lg	Two-phase Condition
$MeOH$	Methanol

O_2	Oxygen
o	Intrinsic Property
$ohmic$	Ohmic Polarization
ref	Reference Value
rev	Reversible Conditions
s	Solid Phase
$xover$	Crossover
-	Averaged value
τ	Tortuosity

Chapter 1

Background

1.1 Flowing Electrolyte – Direct Methanol Fuel Cells

Low temperature fuel cells have shown great promise toward auxillary power, portable and transportation applications; in particular, hydrogen and methanol fuel cells [1,2]. Hydrogen is the ideal fuel for these applications due to its high energy density (119.9 MJ kg^{-1} at 300 bar), abundance and zero greenhouse gas emissions during operation [1]. This type of fuel cell is commonly known as the proton exchange membrane fuel cell or PEMFC. However, the challenges associated with the storage, transportation and distribution of hydrogen have hampered the growth of this type of fuel cell. A promising alternative fuel is methanol. Under standard conditions, methanol is in a liquid state, which mitigates the challenges associated with fuel storage. Methanol yields an energy density that is approximately 26× higher than hydrogen after consideration of storage efficiency. This corresponds to an energy density of 18.9 MJ kg^{-1} for methanol and 0.72 MJ kg^{-1} for hydrogen [1]. In addition, methanol is inexpensive, simple and potentially sustainable to produce, and the infrastructure to support methanol is already present. This type of fuel cell is commonly known as the direct methanol fuel cell or DMFC.

Unfortunately, DMFCs suffer from a phenomena known as 'methanol crossover', which

will be discussed in more detail in Section 1.4.2. It has been estimated that the losses associated with methanol crossover account for 30% of all losses within this fuel cell [3]. As a mitigation strategy, this fuel cell has been designed to operate with a decreased inlet methanol concentration, typically less than 2 mol L^{-1} [4]; thus severely decreasing the DMFC's energy density. Hence the reduction of methanol crossover has been a major topic of research in literature. One method to potentially solve this challenge is to use the flowing electrolyte concept [5], where the corresponding fuel cell is known as a flowing electrolyte – direct methanol fuel cell, or FE-DMFC. In the following section, the operating principles and the individual components within the FE-DMFC will be discussed.

1.2 Operating Principles

The FE-DMFC is an electrochemical device which utilizes methanol as a fuel and oxygen or air as an oxidant to generate electricity [1, 6]. A schematic of a typical FE-DMFC is shown in Figure 1.1.

The generated electricity is achieved by supplying diluted methanol in the anode fuel channel (AFC), which is then transported through a porous carbon backing layer (ABL) and to a catalyst layer (ACL) – which is typically composed of platinum and ruthenium (Pt and Ru) [7, 8]. The supplied diluted methanol then oxidizes in the ACL, which releases electrons and protons, with carbon dioxide as the by-product. The completed anode reaction is shown below the ACL, in Figure 1.1. The protons are transported through the anode and cathode proton conducting yet electron insulating membranes (AM and CM) and flowing electrolyte channel (FEC), which is typically composed of diluted sulfuric acid. The electrons on the other hand, cannot conduct through the membranes and are therefore forced back through the ACL, ABL and AFC to travel around an external circuit to be used towards useful electrical work. The external circuit is connected to the anode and cathode current

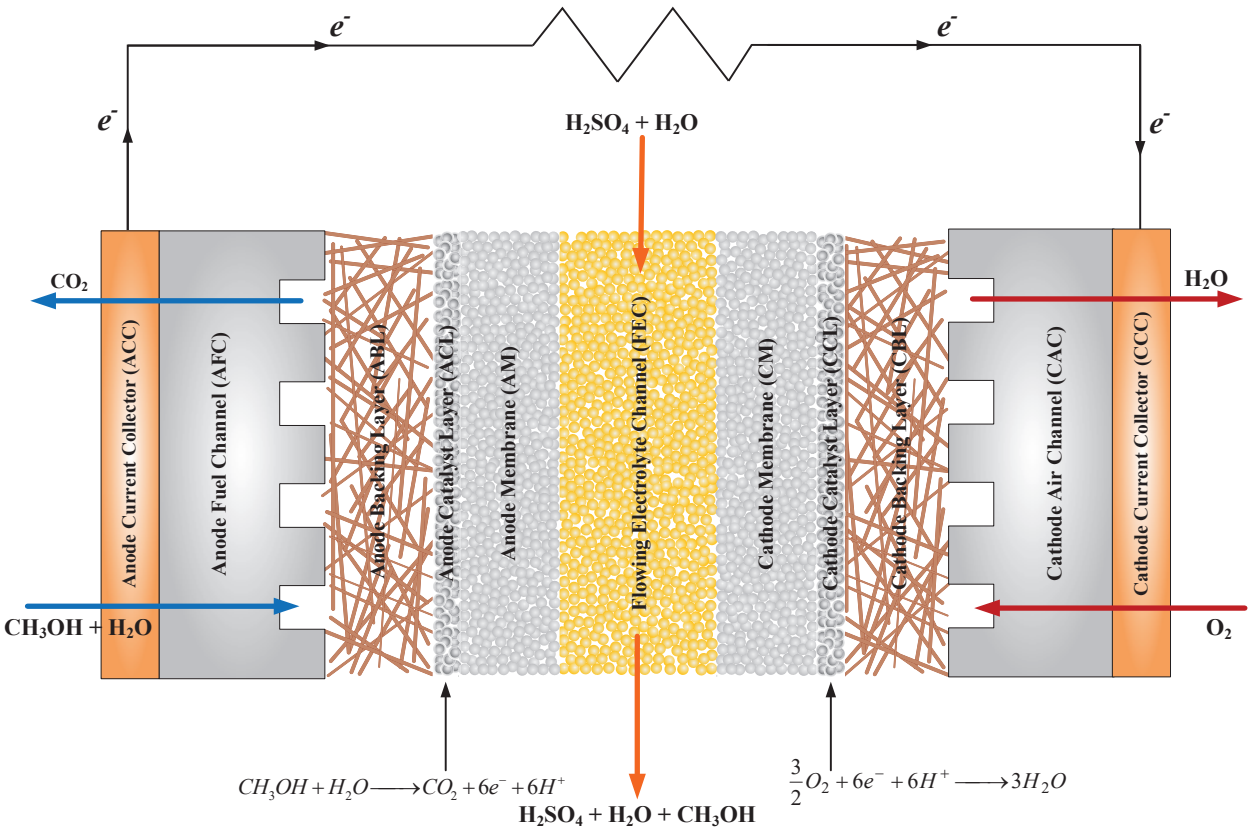

Figure 1.1: Schematic of a flowing electrolyte-direct methanol fuel cell (FE-DMFC).

collectors (ACC and CCC), as shown in Figure 1.1. On the cathode, oxygen is supplied to the cathode air channel (CAC) and is transported through a porous carbon backing layer (CBL) to the catalyst layer (CCL), which is typically composed of Pt. Here, the supplied oxygen is reduced with the provided electrons and protons from the anode reaction, to form water. The anode, cathode and overall reactions are summarized below.

Anode:	$CH_3OH + H_2O$	$\longrightarrow$	$CO_2 + 6H^+ + 6e^-$	$E_a^{eq} = -0.03$ V
Cathode:	$\frac{3}{2}O_2 + 6H^+ + 6e^-$	$\longrightarrow$	$3H_2O$	$E_c^{eq} = 1.24$ V
Overall:	$CH_3OH + \frac{3}{2}O_2$	$\longrightarrow$	$CO_2 + 2H_2O$	$E^{eq} = 1.21$ V

Since at a given operating point, not all methanol is consumed in the ACL, the remaining methanol is transported through the AM, FEC and CM, and reacts within the CCL. This causes methanol to rapidly oxidize in an oxygen rich environment, also causing the released

electrons and protons to be readily consumed by the surrounding oxygen. Since these electrons do not travel through the external load, this results in lost work. This effect is known as methanol crossover and will be discussed in more detail in Section 1.4.2. However, the FEC in this fuel cell is designed to act as a methanol barrier, by removing any crossed over methanol, thus protecting the CCL. The addition of the FEC could potentially allow for less expensive membranes to be used, if the FEC is able to effectively remove methanol from the fuel cell. The removed methanol could then be separated and supplied to the anode inlet to be recycled [5], or sent to a specialized fuel cell that could use the liquid electrolyte-methanol mixture as fuel [9]. As will be seen in Sections 1.6 and 1.7, little is known about how the FEC affects the performance of the FE-DMFC. As such the focus of this dissertation will be on understanding how this fuel cell functions, and to lay a foundation for the fuel cell community, such that future work could focus on the optimization of the fuel cell's structure and design.

It should be noted that the DMFC, without the FE, only has one membrane and does not have the FEC. This configuration is also true for the PEMFC, where in this case, hydrogen is used as fuel instead of methanol. Since individual components within the FE-DMFC were mentioned, the next section will be devoted to describing their structure and physical use.

1.3 FE–DMFC Components

As can be seen in Figure 1.1, the FE-DMFC is composed of an anode and cathode backing layer (ABL and CBL), an anode and cathode catalyst layer (ACL and CCL), two membranes one for the anode compartment (AM) and one for the cathode (CM), and a flowing electrolyte channel (FEC). Each of these components and their functions will be discussed in the following sections, beginning with the backing layers (BLs).

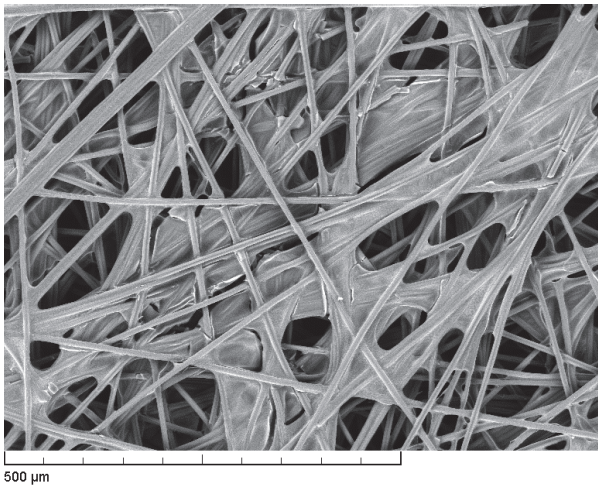

Figure 1.2: In-house SEM micrograph of carbon paper (Toray® TGP-H-090) at 200× magnification.

1.3.1 Backing Layers

The backing layers are a porous layer, typically composed of carbon, that allows the uniform distribution of fuel and oxidant to the catalyst layers. Often times, a hydrophobic material, such as Teflon®, is impregnated into the BLs to help manage the rate of transport of reactants. This in turn helps to reduce the rate of methanol crossover, and the removal of liquid water from the cathode [4]. Under a scanning electron microscope (SEM), shown in Figure 1.2, the carbon paper is shown to be a fibrous porous media. The webbing between fibers is the impregnated Teflon®.

1.3.2 Catalyst Layers

The catalyst layers are where the methanol oxidation reaction (MOR) in the anode and the oxygen reduction reaction (ORR) in the cathode occur. In FE-DMFCs, the catalysts are typically composed of a platinum-ruthenium (Pt-Ru) binary catalyst for the anode and Pt catalyst for the cathode. The binary catalyst allows for improved catalytic activity, while the Ru helps to protect the Pt from impurities and intermediate reactants from being absorbed onto its surface [10, 11], which is known as catalyst poisoning. Like the BLs, the CLs are sometimes impregnated with Teflon® to increase the layer's hydrophobicity [4]. Figure 1.3a

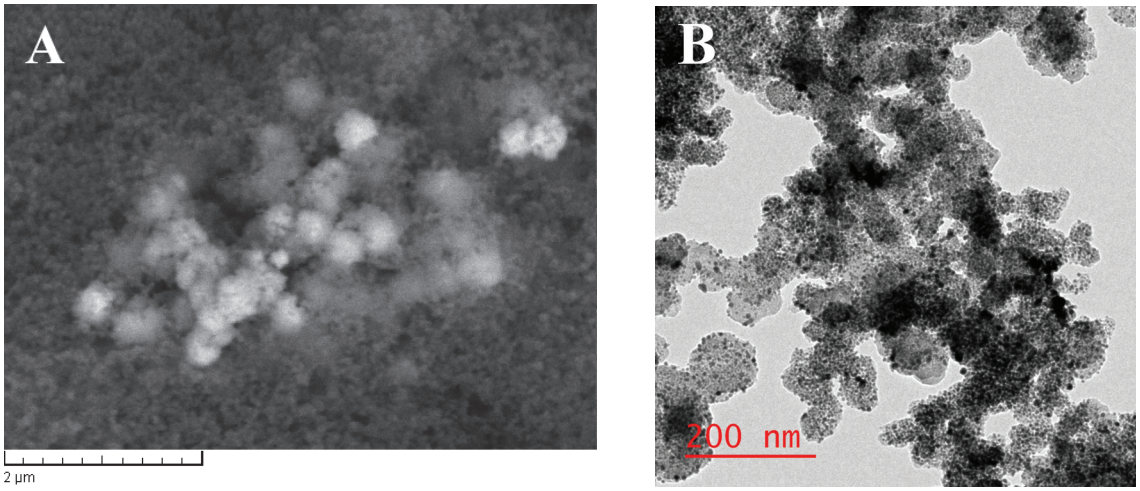

Figure 1.3: In-house micrographs of the cathode catalyst structure. (a) Shows the meso-scale structure observed through SEM, whereas (b) shows the nano-scale structure which forms the meso-scale structure, which was observed through TEM.

displays a SEM micrograph of the surface of the CL applied to a Toray® TGP-H-090 backing layer. As can be seen in the SEM micrograph, shown in Figure 1.2a, it can be seen that the catalyst agglomerates into spherical pellets. Each pellet is further composed of smaller agglomerates of composed of carbon, Nafion and catalyst, as shown in Figure 1.3b.

1.3.3 Membranes

The membranes used (most commonly Nafion®) allow the passage of protons from the ACL to the CCL, while forcing electrons to flow around an external circuit to power an external load [12]. As such, this layer must be proton conducting but not electron conducting. Furthermore, the membranes act as a separator for the fuel, oxidant and liquid electrolyte; preventing methanol, water and oxygen from crossing over and reacting on the opposite side of the fuel cell. This membrane uses polytetrafluoroethylene (PTFE) as the structural support and several side chains typically terminated with sulfonic acid groups (SO_3^-) to promote proton conductivity [13]. Figure 1.4 displays a schematic of the Nafion® structure.

Since these sulfonic acid groups (SO_3^-) are negatively charged, the protons generated

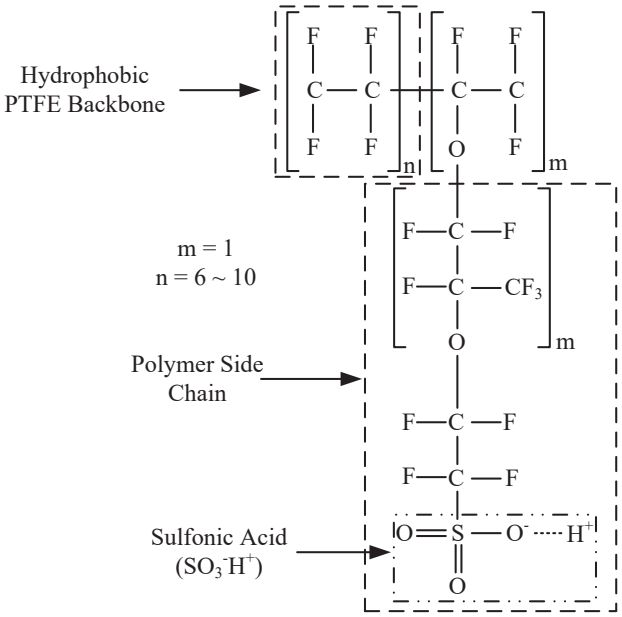

Figure 1.4: Chemical composition of a Nafion® membrane. Adapted from Jiao and Li [13].

from the MOR on the anode become attracted to the sulfonic acid groups and are thus transported to the cathode. On the other hand, due to Nafion®'s very low electronic conductivity compared to the carbon in the BLs and CLs, the electrons generated within the anode are forced around the external circuit, to the cathode. This creates a proton conducting yet electron insulating membrane [13].

The transport of protons through Nafion® occur in multiple modes. The first is related to the proton's weak attraction to the membrane's sulfonic acid groups, which allow protons to easily bond, detach and bond again with the next nearest sulfonic acid group. This proton 'hopping' motion, from one sulfonic acid group to the next, is known as the Grotthuss mechanism [13, 14]. The other mode of transport is caused by protons bonding with water molecules to create a hydronium-type ion, in the form of $(H_2O)_mH^+$, and is carried with the flow of water within the membrane. This transport mechanism is known as the vehicular transport mechanism. The third mode of transport is through electro-osmosis, which occurs due to the presence of an electric field between the anode and cathode. This causes the protons to migrate from the anode to the cathode.

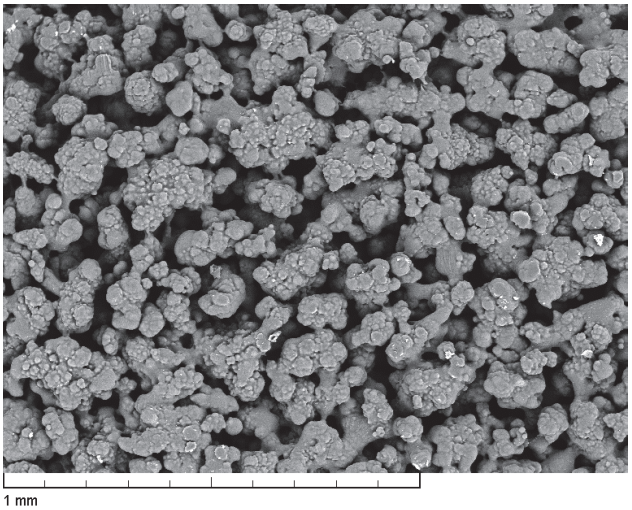

Figure 1.5: In-house SEM micrograph of a 1.57 mm porous polyethylene spacer used for the FEC at 100× magnification.

1.3.4 Flowing Electrolyte Channel

The flowing electrolyte channel (FEC) is the space between the AM and CM for the liquid electrolyte. The original concept for this channel was simply an open space between the membranes [5]. However, in Sabet-Sharghri *et al.*'s work [15], they demonstrated that an open channel design for the FEC was not practical for use, since the membranes can bulge and come in contact during operation; thus hindering the flow of the electrolyte and decrease the performance of the fuel cell. Instead, they proposed the use of a porous spacer, composed of polyethylene. A SEM image of this layer is shown in Figure 1.5.

1.4 Performance Characterization

DMFC performance is typically characterized by measuring the maximum current and power densities, as well as all loss mechanisms, which include: the activation, concentration and ohmic polarizations, as well as methanol and water crossover fluxes. The simplest and most frequently adopted approach, to qualitatively compare fuel cell performance, is through use of polarization curves. This method will be discussed next sub-section, while the remaining loss mechanisms will be discussed after.

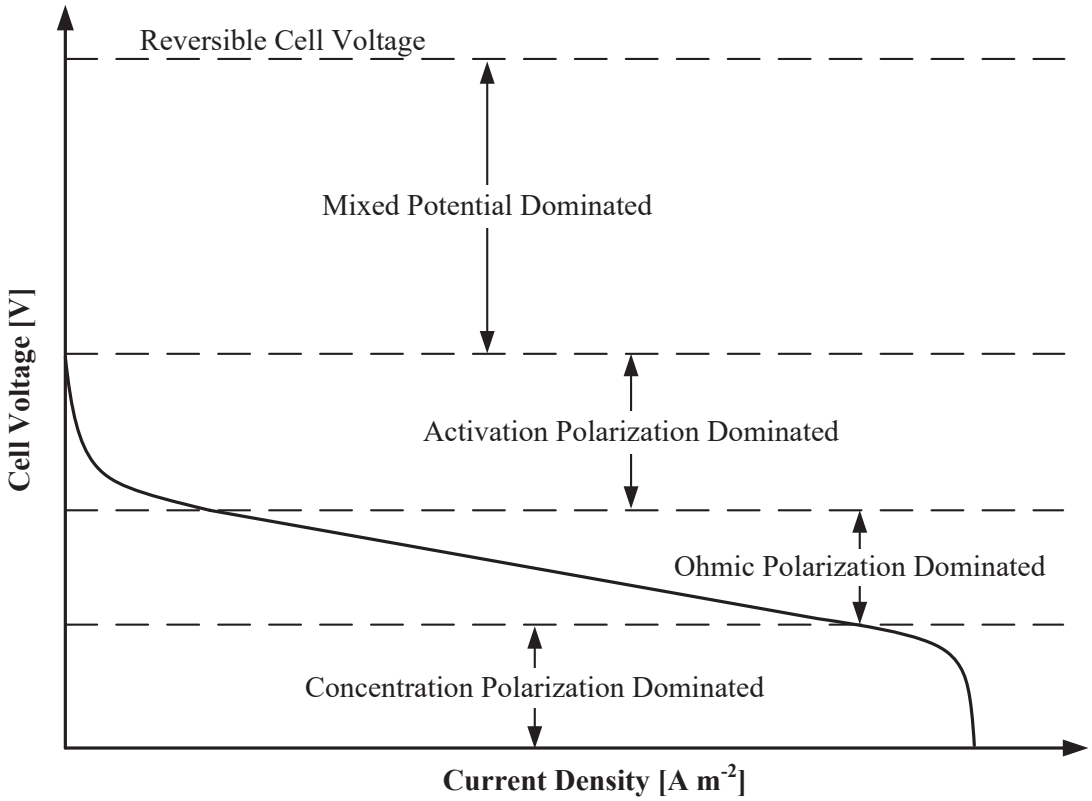

Figure 1.6: Schematic of a typical fuel cell polarization curve, and the regions dominated by each loss mechanism.

1.4.1 Polarization Curves

A common method to qualitatively determine the fuel cell performance, is through use of a voltage-current plot, known as a polarization curve. The advantage of polarization curves is that they provide a quick indicator of the qualitative magnitude of the different loss mechanisms within the fuel cell, such as the: mixed potential, and the activation, ohmic and concentration polarizations. These dominant regions are shown in Figure 1.6.

Many models reproduce a polarization curve by subtracting the reversible cell voltage, V_{rev}, by all the loss mechanisms, η, as shown below. Details of each of the remaining terms will be discussed in the following subsections.

$$V_{cell} = V_{rev} - \eta_{act} - \eta_{ohmic} - \eta_{conc} \tag{1.1}$$

Reversible Cell Voltage

The reversible cell voltage, V_{rev}, is the maximum voltage that a single cell can achieve to produce useful work, as shown in Equation 1.2. This equation is calculated based on the change in Gibb's free energy of formation, $\Delta\bar{g}_f$, of the overall reaction (as mentioned in Section 1.2). Here, n and F are the number of electrons participating in the overall reaction, and Faraday's constant, respectively. At 25°C, $V_{rev} = 1.21$ V [1, 16, 17].

$$V_{rev} = -\frac{\Delta\bar{g}_f}{nF} \tag{1.2}$$

As will be discussed later in greater detail, there is typically significant methanol crossover at open circuit, which creates a mixed potential. This significantly reduces the fuel cell's V_{rev}, typically to a range of 0.5 V - 0.7 V [18, 19], as seen in Figure 1.6. This drop in V_{rev} is a combination of a decrease in magnitude of $\Delta\bar{g}_f$, due to the shift in the cathode's half-cell reaction, and due to the increased cathode activation polarization, η_c [18, 20, 21].

Activation Polarization

The activation polarization corresponds to the potential difference, across the electrolyte-catalyst particle interface, required to drive the reaction. At low current densities, this loss mechanism is generally the most dominant, as can be seen in Figure 1.6. A common method to predict this loss mechanism is the Butler-Volmer expression, shown in Equation 1.3 [22,23].

$$j = ai_{o,ref}\left[\left\langle\prod_k\left(\frac{C^k}{C^k_{ref}}\right)^{m_k}\right\rangle\exp\left(\frac{\alpha_a F}{\bar{R}T}\eta_{act}\right) - \left\langle\prod_k\left(\frac{C^k}{C^k_{ref}}\right)^{n_k}\right\rangle\exp\left(-\frac{\alpha_c F}{\bar{R}T}\eta_{act}\right)\right] \tag{1.3}$$

In this equation, j represents the measured volumetric current density, a is the surface area to volume ratio of the electrode, $i_{o,ref}$ is the exchange current density of the electrode at the reference state, C is the molar concentration of the fuel or oxidant, m and n are the reaction order of the anodic and cathodic reactions respectively, α is the charge transfer

coefficient, T is the temperature, and η_{act} is the activation overpotential. The subscripts, a and c, represent the anode and cathode, respectively, whereas k represents the k^{th} species participating in the reaction.

As more current is generated by the fuel cell, the reactions are pushed more in the forward direction, causing the terms representing the reverse reaction to become negligible. This form of the equation is known as the Tafel equation, shown below for the anodic and cathodic reactions, respectively.

$$j = aj_{o,ref}\left\langle \prod_k \left(\frac{C^k}{C^k_{ref}}\right)^{m_k} \right\rangle \exp\left(\frac{\alpha_a F}{\bar{R}T}\eta_{act}\right) \tag{1.4a}$$

$$j = -aj_{o,ref}\left\langle \prod_k \left(\frac{C^k}{C^k_{ref}}\right)^{n_k} \right\rangle \exp\left(-\frac{\alpha_c F}{\bar{R}T}\eta_{act}\right) \tag{1.4b}$$

It should be noted that the form of the Butler-Volmer and Tafel equations shown so far assume that the concentration of ions at the electrode surface is at equilibrium with the bulk solution, and that the reaction mechanism is a one-step and one-electron process [22, 23]. Although both the methanol oxidation and oxygen reduction reactions (MOR and ORR) do not follow this, the Tafel expression is often applied due to its simplicity. A more accurate and frequently adopted approach to account for the multi-step reaction of the MOR is the one proposed by Meyers and Newman [24], shown below. There are many similar expressions in literature, but all have the same general form [25, 26]. Here, the second set of terms in the denominator account for the smooth transition from zero order to first order kinetics, where before, in Equations 1.3 and 1.4a, a step change in reaction order is often taken when changing from zero to first order kinetics [21, 27].

$$j = \frac{aj_{oa}C_l^{MeOH}\exp\left(\frac{\alpha_a F}{\bar{R}T}\eta_{act}\right)}{C_l^{MeOH} + K_a\exp\left(\frac{\alpha_a F}{\bar{R}T}\eta_{act}\right)} \tag{1.5}$$

More rigorous approaches also exist for the MOR and ORR, which account for more detailed reaction pathways and the change in available reaction area due to the absorbed species onto the catalyst surface [7, 18, 28, 29]. However, Equations 1.4b and 1.5 seem to be the most frequently adopted equations to represent the ORR and MOR, respectively. Another common approach is to develop a set of modified equations that account for the physical structure of the CLs. For example, the CLs could be treated as a packed bed of spheres, as can be seen in Figure 1.3, and from there an analytical solution [30–32], or a more detailed numerical solution [33, 34], could be devised to account for the mass transport resistance of reactants. This modification has been demonstrated to be an accurate physical representation of experimental results.

Ohmic Polarization

The next dominant regime is from the ohmic polarization. This loss is due to the resistance to electron and proton conduction through each layer of the fuel cell, as well as the contact resistances between layers [35]. Models often use Ohm's Law to predict this loss, as shown below. This equation often displays a nearly linear trend with current density, any deviation from this trend would stem from non-linearities in the resistance of each layer.

$$\eta_{ohmic} = iR \tag{1.6}$$

Concentration Polarization

The final loss mechanism occurs when the fuel cell becomes transport limited; whereby, reactants cannot reach the CLs fast enough to maintain the reaction rate. As such, the concentration polarization, η_{conc}, only becomes important near the limiting current density, i_{lim}, (the maximum achievable current by the fuel cell) and causes the sharp drop in performance as observed in Figure 1.6. However, DMFCs generally do not reach their i_{lim}, due to their high activation and ohmic polarizations. As such, the concentration polarization

can be neglected with minimal loss in accuracy. If one wanted to model the effects of the concentration polarization, the Nernst equation can be applied where the final form of the equation is shown below [22].

$$\eta_{conc} = \frac{\bar{R}T}{nF} \ln\left(1 - \frac{i}{i_{lim}}\right) \tag{1.7}$$

1.4.2 Methanol Crossover

In DMFCs, the anode and cathode are separated by a membrane. Although this layer is designed to act as a separator to methanol and oxygen, some unreacted methanol is transported through the membrane and reacts in the CCL; this is known as methanol crossover. This process effectively short circuits the fuel cell, since the released proton and electrons from the oxidized methanol in the CCL, readily bond with the available oxygen. As such, the released electrons do not provide useful electrical work for the external load. There are other issues surrounding methanol crossover, some of the main issues are mentioned below.

- Methanol crossover wastes fuel and also causes higher rates of oxygen consumption and water production in the CCL [18, 21]. The increased oxygen consumption could lead to oxygen starvation in the CCL, decreasing the overall performance of the fuel cell. The higher water generation rate causes water to fill the CBL and CCL pores, hindering oxygen's ability to reach the CCL and its ability to react on the catalyst surface, thus decreasing the performance of the fuel cell. Furthermore, the generated water can travel into the CAC, causing channel blockage, where higher back pressures are required to push water out of the channels. The issues surrounding the increased water production and crossover will be discussed in the next sub-section.

- Oxidized methanol will form an oxide film on the Pt catalyst particles within the CCL, increasing the activation polarization and thus decreasing the performance of the fuel cell [18, 24, 25].

- To compensate for the lower performance, higher catalyst loadings (typically Pt) are often required in the CCL, greatly adding to the cost of the fuel cell [36, 37].

There are many mitigation strategies to minimize or eliminate the effects of methanol crossover, such as: the use of selective catalysts and membranes [38, 39], as well as the use of transport barriers such as micro-porous layers (MPLs) [40, 41]. Each of these approaches have their merits. For example, selective cathode catalysts could allow the cathode to be, in some sense, immune to methanol crossover. However, research on these catalysts are still in their infancy these catalysts typically display lower catalytic activity towards oxygen than the traditional Pt-based catalysts [42,43]. Also, since methanol is not consumed in the CCL, any crossed over methanol would fill the CCL's pores preventing oxygen from reaching available reaction sites. Selective membranes could selectively prevent methanol from entering the membrane, essentially eliminating methanol crossover all together. However, these membranes are often more expensive than commercially available membranes, and also generally display higher ohmic resistance, lower chemical and thermal stability, and durability [38,39]. Transport barriers, such as MPLs, would allow the use of traditional materials, as well as help control the motion of the gas and liquid phases, and the species within the fuel cell. The use of MPLs and their design have also been demonstrated to improve fuel cell performance. But this approach only minimizes methanol crossover, not eliminate it.

1.4.3 Water Management

The water management in portable DMFCs and stacks is very important. On the one hand, water helps to promote high membrane conductivity [13]. However, too much water can lead to cathode flooding; where liquid water occupies the cathode's pores preventing oxygen from reaching the CCL. Further complications arise when the liquid water reaches the CAC, and large back pressures are required to remove the condensed water. This causes maldistribution of reactants in the cathode, erratic fuel cell performance and in some cases local membrane dehydration. Each of which complicate the ability to collect repeatable

experimental results [44]. Cycling of the membrane hydration can also lead to pin hole formation, which could lead to device failure and, as discussed in the previous subsection, very high rates of methanol crossover and flooding [45].

Typical water management approaches involve the use of custom material properties for the BLs and CLs [45], the use of MPLs [45, 46], and specialized membranes, control of the cathode inlet relative humidity [44], and use of various channel geometries [47]. To the author's knowledge, a water balance study has not been performed on the FE-DMFC.

1.5 Overview of Modeling Approaches

Early DMFC modeling work assumed the fuel cell operated under single phase conditions. This assumption implies that all species in the anode remain in the liquid state while all species in the cathode remain in the gaseous state. This is only realistic at low current densities and crossover rates [48, 49]. Although simplified, these assumptions allowed for simple yet relatively accurate models to be formulated. Often, depending on the complexity of the model, an exact solution could be devised [26, 50]. Although single phase models are good for determining general trends, they also tend to over-predict the performance of the fuel cell.

Over time, as computational power increased and fuel cell models became more advanced, multiphase models began to be formulated [21, 41, 51–60]. However, when methanol is oxidized, carbon dioxide is produced. This creates a two-phase flow within the anode, since carbon dioxide is in the gaseous state, and methanol and water both co-exist in the gaseous and liquid states. Furthermore, in the cathode, as oxygen is reduced and crossed-over methanol is oxidized, water is generated; which creates a two-phase flow in the cathode. These effects are not taken into account in the single phase models, and are therefore a major short coming. Since these effects are not captured, the predicted performance is overestimated.

1.5.1 Two-Phase Modeling Approaches

Three common multiphase modeling approaches exist in the fuel cell literature: unsaturated/saturated flow theory (UFT and SFT) [41, 52, 53], multi-fluid model (MFM) [54–56] and multiphase mixture model (MMM) [21, 57–60]. The UFT and SFT models assume that the pressure gradient of the primary phase (gas phase for UFT, and liquid for SFT) is negligible [52]. This allows for a simplified set of momentum equations to be solved, allowing for a more direct calculation of the capillary pressure distribution, which drives the flow in a porous media. This assumption begins to break down as the secondary phase generation is high, which typically occurs at high current densities.

A more generalized formulation is the MFM, which accounts for the variation of both phase pressures [54–56]. This modeling approach is frequently used in both DMFC and PEMFC models due to its flexibility and accuracy. This approach uses a set of governing equations for each phase, and each of the sets of governing equations interact through source terms. Although this approach is more physically representative of the fluid flow, it is also very non-linear due to the large number of differential equations that are required to be solved, and due to their strong coupling. A recent approach to reduce the number of differential equations in the MFM, is the mathematically equivalent MMM. This approach treats the multiphase flow as an effective single phase mixture [57, 61]; which is achieved by taking each governing equation and summing it across all phases. A set of algebraic equations are then used to ensure proper coupling between each phase and the mixture. For further discussion on the comparison between the presented approaches, the reader is referred to Wang and Chen [62]. The reader is also referred to Mazumder and Cole's derivation [63, 64] and Sui *et al.*'s [65] extension to their work for a good review of the governing equations required to evaluate the performance of a fuel cell. In this dissertation, the MMM is applied and, wherever applicable, extensions and parallels to the MFM will be provided.

1.5.2 Computational Domain

When modeling the fuel cell domain, there are two common approaches, the multi-domain approach [54, 66, 67] and the single-domain approach [68–70]. The multi-domain approach models each layer within the fuel cell separately and the adjacent layers are coupled through interfacial conditions (typically through a continuity and Dirchlet conditon) [54]. It is also common to tailor each set of governing equations to each layer. It is expected that this approach is more computationally stable but likely requires a greater number of iterations to achieve convergence. The single-domain approach, on the other hand, treats the entire fuel cell as a unified domain, removing the need for interfacial conditions [71]. In this case, the governing equations are formulated in a manner that makes them independent of which layer of the model is being examined. This approach is very convenient for fuel cell modeling.

To achieve a single-domain model, one needs to solve each governing equation with a consistent variable. However, this can become problematic for the water's species conservation equation [58,72], where in the porous layers (BLs and CLs) the liquid saturation (the ratio of liquid volume within the pore volume, given by $s = \forall_l / \forall_{pore}$) is often used as the variable of choice. However, in the electrolyte phase (such as in the CLs and membrane), the liquid saturation is not very meaningful, due to the hydrophilic membrane pores. This causes the membranes, to a good approximation, to be completely liquid saturated [73]. As such, it is more meaningful to rather track the water content (λ_{wc}, the number of water molecules per sulfonic acid group within the membrane) or the concentration of water in the electrolyte phase, $C_e^{H_2O}$ [31, 55, 65]. This change in variables quickly demonstrates how a single domain approach can be difficult to formulate.

1.5.3 Liquid Saturation Distributions

In a fuel cell assembly, known as a membrane electrode assembly (MEA), it is typical to have different porous properties for each layer. In a two-phase flow regime, if two

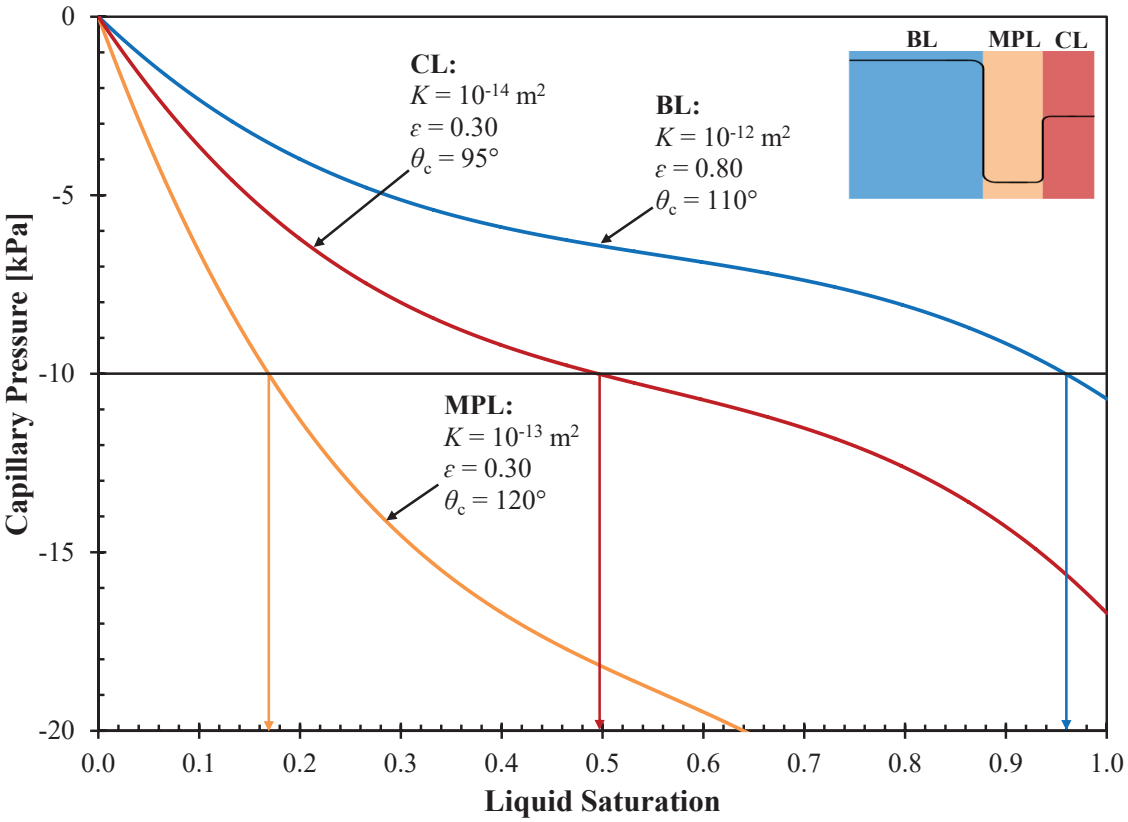

Figure 1.7: Demonstration of the saturation jump across adjacent layers of differing porous properties, for an assumed uniform capillary pressure of -10 kPa. The black line, in the top right sub-figure, qualitatively shows the liquid saturation distribution between the three layers.

materials of differing porous properties are adjacent, one layer will act more like a 'sponge', causing more liquid to be retained in one layer than the other [74]. This is also shown graphically in Figure 1.7, for a uniform capillary pressure, P_{cap}, of -10 kPa across three layers. Because each layer has its own $P_{cap} - s$ curve, a jump in s will occur across each interface; where for example, s is 0.96 in the BL, 0.17 in the MPL, and 0.50 in the CL. Similar behaviour can be expected in the case where there is a spatial distribution of porous properties, such as when any of the layers are compressed during fuel cell assembly.

To model this phenomena, two common methods in the literature are discussed. In the first, which is more applicable to the MFM approach, the liquid and gaseous pressures can be obtained from the conservation of mass and momentum equations. The difference in phase

pressures yield the P_{cap} distribution. The corresponding s distribution can be obtained from a $P_{cap} - s$ expression, such as the Young-Laplace equation, as shown in Equation 1.8 [55,56,75]. Here, σ is the surface tension, K is the absolute permeability, ε is the porosity, θ_c is the contact angle, and J is the Leverett J-Function, which is a function of s.

$$P_{cap} = P_g - P_l = \sigma(\cos\theta_c)\left(\frac{\varepsilon}{K}\right)^{1/2} J \tag{1.8}$$

The other approach is to obtain a governing equation (either from the liquid continuity equation or an appropriate species equation) that is in terms of s [21,52,53]. A common form of the liquid continuity equation that is used in such an approach is shown below, which is derived from coupling Darcy's Law for both the liquid and gas phases [76–78].

$$\nabla \cdot \left[\frac{K k_{rl}}{\nu_l}\frac{\partial P_{cap}}{\partial s}(\nabla s) + \frac{k_{rl}\nu_g}{k_{rg}\nu_l}(\rho_g \mathbf{u_g})\right] = S_{gen,l} \tag{1.9}$$

This approach yields identical results as the previous approach when the spatial variation in porous properties are negligible. Due to this assumption, Equation 1.9 is not capable of capturing a liquid saturation jump. To circumvent this issue, many authors apply an interfacial continuity and capillary pressure equality to the relevant interfaces [67, 79]. Due to this interfacial condition, this approach is not well-suited for a single domain approach.

1.6 FE–DMFC Literature Review

This section is devoted to summarizing the experimental and modeling studies currently published in the literature on the FE-DMFC. This section will then tie into the next section, where the unresolved issues in FE-DMFC literature will be summarized, along with this dissertation's research objectives.

1.6.1 Experimental Studies

Kordesch *et al.* [5] demonstrated the FE and circulating electrolyte (CE) concepts for a PEMFC and DMFC, by comparing the open circuit voltages (OCV) of these fuel cells when the FEC was active and inactive. In their study, they found that the OCV improved when the FEC was active and provided possible improvements on the FE-DMFC and plant designs. A notable recommendation was the inclusion of a liquid electrolyte-methanol separator in the plant design, such that the removed methanol and liquid electrolyte can both be recycled. Later, Sabet-Sharghi *et al.* [15, 80] performed a set of parametric studies on the FE-DMFC, where they investigated the effect of the: FEC's inlet concentration, flow rate and thickness, cell temperature, and methanol concentration and flow rate on the FE-DMFC's performance. They demonstrated that the FE concept indeed decreased the amount of methanol reaching the CCL; however careful consideration had to be made to the FEC design. A major finding was that an open FEC was impractical for use, since the membranes can bulge and come into contact, hindering the performance of the FEC. Instead, Sabet-Sharghi *et al.* suggested the use of a porous spacer to allow the FE to pass through, while preventing the membranes from coming into contact.

Kablou also recently examined the performance of a five cell, FE-DMFC short stack where he applied the advice of Sabet-Sharghi *et al.* [81]. In his experimental work Kablou examined the effects of: stack temperature, methanol concentration and flow rate, and FE and air flow rate. Kablou found that the FE concept increased the performance of the stack and also found that at high operating currents, the cell voltage will drop significantly if the FE were to stop flowing, which could be an effective method to rapidly shut down the stack. He further determined that the FE is an effective method to maintain a uniform temperature across the stack.

Duivesteyn experimentally measured the porous properties (particle diameter, porosity

and permeability) of different FEC materials, and their affect on the fuel cell's performance, when the cell temperature and the FE flow rate were varied [82]. Although Duivesteyn reported inconsistent performance on the optimal FE flow rate, his results seem to indicate that higher pore diameters and thus higher permeabilities require higher FE flow rates to maintain optimal performance. Duivesteyn suspected that the FEC's back pressure played a significant role in the fuel cell's performance.

Ouellette *et al.* [9] recently proposed to replace sulfuric acid with a MOR intermediate, specifically formic acid. This design allowed for the FEC outlet to be routed to the anode inlet, thereby readily recycling the formic acid-methanol mixture as fuel, removing the need for a separator as suggested by Kordesch *et al.* [5]. Interestingly, they found that the formic acid electrolyte DMFC (FAE-DMFC) had a maximum power output at a temperature of 48°C, which could make this fuel cell a viable solution for hand held and portable applications. Although the fuel cell's performance was limited due to the low conductivity of formic acid, Ouellette *et al.* encouraged the exploration of different MOR intermediates that could be used as a sulfuric acid substitute, as well as the use of conductivity enhancement techniques such as dissolving a salt of strong acid into the electrolyte.

1.6.2 Modeling Studies

One of the first models developed for the FE-DMFC was by Kjeang *et al.* [83, 84]. In their work, they developed a two and three dimensional (2 and 3D) computational fluid dynamic (CFD) model to examine the theoretical effectiveness of an open, single-phase FEC. They found, under their examined conditions, that the FEC can reduce the methanol crossover flux by as much as 90%, and that the methanol crossover flux was inversely proportional to the flow rate of the FE.

Colpan *et al.* recently developed an extension to Kjeang *et al.*'s analysis by creating a

1 and 2D single phase performance model for the DMFC and FE-DMFC [35, 85]. In these studies, they conducted several simulations on the FE, methanol and air flow rates, FEC thickness, and inlet methanol concentration. They found that the greatest gross power output can be achieved with the highest possible FE flow rate and thinnest possible FEC, and that higher power densities can be achieved with increased methanol and air flow rates. However, the electrical efficiency was found to decrease with increased methanol flow rate, since less methanol was available to be consumed. They also found that with the CE concept, the efficiency of the fuel cell can be increased by as much as 57%. It should be noted that Colpan's DMFC models were compared against experimental DMFC data, and that the FE-DMFC model was treated as an extrapolation of the results. This was due to the lack of FE-DMFC experimental data at the time. Furthermore, the effects caused by the FEC's back pressure, to maintain its flow rate was not included.

Kablou also performed a two-phase hydrodynamic study of the anode flow field that was coupled to an analytical single phase model within the MEA [81]. Kablou's hydrodynamic algorithm applied the Hardy-Cross algorithm, with a separated flow pressure drop and void fraction method. Using his algorithm, Kablou tested the effect of cell temperature, current density, and methanol concentration and flow rate on the hydrodynamics of the single cell and stack anode flow fields. Kablou demonstrated the importance of the inclusion of two-phase flow within the anode flow field, as well as displayed the differences in the predicted solution when different pressure drop and void fraction methods were applied. Out of the tested methods, the Lockhart-Martinelli and CISE pressure drop and void fraction methods most accurately reproduced the experimental data. He also pointed out that the two-phase gravitational pressure was the most dominant component of pressure, and the greatest pressure drop occurred near the anode inlet manifold.

Later, Duivesteyn *et al.* [86,87] extended Kjeang's work by examining the isothermal and

non-isothermal hydrodynamics and effectiveness of a porous single phase FEC. Their studies approximated the FEC's working fluid as water, and they did not account for the mass transfer in the anode or cathode, and they focused on the pressure drops and flow behaviour in such a channel for different porous structures. Duivesteyn *et al.* concluded that Darcy's Law, and as such a 1D velocity profile, was a valid approximation of the flow behaviour within the FEC and that preheating the FEC has negligible impact on the flow behaviour due to the very small thermal entry length. Duivesteyn *et al.* also provided recommendations on the porous structure to minimize methanol crossover and pressure drop, such as: the use of a porosity in the range of 0.5 – 0.6 and a particle diameter that is an order of magnitude smaller, or greater, than the FEC thickness.

1.7 Unresolved Issues and Research Objectives

Reviewing the information discussed in Sections 1.5 and 1.6, several unresolved issues have been brought up, and are summarized below.

1. Current FE-DMFC models are only single phase [35, 83–87]; with the exception of Kablou's two-phase hydrodynamic model [81]. It has been demonstrated in DMFC and PEMFC literature, that the multiphase flow significantly affect the performance of the fuel cell in a detrimental manner [88, 89]. It is not known how the multiphase flow will affect the performance of the FE-DMFC.

2. The removal of methanol from the FEC has been accounted for by a convective sink term, without the consideration of how its pressure and velocity would affect the rest of the fuel cell [35, 85]. The increased pressure within the FEC was further demonstrated in Duivesteyn *et al.*'s work [86, 87]. It is suspected that this increased pressure could cause a counter convective flux from the FEC to the anode and cathode. However, this phenomenon and its affect on the fuel cell's performance have yet to be explored.

3. The validation process for FE-DMFC performance models have consisted of comparing against an analytical solution [83,84], or by producing an equivalent DMFC model and comparing the results to DMFC experimental data [35, 85]. As mentioned previously, it is suspected that the FE may affect the fuel cell's performance in a non-linear fashion and still has yet to be fully understood. As such, a more thorough verification and validation process will be required to ensure accurate predictions.

4. Published experimental studies on the FE-DMFC have only qualitatively discussed how the ohmic resistance, and the methanol and water crossover fluxes affect the performance of the fuel cell [15, 81, 82]. However, in some cases, little theoretical backing to the experimental observations have been provided. As such, further details of the physics during fuel cell operation still need to be resolved.

5. There are few single domain models in literature that apply the MMM. The ones that exist often use information concerning the gaseous state to determine the activity, and thus the water content, within the membranes, complicating the model. A formulation that makes use of mixture variables only would be more practical, and to the author's knowledge, has not been formulated.

6. A common method to determine the saturation profile is through application of Equation 1.9. However, in this form, an explicit set of interfacial conditions would be required, as discussed in Section 1.5.3, in cases where saturation jump is to occur. This explicit treatment is not useful for a single domain approach, as the saturation jump should occur on its own, without the need of any explicit treatment. A single domain approach to account for this effect requires formulation.

Of these unresolved issues, the most salient points to be raised are as follows:

- The current state of understanding of how the FE-DMFC functions is still in its infancy, and little is known as to how the FEC affects the performance of the fuel cell;

- The current modeling approaches need to be improved to increase the fidelity of the predictions and ease of implementation; and,
- Better verification and validation practices need to be implemented, such that these tools can provide better predictions and understanding of how the FE-DMFC functions.

As such, the objectives of this dissertation is to address these unresolved issues by developing a single domain MMM of the FE-DMFC. The derivation of this model is intended to extend the MMM formulation, such that only mixture variables are required throughout the computational domain, and to provide an approach to account for liquid saturation jumps in a single domain manner. A focus of the study will be to demonstrate the capabilities and limitations of this model, through verification and validation, as well as apply the model to understand in detail how the fuel cell functions and how the FEC affects the performance of the fuel cell.

1.8 Organization of Presented Thesis

This dissertation is separated into five chapters to achieve the objectives mentioned in the previous section. A summary of each chapter is provided below.

Chapter 1 presents the necessary background information and literature review to understand the information in this dissertation. The scope and outline of this dissertation are provided.

Chapter 2 details the derivation and formulation of a 1D, multiphase and single domain model of the FE-DMFC. A detailed discussion on the assumptions and their expected impact on the model's predictions, along with the solution methodology, numerical challenges, and calibration procedure are provided.

Chapter 3 presents three test cases that are used to verify and validate the model presented in Chapter 2. Two test cases involve comparisons to analytical solutions, while the other test case involves a comparison to in-house experimental FE-DMFC data. Details of the analytical solutions and the collected experimental data are provided in Appendices C, D and E, respectively.

Chapter 4 demonstrates the capabilities of the numerical model, proposed in Chapter 2, by examining the performance and the physics of the fuel cell under different scenarios. Some of which include: providing an explanation of the experimental observations that are presented in Chapter 3, and predicting the performance of the fuel cell under various FEC porous structures, and various FEC and membrane thicknesses. A comparison between the FE-DMFC's and DMFC's performance is presented.

Chapter 5 summarizes the conclusions and contributions of this dissertation. Possible future paths in which this study could be extended are also discussed.

Chapter 2

Modeling Approach and Formulation

As current FE-DMFC performance models are all single phase, and few fuel cell multiphase mixture model (MMM) formulations are single domain, this chapter details a formulation that solves both of these issues. This chapter is intended to clearly detail:

- the assumptions and their expected impact on the model's predictions;
- the derivation and implementation of the model; and,
- the challenges and considerations needed to obtain a robust and stable solution.

The proposed approach is expected to simplify the implementation of future fuel cell models, provide greater insight into the physics of the fuel cell and more realistic predictions of the fuel cell's performance. It should be noted that the information in this chapter is based off of the author's previous published work [90–92].

2.1 Computational Domain

A schematic of the fuel cell's computational domain is shown in Figure 2.1, and extends across the whole MEA and excludes the channels. The reduced area caused by the presence of the ribs, however, are accounted for at the anode and cathode channel-BL interfaces, and is treated with an 'effective channel and rib area', whereby the anode and cathode flow

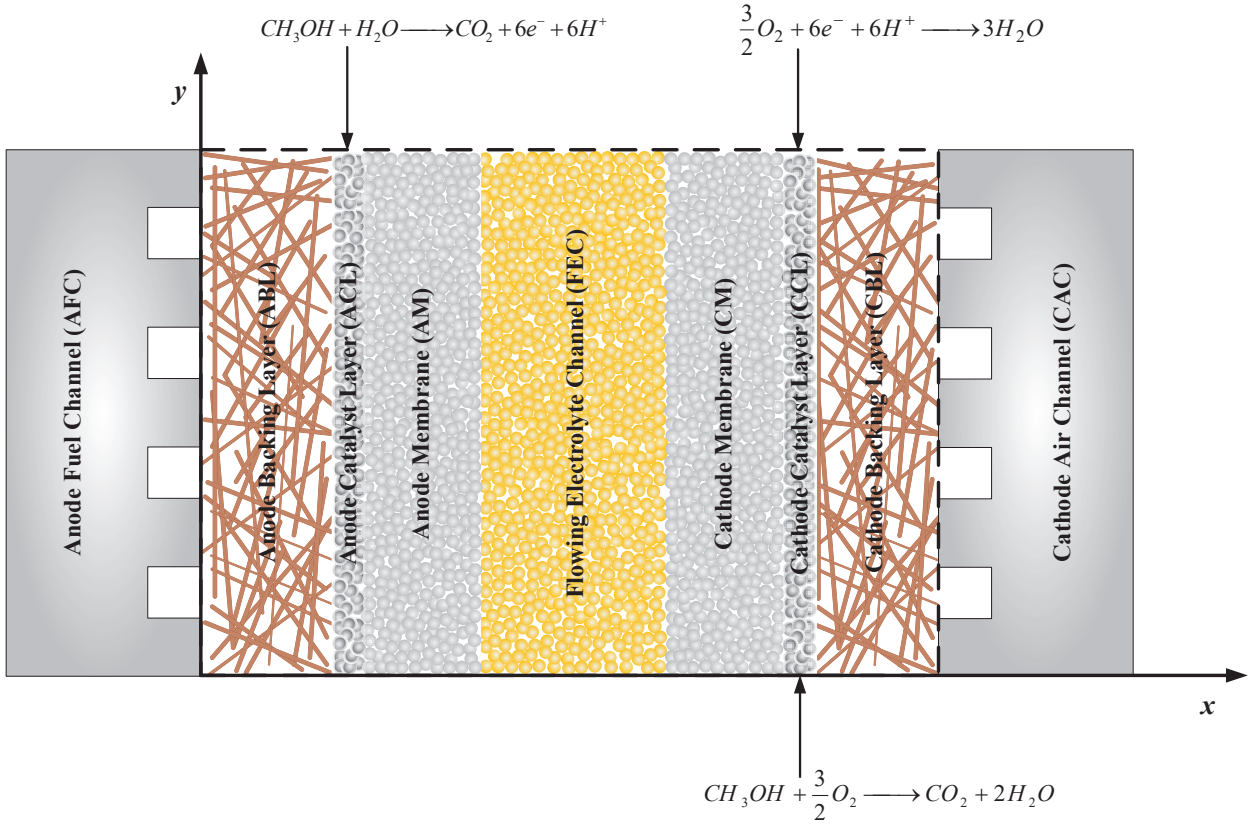

Figure 2.1: Schematic of the computational domain used in the model. The layers enclosed within the dashed box are the ones that are considered within the model.

fields are each assumed to be collapsed to one large channel and rib.

This single domain model considers all layers within the domain to have finite thickness (BLs: 280 μm, CLs: 28 μm, membranes: 183 μm, and FEC: 610 μm), and considers the domain to be 1D. The 2D form of each equation, however, will be needed to account for the presence, and introduction and removal of mass at the FEC inlet and outlet. To decrease computational time, each variable is confined to layers where the transport equations are physically meaningful, or where information of a particular variable is not known without solving the governing equations [71]. This will be expanded upon in Section 2.6.

In this work, the pathways shown below are assumed to exist for each species. The fuel cell that is being modeled is the one that was experimentally tested in this work; its design

will be detailed in Section 3.3.

- Methanol is taken to be supplied at the anode, and is transported towards the cathode.
- Oxygen is taken to be supplied at the cathode and is transported towards the anode.
- Water is taken to be supplied at the anode, cathode and FEC inlet and is allowed to flow as governed by the conservation equations.
- Sulfuric acid is taken to be fully contained within the FEC.

2.2 Modeling Assumptions

Many of the assumptions made in this model are similar to those mentioned in Colpan *et al.*'s model [35]. However, in the presented model, both the liquid and gaseous states are considered, also the membranes are no longer assumed to be fully hydrated. The remaining assumptions are listed below in italics. After each assumption, a discussion on the validity and impact of these assumptions on the final solution are provided.

1. *The fuel cell operates under steady state and isothermal conditions*:

   Realistically, the fuel cell will operate under transient conditions due to any non-uniformities within the fuel cell, external disturbances, and obstructions within the porous media caused by the bubble and droplet motion within the fuel cell. Furthermore, over time the fuel cell performance will degrade due to factors such as: catalyst poisoning, carbon corrosion, membrane degradation, and MEA delamination [93–95]. A degradation study is outside the scope of this work and will not be examined. But the model can be considered to look at a statistical steady state, which is often considered in steady state models and experiments. Furthermore, the fuel cell will also realistically operate under non-isothermal conditions, due to thermal contact resistances, chemical reactions in the CLs, convective heat transfer from the AFC, CAC and FEC,

latent heat from evaporation and condensation processes and joule heating [65, 96]. As such, this assumption will negate any temperature driven transport of species, such as thermo-capillary action and the "heat pipe effect", as well as negate any evaporation and condensation of species [67]. In literature, it has been shown that DMFCs and PEMFCs tend to exhibit temperature differences, as high as $\sim 5°C$ [97–99]. However, it is suspected that the temperature profile within the FE-DMFC will be more uniform due to the convective heat transfer and large thermal capacitance of the FE.

2. *All fluids are ideal and exist in equilibrium with one another*:

   This is a common assumption in modeling literature due to the complexity of accounting for thermodynamic non-ideality, which results in having to determine the spatial activity coefficient distribution of each species [100]. There is also evidence in DMFC and PEMFC literature that these fuel cells operate in a state of non-equilibrium, due to the slow rates of absorption and desorption of water into and out of the electrolyte phase [101, 102]. Furthermore, it is not known if the FE-DMFC is in a state of equilibrium. Therefore, for simplicity, the FE-DMFC is treated to be in a state of equilibrium. This would cause the sorption processes to occur infinitely fast, likely causing an over-prediction in the concentration of absorbed water in the electrolyte phase.

3. *Each media is homogeneous and isotropic*:

   When the fuel cell is assembled and clamped shut, each layer will be compressed underneath the ribs, while some material will intrude into the channels [103, 104]. Although the compression will increase the material's electrical conductivity, the mass transport resistance will also increase, due to the collapsed pore structure [105]. The model formulation proposed in this chapter is capable of accounting for heterogeneous material properties, but the actual deformed geometry and material property distributions of an assembled FE-DMFC are not currently known. Therefore, for simplicity, each layer will be treated as homogeneous. This assumption will likely cause an over-prediction

in the true concentration profiles and thus performance of the fuel cell, due to the lower mass transfer resistance associated with this assumption.

4. *The membranes are impermeable to the gaseous phase*:

   There is numerical evidence which suggests that the membranes can be treated to good approximation fully liquid saturated [73]. Although to the author's knowledge, the capillary pressure behaviour of the membranes is not fully known for the full range of liquid saturation values and as such is lacking in literature, the membrane layers are treated as fully liquid saturated for simplicity. This can be further substantiated by the fact that the pores of the Nafion membrane are hydrophilic when and near liquid equilibrium [106, 107], thus attracting water, this would then push the gaseous phase out, maintaining the expected fully liquid saturated membranes.

5. *All crossed over methanol is fully consumed at the cathode catalyst layer*:

   It has been experimentally shown by Wang and his team to be an accurate assumption [108]. Although at low current densities this will be least accurate since at this regime, the greatest amount of methanol crossover occurs, resulting in the greatest probability of methanol flowing through the CCL unreacted. While at medium and high current densities, this assumption will be the most accurate, since any crossed over methanol will be rapidly consumed due to the higher reaction rates. This is also expected to be accurate due to the expected low rates of methanol reaching the cathode, and abundance of oxygen in the cathode.

6. *The inlet velocity profile of the FEC is uniform*:

   Since the FEC is porous, the entry length is expected to be small and the viscous forces from the porous structure onto the fluid are expected to be high [82,86]; thus generating a blunt velocity profile. To maintain such a velocity profile, numerical results suggest that the FEC thickness must be > 0.05 mm [82], which is much smaller than what is used in this study (0.6 mm). When the FEC thickness used in this study is simulated,

a blunted velocity profile is shown to be accurate, even a high flow rate of 10 mL min^{-1}. The FEC's boundary layer thickness is about 1% of the FEC's thickness [82].

2.3 Reduction of Governing Equations

Now that the assumptions are defined, each governing equation for the MMM will now be discussed in this section. These equations are presented for the case where the gas, liquid and the electrolyte phases all co-exist. In the scenario where any one of these phases do not exist, the corresponding terms are set to zero. Before delving into the governing equations, the notation used with the equations will be presented.

2.3.1 Notation

In the subsequent sections, the subscripts e, g, and l refer to the electrolyte, gaseous and liquid states respectively; while the subscripts i and lg refer to an arbitrary phase of interest (liquid, gas, electrolyte), and effective two-phase phase value, respectively. The terms with the subscript of gen represents a source term that accounts for the generation or consumption of species through a chemical process, while the subscript $trans$ refers to a source term that accounts for a transport related process such as a body force. The superscript k refers to an arbitrary species of interest (methanol, oxygen or water). In the case where a subscript is not present, it is implied that the variable corresponds to the mixture. All pieces of notation can be found in the Nomenclature section.

2.3.2 Conservation of Mass

The conservation of mass equation, also known as the continuity equation, accounts for the mass balance across each control volume. The MMM version of this equation, is shown below and derived from the summation of each phase's conservation of species equation (discussed in Section 2.3.4), multiplied by their respective molar mass [109].

$$\nabla \cdot (\rho \mathbf{u}) = \left(\sum_k M^k S^k_{gen} \right) - \left(\sum_k M^k \left(\nabla \cdot \dot{\mathbf{N}}''^{\mathbf{k}}_{\mathbf{e}} \right) \right|_{CL} = S_{gen} + S_{trans} \tag{2.1}$$

Although all phases are part of the multiphase mixture, it is assumed that the mixture phase is only composed of the liquid and gaseous phases. This gives rise to the transport source term, S_{trans}, which accounts for the transport of methanol and water in the CLs' electrolyte phase. In all other regions, $S_{trans} = 0$. Details of each source term can be found in Section 2.4.3. The continuity equation, along with the conservation of momentum equation, discussed in the next sub-section, are used to determine the velocity distribution within each of the fuel cell's layers. The velocity distribution is used to determine the convective mode of transport within the conservation of species equations.

2.3.3 Conservation of Momentum

The conservation of momentum equation, accounts for the forces acting on the fluid. In the limit of low Reynolds flow ($\text{Re} = \mathbf{u}\bar{d}_{pore}/\nu < 1$), in a porous medium, the convective terms within the Navier-Stokes equation can be assumed to be negligible and that the viscous forces are linearly dependent on velocity [110–112]. This gives the form of the momentum equation known as Darcy's Law, shown below.

$$\rho \mathbf{u} = -\frac{K}{\nu}(\nabla P) \tag{2.2}$$

2.3.4 Conservation of Species

The conservation of species equation is solved throughout the computational domain to track the concentration distribution of each species. In the MMM approach, this equation is derived by summing each phase's conservation of species equation for a given species. This equation is shown below for the case where the electrolyte, gas and liquid phases all co-exist.

$$\nabla\cdot\left[-D_l^k(\nabla C_l^k)-D_g^k(\nabla C_g^k)-D_e^k(\nabla C_e^k)+\mathbf{j_l}\left(\frac{C_l^k}{\rho_l}-\frac{C_g^k}{\rho_g}\right)+\gamma^k\mathbf{u}C^k+\mathbf{u}_eC_e^k+\varepsilon_e x_l^k n_d^{H_2O}\frac{\mathbf{i_e}}{F}\right]=S_{gen}^k \tag{2.3}$$

As can be seen in this formulation, the first three sets of terms correspond to the diffusion of each phase. The fourth term accounts for capillary-induced transport of the liquid and gaseous phases. The fifth and sixth sets of terms account for the convection of species k in both the mixture and electrolyte phases, respectively. The last set of terms on the left hand side account for the drift of charged species in an electric field. This process is known as electro-osmosis. The term on the right hand side accounts for any generation or destruction of species k. In this work, the velocity within the electrolyte phase of the CLs is considered to be negligible, due to the large difference in permeability between the porous domain and the electrolyte phase. However, within the AM and CM, the mixture velocity is equal to the velocity within the electrolyte phase.

Since Equation 2.3 cannot be solved effectively in its current state, due to the large number of unknowns in one equation, this equation is instead formulated to fit the form of the convective-diffusion-reaction equation, shown in Equation 2.4. The first source term on the right hand side, S_{gen}^k, accounts for any generation or destruction of species, while the second source term, S_{trans}^k, is used to bundle any terms that do not fit the form of Equation 2.4. The advantage of this equation is that traditional and well-established mathematical and numerical methods can be applied to solve this equation.

$$\nabla\cdot\left[-D_{lg}^k(\nabla C_i^k)+\mathbf{u_{lg}^k}C_i^k\right]=S_{gen}^k+S_{trans}^k \tag{2.4}$$

The constitutive equations for the transport equations and source terms are shown in Tables 2.1 and 2.2, respectively, and are discussed in Section 2.4. The formulation of the methanol, water and oxygen transport equations are provided in the following sub-sections.

Methanol Transport

For the transport of methanol, it is more practical to track the liquid state since the anode's pores are predominantly composed of liquid, while the gaseous state is generally dispersed as gaseous bubbles [113–115]. Therefore, setting Equation 2.4 in terms of the liquid state, the two-phase diffusion coefficient takes the form shown in Equation 2.5.

$$D_{lg}^{MeOH} = D_{l}^{MeOH} + \frac{D_{g}^{MeOH}}{k_{H}^{MeOH}} + D_{e}^{MeOH} \tag{2.5}$$

To relate the gaseous and liquid concentrations, Henry's Law is applied, as shown below.

$$k_{H}^{MeOH} = \frac{C_{l}^{MeOH}}{C_{g}^{MeOH}} \tag{2.6}$$

Applying Equation 2.6, methanol's two-phase velocity, $\mathbf{u_{lg}^{MeOH}}$, provided below, is the summation of each of the contributions to the velocity; the bulk fluid motion, and the capillary and electro-osmotic drag induced velocities respectively.

$$\mathbf{u_{lg}^{MeOH}} = \gamma^{MeOH}\mathbf{u}\left(s + \frac{1-s}{k_{H}^{MeOH}}\right) + \mathbf{j_l}\left(\frac{1}{\rho_l} - \frac{1}{k_{H}^{MeOH}\rho_g}\right) + \frac{\varepsilon_e n_d^{H_2O}}{C_l^{H_2O} + C_l^{MeOH}}\frac{\mathbf{i_e}}{F} \tag{2.7}$$

Oxygen Transport

To determine oxygen's concentration profile, the same approach for methanol is applied. Tracking the gaseous state, and assuming the concentrations of oxygen in the electrolyte and liquid phases are negligible, oxygen's two-phase diffusion coefficient and velocity reduce to the form shown in Equations 2.8 and 2.9.

$$D_{lg}^{O_2} = D_{g}^{O_2} \tag{2.8}$$

$$\mathbf{u_{lg}^{O_2}} = \gamma^{O_2}\mathbf{u}\,(1-s) - \frac{\mathbf{j_l}}{\rho_g} \tag{2.9}$$

Water Transport

To remove the complexity of swapping between two variables of interest (s in the porous layers and λ_{wc} or $C_e^{H_2O}$ in the electrolyte phases), this derivation made use of the mixture water concentration, C^{H_2O}, as the phase of interest throughout the domain. Wherever applicable, s and λ_{wc} are back calculated using the equations discussed in this section. In the case of two-phase flow, the capillary diffusion flux (the fourth set of terms in Equation 2.3) can be reformulated into a diffusive flux with respect to C^{H_2O} and the Young-Laplace coefficient, ψ, through use of the chain rule, as shown in Equation 2.10. The expression for ψ and the liquid phase capillary diffusion flux, $\mathbf{j_l}$, can be found in Table 2.1.

$$\mathbf{j_l}\left(\frac{C_l^{H_2O}}{\rho_l} - \frac{C_g^{H_2O}}{\rho_g}\right) = -D_{cap}^{H_2O}(\nabla C^{H_2O}) - D_{cap}^{\psi}(\nabla\psi) \tag{2.10}$$

The first set of terms on the right hand side account for the diffusion of water due to a capillary pressure gradient caused by a difference in liquid saturation. The corresponding diffusion coefficient, $D_{cap}^{H_2O}$, is named the capillary diffusion coefficient of water, and has a form shown below [116].

$$D_{cap}^{H_2O} = -\frac{\lambda\,(1-\lambda)\,K}{\nu}\frac{\psi}{C_l^{H_2O} - C_g^{H_2O}}\frac{\partial J}{\partial s}\left(\frac{C_l^{H_2O}}{\rho_l} - \frac{C_g^{H_2O}}{\rho_g}\right) \tag{2.11}$$

The second set of terms in Equation 2.10 account for the capillary pressure gradient caused by changes in the pore structure. This new term allows for saturation jumps to occur on their own, in a single domain. The corresponding diffusion coefficient, D_{cap}^{ψ}, is named the Young-Laplace diffusion coefficient of water, and has the form shown below.

$$D_{cap}^{\psi} = -\frac{\lambda\,(1-\lambda)\,K}{\nu}\left(\frac{C_l^{H_2O}}{\rho_l} - \frac{C_g^{H_2O}}{\rho_g}\right)J \tag{2.12}$$

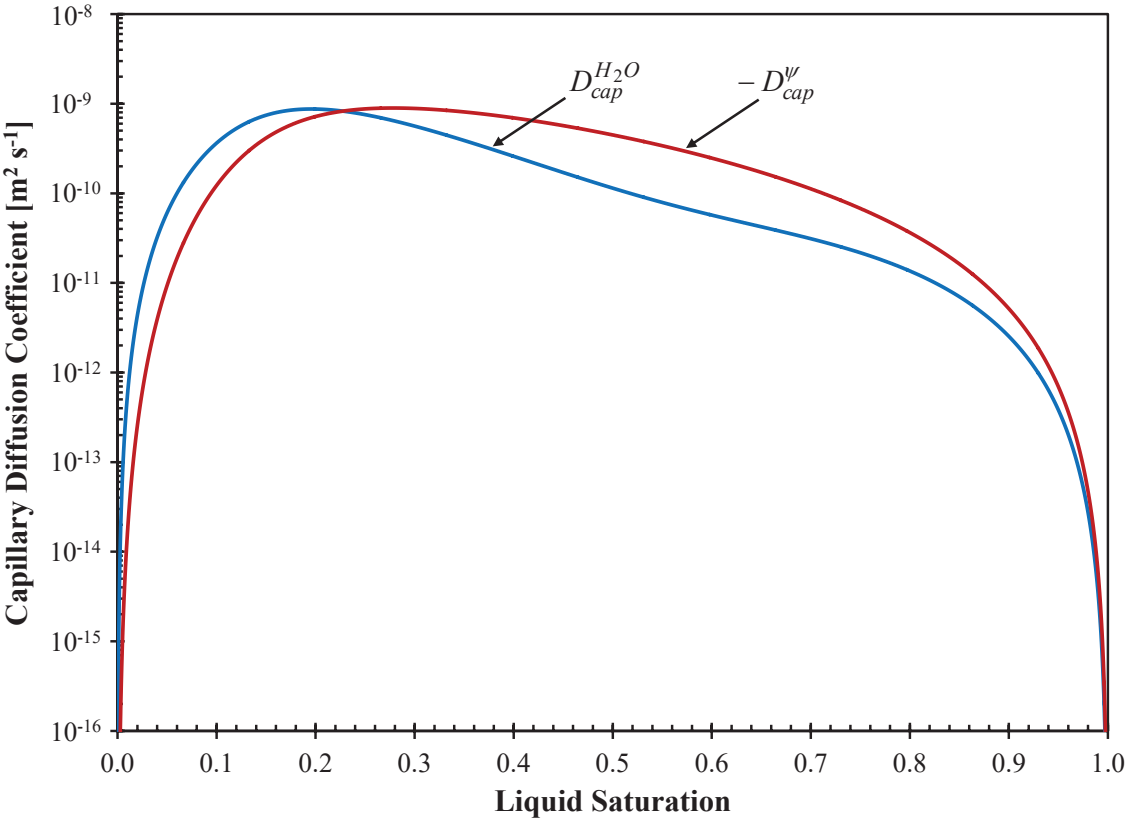

Figure 2.2: Comparison of the capillary diffusion coefficient of water, $D_{cap}^{H_2O}$ (Equation 2.10), and the Young-Laplace diffusion coefficient of water, D_{cap}^{ψ} (Equation 2.11), both at 80°C and for a porous media with $\varepsilon = 0.78$, $K = 10^{-12}$ m^2 and $\theta_c = 110°$.

For reference, $D_{cap}^{H_2O}$ and D_{cap}^{ψ} are plotted in Figure 2.2. As can be seen, both diffusion coefficients are on the same order of magnitude, suggesting that the inclusion of the material property gradient is non-negligible and demonstrates the importance of the Young-Laplace terms near material interfaces, where $\nabla\psi$ can be very large. It should be noted that the approach described thus far, can also be applied to the MFM. This application is provided in Appendix A for the MFM's liquid saturation equation.

For water dissolved in the electrolyte phase, it can be shown that the concentration of water in the electrolyte phase, $C_e^{H_2O}$, is related to the water content, λ_{wc}, through the following expression.

$$C_e^{H_2O} = \frac{\rho_e}{M_e}\lambda_{wc} \tag{2.13}$$

Equation 2.14 is then used to calculate λ_{wc} under equilibrium [55, 75].

$$\lambda_{wc} = \begin{cases} \lambda_{wc,g@30°C} + \dfrac{\lambda_{wc,g@80°C} - \lambda_{wc,g@30°C}}{50}(T - 303.15) & \text{for } a \leq 1, s = 0 \\ \lambda_{wc,l}s + \lambda_{wc,g@a=1}(1 - s) & \text{for } s > 0 \end{cases} \tag{2.14}$$

When the activity, $a < 1$, single phase gas flow prevails and λ_{wc} is assumed to be linearly interpolated between two equilibrium isotherms, as given by Equations 2.15 and 2.16, at 30°C and 80°C, respectively.

$$\lambda_{wc,g@30°C} = 0.043 + 17.81a - 39.85a^2 + 36.0a^3 \tag{2.15}$$

$$\lambda_{wc,g@80°C} = 0.3 + 10.8a - 16a^2 + 14.1a^3 \tag{2.16}$$

Once $a = 1$, any additional water is assumed to condense. The corresponding λ_{wc} is assumed to be interpolated between the liquid and gaseous equilibrium water contents, based on the liquid saturation levels. The liquid equilibrated water content, $\lambda_{wc,l}$, is assumed to be constant, with a value of 22 [117]. The fully vapour-equilibrated water content, $\lambda_{wc,g@a=1}$, follows the same correlations as before with $a = 1$.

Therefore, for the single phase gas flow scenario, $s = 0$ and $C^{H_2O} = C_g^{H_2O}$. The activity of water can thus be formulated as shown below.

$$a = \frac{C^{H_2O}}{C_{g,sat}^{H_2O}} \tag{2.17}$$

In the case where $s > 0$, λ_{wc} and C^{H_2O} can be equated through the saturation, as shown

below. In the model, this equation is used to calculate s and λ_{wc}.

$$s = \frac{\lambda_{wc} - \lambda_{wc,g}}{\lambda_{wc,l} - \lambda_{wc,g}} = \frac{C^{H_2O} - C^{H_2O}_{g,sat}}{C^{H_2O}_{l} - C^{H_2O}_{g,sat}} \tag{2.18}$$

When $a < 1$, Equations 2.13, 2.14 and 2.17 can be substituted into Equation 2.3. By applying the chain rule, $D^{H_2O}_{\lambda,eff}$ can be formulated as shown in the first part of Equation 2.19. When $s > 0$, the same process can be applied, using Equation 2.18. The final result is shown in the second part of Equation 2.19.

$$D^{H_2O}_{\lambda,eff} = \begin{cases} \dfrac{\rho_e}{M_e} \dfrac{D^{H_2O}_e}{C^{H_2O}_{g,sat}} \dfrac{\partial \lambda_{wc}}{\partial a} & \text{for } C^{H_2O} \leq C^{H_2O}_{g,sat} \\ D^{H_2O}_e \dfrac{\rho_e}{M_e} \left(\dfrac{\lambda_{wc,l} - \lambda_{wc,g@a=1}}{C^{H_2O}_{l} - C^{H_2O}_{g,sat}} \right) & \text{for } C^{H_2O} > C^{H_2O}_{g,sat} \end{cases} \tag{2.19}$$

In this work, the correlation by Motupally *et al.* [118] is used for $D^{H_2O}_e$, shown in Table B.2. Figure 2.3 compares Motupally *et al.*'s diffusion coefficient to this work's proposed transformation (Equation 2.19). As can be seen in Figure 2.3, $D^{H_2O}_{\lambda,eff}$ displays a discontinuity at $\lambda_{wc} = \lambda_{wc,g@a=1} = 9.2$, which corresponds to the transition between equations in Equation 2.19. For $\lambda_{wc} < \lambda_{wc,g@a=1}$, the high diffusivity is characteristic of the high mobility of the gaseous water. For $\lambda_{wc} > \lambda_{wc,g@a=1}$, any additional water is assumed to condense, which is less mobile and gives rise to a diffusivity that is more characteristic of the liquid state.

Under the case of single phase flow, the corresponding single phase diffusion coefficient is retained, while the non-existent phase's diffusion coefficient and the capillary diffusion coefficient both equal zero. Under this limit, the single-phase water concentration, equals the mixture concentration of water, as per the definition provided in Table 2.1. Therefore, in the general case, $D^{H_2O}_{lg}$ yields the form shown in Equation 2.20.

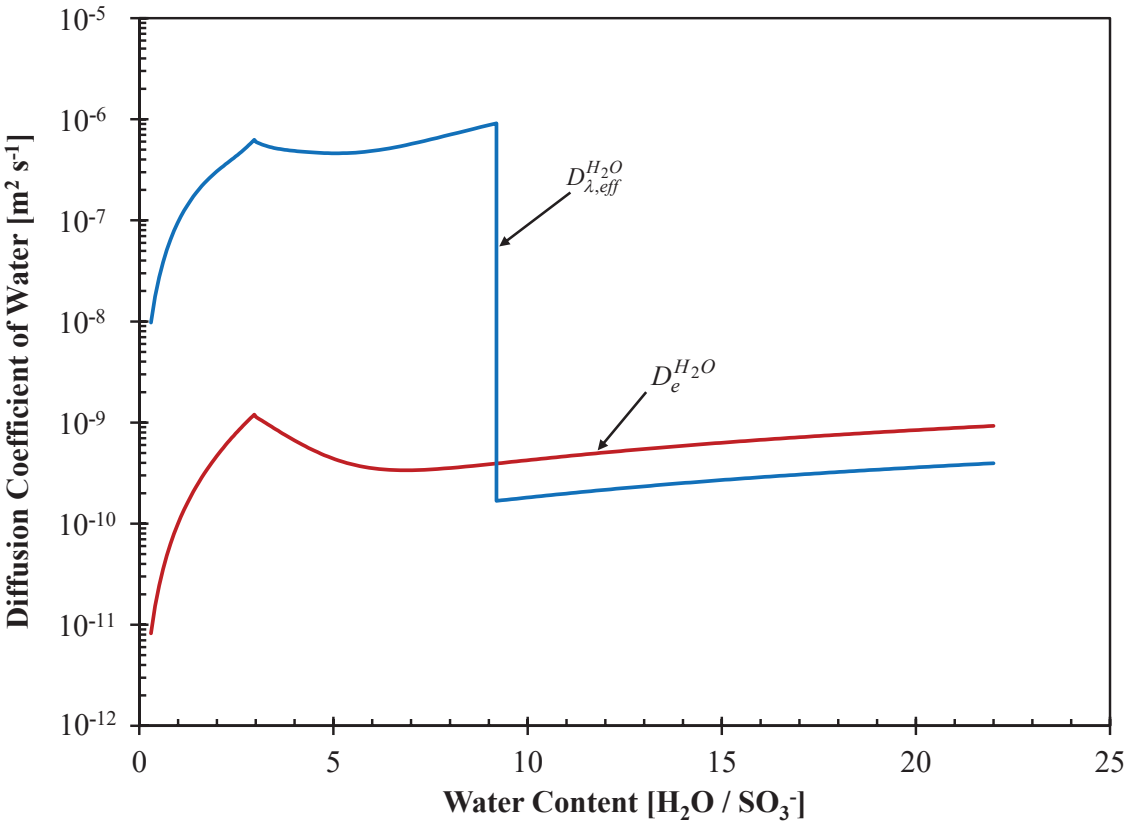

Figure 2.3: Comparison of the diffusion coefficient proposed by Mortupally *et al.* [118], and its transformation into the effective diffusion coefficient of water, $D_{\lambda,eff}^{H_2O}$ (Equation 2.19), both at 80°C.

$$D_{lg}^{H_2O} = \begin{cases} D_g^{H_2O} + D_{\lambda,eff}^{H_2O} & \text{for } C^{H_2O} \leq C_{g,sat}^{H_2O} \\ D_{cap}^{H_2O} + D_{\lambda,eff}^{H_2O} & \text{for } C_{g,sat}^{H_2O} < C^{H_2O} < C_l^{H_2O} \\ D_l^{H_2O} + D_{\lambda,eff}^{H_2O} & \text{for } C^{H_2O} = C_l^{H_2O} \end{cases} \tag{2.20}$$

The two-phase velocity of water simply takes on the mixture component of advection, as shown in Equation 2.21. The electro-osmotic drag is treated as part of water's transport source term, $S_{trans}^{H_2O}$.

$$\mathbf{u_{lg}^{H_2O}} = \gamma^{H_2O}\mathbf{u} \tag{2.21}$$

2.3.5 Conservation of Charge

The conservation of charge equation is derived from the species equation, discussed in the previous subsection, when applied to all ions within the domain. In the limit where the electro-migration flux dominates over the diffusive and convective fluxes, the species equation reduces to Ohm's Law, which is used in this work. This section details the application of this equation to determine the electronic and ionic potentials, which are subsequently used to calculate the activation polarizations and reaction rates in the CLs, and the electro-osmotic drag flux within the species equations.

Electron Transport

The electrons within the fuel cell only flow within the 'solid phase', which constists of layers made of carbon; which includes: the BLs and CLs. Furthermore, examining the reactions discussed in Chapter 1 and shown in Figure 2.1, it can be seen that electrons and protons are generated at equal rates. This electro-neutrality condition is explicitly enforced by the form shown below.

$$\nabla \cdot \left[-\sigma_s \left(\nabla \Phi_s\right)\right] = -\nabla \cdot \left[-\sigma_e \left(\nabla \Phi_e\right)\right] \tag{2.22}$$

The left and right hand sides represent Ohm's Law for the electrons and protons, respectively. It should be noted that the convention applied in this work is that electrons flow against the potential gradient, which is equivalent to having electrons flow in the opposite direction to the electric current.

Proton Transport

To solve Equation 2.22, Φ_e must first be known, and is solved from the form of Ohm's Law, shown below. It should also be noted that protons only travel within the electrolyte phase of the CLs, membranes and the FEC. Also, the terms within the divergence, represent the

ionic current, $\mathbf{i_e}$, which is used to calculate the electro-osmotic drag in Equation 2.3.

$$\nabla \cdot [-\sigma_e (\nabla \Phi_e)] = S^{\Phi}_{gen} \tag{2.23}$$

The source term on the right hand side, is directly coupled to the reaction rates in the catalyst layers. These reaction rates will be discussed in Section 2.4.2, and it will be seen that Φ_s and Φ_e are strongly coupled through S^{Φ}_{gen}. Making the solution of Equations 2.22 and 2.23 very non-linear and difficult to obtain.

2.4 Constitutive Equations

Now that each governing equation has been formulated, all that remains is a discussion on how to calculate the mixture relationships, transport properties, electrochemical properties and relationships, and source terms. These calculations are discussed in this section, beginning with the calculation of the mixture relationships.

2.4.1 Mixture Relationships

The equations used to calculate the mixture properties and relationships are presented in Table 2.1. These relationships can be thought of as the average properties of the two-phase system. For the physical meaning of each variable, the reader is referred to References [57,61]. The correlations and constants used to calculate the electrochemical and transport properties are summarized in Table B.2 of Appendix B.

2.4.2 Electrochemical Relationships

The reaction rates are given by the anode non-Tafel and cathode Tafel kinetics, given by Equations 2.24 and 2.25, respectively.

Table 2.1: Constitutive equations used to calculate the mixture fluid and transport properties.

Variable	**Expression**	**Units**
Mixture Density	$\rho = s\rho_l + (1-s)\,\rho_g$	kg m^{-3}
Mixture Molar Concentration	$C^k = sC_l^k + (1-s)\,C_g^k$	mol m^{-3}
Mixture Kinematic Viscosity	$\nu = \left(\frac{k_{rl}}{\nu_l} + \frac{k_{rg}}{\nu_g}\right)^{-1}$	m^2 s^{-1}
Relative Permeability	$k_{rl} = s^3$	-
	$k_{rg} = (1-s)^3$	-
Relative Mobility	$\lambda = k_{rl}\frac{\nu}{\nu_l}$	-
	$\sum_i \lambda_i = 1$	-
Advection Correction Factor	$\gamma^k = \frac{\rho}{C^k}\left[\lambda\frac{C_l^k}{\rho_l} + (1-\lambda)\,\frac{C_g^k}{\rho_g}\right]$	-
Capillary Diffusion Flux	$\mathbf{j_l} = \frac{\lambda(1-\lambda)\,K}{\nu}\,(\nabla P_{cap})$	kg m^{-2} s^{-1}
	$\sum_i \mathbf{j_i} = 0$	kg m^{-2} s^{-1}
Mixture Mass Flux	$(\rho\mathbf{u}) = (\rho\mathbf{u})_l + (\rho\mathbf{u})_g$	kg m^{-2} s^{-1}
Individual Phase Mass Flux	$(\rho\mathbf{u})_i = \mathbf{j_i} + \lambda_i\,(\rho\mathbf{u})$	kg m^{-2} s^{-1}
Capillary Pressure	$P_{cap} = \psi J$	Pa
Young-Laplace Coefficient	$\psi = \sigma\,(\cos\theta_c)\left(\frac{\varepsilon}{K}\right)^{1/2}$	Pa
Leverett J-Function	$J = \begin{cases} 1.417\,(1-s) - 2.120\,(1-s)^2 + 1.263\,(1-s)^3 & \text{for } \theta_c < 90^\circ \\ 1.417s - 2.120s^2 + 1.263s^3 & \text{for } \theta_c > 90^\circ \end{cases}$	-
Diffusion Coefficients	$D_l^k = D_{l,o}^k\,(\varepsilon s)^\tau$	m^2 s^{-1}
	$D_g^k = D_{g,o}^k\,(\varepsilon\,(1-s))^\tau$	m^2 s^{-1}
	$D_e^k = D_{e,o}^k\varepsilon_e^\tau$	m^2 s^{-1}

$$j = \frac{a i_{a,ref} C^M \exp\left(\frac{\alpha_a F}{\bar{R}T}\eta_a\right)}{C^M + K_a \exp\left(\frac{\alpha_a F}{\bar{R}T}\eta_a\right)} \tag{2.24}$$

$$j = a i_{c,ref} \frac{C_g^{O_2}\xi}{C_{g,ref}^{O_2}} \exp\left(\frac{\alpha_c F}{\bar{R}T}\eta_c\right) \tag{2.25}$$

The correction factor, ξ, in Equation 2.25, allows the use of the Tafel equation while accounting for the CL structure. This factor is derived in Section 2.5. The anode and cathode activation polarizations are calculated from Equations 2.26 and 2.27, respectively; which represents the potential difference across the catalyst-electrolyte interface.

$$\eta_a = \Phi_s - \Phi_e - E_a^{eq} \tag{2.26}$$

$$\eta_c = -(\Phi_s - \Phi_e - E_c^{eq}) \tag{2.27}$$

The parasitic current in the CCL, caused by the oxidation of crossed-over methanol, is assumed to follow the same reaction pathway as in the ACL, thus allowing the use of the same equation as in the ACL [8, 24]. Although the exchange current density is likely to be different than that of the anode, the exchange current density, is assumed to be identical to that of the ACL as a first approximation.

$$j_{xover} = \frac{a i_{a,ref} C^M \exp\left(\frac{\alpha_c F}{\bar{R}T}\eta_c\right)}{C^M + K_c \exp\left(\frac{\alpha_c F}{\bar{R}T}\eta_c\right)} \tag{2.28}$$

2.4.3 Source Terms

The reaction-based source terms, summarized in Table 2.2, are developed using Faraday's Law and the electrochemical relationships discussed in the previous sub-section. Although previous FE-DMFC performance models treated the removal of methanol from the FEC

Table 2.2: Summary of reaction-based source terms for each governing equation.

Symbol	Expression						
	ABL	**ACL**	**AM**	**FEC**	**CM**	**CCL**	**CBL**
S_{gen}^{MeOH}	0	$-\frac{j}{6F}$	0	0	0	$-\frac{j_{xover}}{6F}$	0
$S_{gen}^{O_2}$	0	0	0	0	0	$-\frac{j+j_{xover}}{4F}$	0
$S_{gen}^{H_2O}$	0	$-\frac{j}{6F}$	0	0	0	$\frac{j}{2F}+\frac{j_{xover}}{3F}$	0
$S_{gen}^{CO_2}$	0	$\frac{j}{6F}$	0	0	0	$\frac{j_{xover}}{6F}$	0
S_{gen}^{Φ}	0	j	0	0	0	$-(j+j_{xover})$	0

Note that the continuity source term is the summation of all species equation source terms ($S_{gen}=\sum_k M^k S_{gen}^k$); that is, for carbon dioxide, methanol, oxygen and water.

as an effective reaction-based source term, this explicit treatment is not required in this model. Instead, the introduction of water at the FEC inlet and the removal of methanol and water at the FEC outlet are accounted for by the continuity and momentum equations in the y-direction. This approach allows the model to determine the removal rates of each species and the back pressure within the FEC on its own, without the need of source terms.

The transport-based source terms, as discussed in Section 2.3.4, are summarized by Equations 2.29 and 2.30, below, for each of the species transport equations.

$$S_{trans}^{H_2O} = \nabla \cdot \left[D_{cap}^{\psi}(\nabla\psi) - \varepsilon_e n_d^{H_2O} \frac{\mathbf{i_e}}{F} \right] \tag{2.29}$$

$$S_{trans}^{MeOH} = S_{trans}^{O_2} = S_{trans}^{\Phi} = 0 \tag{2.30}$$

To ensure that the continuity equation accounts for the transport of species within the CLs' electrolyte phase, the transport source term is introduced, shown below. This source term is only valid within the CLs, elsewhere this source term equals zero.

$$S_{trans} = \nabla \cdot \left[D^{H_2O}_{\lambda,eff} M^{H_2O} \left(\nabla C^{H_2O} \right) + D^{MeOH}_{e} M^{MeOH} \left(\nabla C^{MeOH}_{l} \right) \right] \tag{2.31}$$

2.5 Spherical Agglomerate Sub-Model

The CLs in this model are considered to be composed of a packed bed of spherical agglomerates, as evidenced by Figure 1.3. A schematic of a representative single agglomerate is shown in Figure 2.4. To allow for an analytical solution to be obtained, each agglomerate is assumed to be composed of an agglomerate nucleus, with an electrolyte and water film surrounding the nucleus. These films act as a mass transport barrier to the incoming reactants. The agglomerate nucleus is assumed to be composed of dispersed carbon and catalyst particles, with the remaining space composed of Nafion®. It should be noted that in such a simplified configuration, electron and proton transport between agglomerates would not be possible, since this analysis assumes that each agglomerate is not in physical contact with one another. However, in reality, neighbouring agglomerates overlap, thus allowing current to flow [119].

As can be seen in Figure 2.4, any reactants in the surrounding pores first must dissolve into the water film and then diffuse to the center of the agglomerate, creating a large mass transport resistance. This is especially true for oxygen in the CCL, due to its low solubility in liquid water and the electrolyte phase ($k^{O_2}_{H,l} \sim 0.1$, $k^{O_2}_{H,e} \sim 0.04$, both at 80°C). Therefore, the agglomerate model was found to be an important addition. However, it was demonstrated by Nordlund and Lindbergh [120], that an agglomerate model was not necessary due to methanol's high diffusivity in Nafion®. As such, an agglomerate model was only developed for the ORR in the CCL.

Therefore, the reaction rates are assumed to follow Equations 2.24, 2.25 and 2.28. The

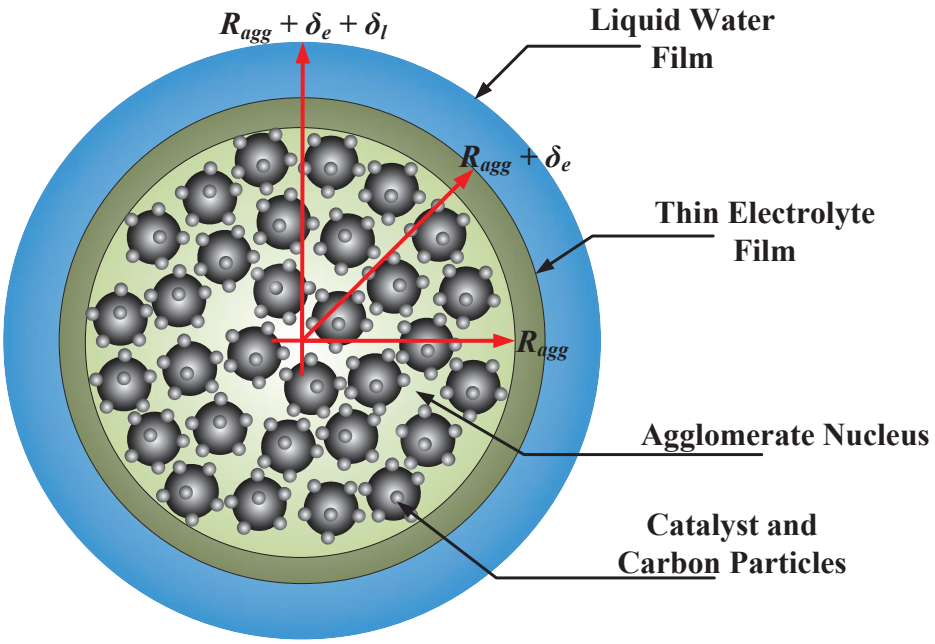

Figure 2.4: Schematic of a spherical agglomerate. The agglomerate nucleus has a radius of R_{agg}, while the electrolyte and water film thicknesses are δ_e and δ_l, respectively.

agglomerate correction factor, ξ, will link the microstructure of the CL to the macroscopic model. This sub-section will be devoted to developing an expression for ξ. Given that the electrochemical reactions only takes place within the agglomerate nucleus, a resistance model can be applied within the water and electrolyte films. The expressions for the molar flow rate, $\dot{N}^{O_2}$, and effective film resistance, h^{O_2}, are shown below. In Equation 2.32a, $C^{O_2}_{surf}$ and $C^{O_2}_{nuc,surf}$, represent the concentrations at $r = R_{agg} + \delta_e + \delta_l$ and $r = R_{agg}$, respectively.

$$\dot{N} = \frac{C^{O_2}_{surf} k^{O_2}_{H,l/e} - C^{O_2}_{nuc,surf}}{h^{O_2}} \tag{2.32a}$$

$$h^{O_2} = \frac{1}{4\pi D^{O_2}_e} \cdot \frac{\delta_e}{R_{agg}(R_{agg} + \delta_e)} + \frac{k^{O_2}_{H,l/e}}{4\pi D^{O_2}_l} \cdot \frac{\delta_l}{(R_{agg} + \delta_e)\,(R_{agg} + \delta_e + \delta_l)} \tag{2.32b}$$

Here, $k^{O_2}_{H,l/e}$ accounts for the differences in oxygen solubility in the water and electrolyte films [121]. To maintain the same form of each equation presented in this sub-section, regardless of whether the flow is single or two-phase, $k^{O_2}_{H,l/e}$ is given the following form.

$$k_{H,l/e}^{O_2} = \begin{cases} \dfrac{k_{H,l}^{O_2}}{k_{H,e}^{O_2}} & \text{for } \delta_l > 0 \\ 1 & \text{for } \delta_l = 0 \end{cases} \tag{2.33}$$

To define the oxygen consumption rate, the volume averaged electrochemical reaction rate across the agglomerate nucleus is determined. This is given by the terms on the first right hand side. This reaction rate can also be determined from a flux balance at $r = R_{agg}$, through application of Equation 2.32a. This flux balance is given by the second right hand side of the equation below. The term, n_{agg}, represents the number of agglomerates per unit volume of the whole CL; thus converting the molar flow rate to a molar volumetric flow rate.

$$S_{gen}^{O_2} = (1-\varepsilon)k_c E C_{nuc,surf}^{O_2} = n_{agg}\frac{C_{surf}^{O_2}k_{H,l/e}^{O_2} - C_{nuc,surf}^{O_2}}{h^{O_2}} \tag{2.34}$$

Here, k_c is the reaction rate within the agglomerate, and E and ϕ_R are the agglomerate effectiveness factor and Thiele's modulus, given by Equations 2.35a and 2.35b, respectively.

$$E = \frac{3}{\phi_R^2}\Big[\phi_R(\coth\phi_R) - 1\Big] \tag{2.35a}$$

$$\phi_R = R_{agg}\sqrt{\frac{k_c}{D_{e,nuc}^{O_2}}} \tag{2.35b}$$

By applying Equation 2.34, an expression for $C_{nuc,surf}^{O_2}$ can be determined, to provide a new expression for $S_{gen}^{O_2}$. This new expression is shown below.

$$S_{gen}^{O_2} = C_{surf}^{O_2}k_{H,l/e}^{O_2}\frac{n_{agg}(1-\varepsilon)k_c E}{n_{agg} + (1-\varepsilon)h^{O_2}k_c E} \tag{2.36}$$

To ensure Equation 2.36 and the homogeneous reaction model (Equation 2.25 without ξ) are consistent in the limit where R_{agg} and $\delta_e \to 0$, Equation 2.36 is applied to this limit and equated to the homogeneous model to provide an expression for k_c, shown below.

$$k_c = \frac{a i_{oc,ref}}{4F(1-\varepsilon) C_{g,ref}^{O_2} k_{H,l/e}^{O_2}} \exp\left(\frac{\alpha_c F}{\bar{R}T}\eta_c\right) \tag{2.37}$$

After substituting Equation 2.37 into Equation 2.36, and rearranging the expression such that it is in the form of Equation 2.25, the agglomerate correction factor, ξ, takes the form shown below. In the case where $s > 0$, a water film is assumed to be present. This requires oxygen to first dissolve into the water film, as given by $k_{H,l}^{O_2}$. When $s = 0$, no water film is present, thus requiring oxygen to only dissolve into the electrolyte film, given by $k_{H,e}^{O_2}$.

$$\xi^{O_2} = \frac{n_{agg} E}{n_{agg} + (1-\varepsilon) h^{O_2} k_c E} \begin{cases} k_{H,l}^{O_2} & \text{for } \delta_l > 0 \\ k_{H,e}^{O_2} & \text{for } \delta_l = 0 \end{cases} \tag{2.38}$$

2.5.1 Catalyst Layer Porous Properties

To determine both of the CLs' porous properties from their compositions, a series of mass and volume balances are applied. The porosity, shown below, was calculated through a volume balance of the CL [122].

$$\varepsilon = 1 - \frac{m''_{Pt}}{f_{Pt} t_{CL}} \left[\frac{f_{Pt}}{\rho_{Pt}} + \frac{f_{Ru}}{\rho_{Ru}} + \frac{1 - f_{Pt} - f_{Ru}}{\rho_C} + \frac{f_e}{(1-f_e)\,\rho_e}\right] \tag{2.39}$$

Here, f denotes the mass fraction of each component of the CL, while m'' denotes the mass loading, given in units of kg m^{-2} of apparent CL area [122]. The expressions for each mass fraction are shown below, and all mass loadings are assumed to be known.

$$f_{Pt} = \frac{m''_{Pt}}{m''_{Pt} + m''_{Ru} + m''_C} \tag{2.40a}$$

$$f_{Ru} = \frac{m''_{Ru}}{m''_{Pt} + m''_{Ru} + m''_C} \tag{2.40b}$$

$$f_C = \frac{m''_C}{m''_{Pt} + m''_{Ru} + m''_C} \tag{2.40c}$$

$$f_e = \frac{m''_e}{m''_{Pt} + m''_{Ru} + m''_C + m''_e} \tag{2.40d}$$

The volume fractions of the solid and electrolyte phases, ε_s and ε_e, can also be determined in a similar fashion to Equation 2.39. The final forms of the equations are shown below.

$$\varepsilon_s = \frac{m''_{Pt}}{f_{Pt} t_{CL}} \left[\frac{f_{Pt}}{\rho_{Pt}} + \frac{f_{Ru}}{\rho_{Ru}} + \frac{1 - f_{Pt} - f_{Ru}}{\rho_c} \right] \tag{2.41a}$$

$$\varepsilon_e = \frac{m''_{Pt}}{f_{Pt} t_{CL}} \frac{f_e}{(1 - f_e)\, \rho_e} \tag{2.41b}$$

Through geometry, referring to Figure 2.4, n_{agg} can be determined as shown below. Here, R is the combined radius of the agglomerate nucleus and electrolyte film thickness, and is assumed to be known in this model.

$$n_{agg} = \frac{3(1 - \varepsilon)}{4\pi R^3} \tag{2.42}$$

If the volume fraction of electrolyte within the agglomerate nucleus, $\varepsilon_{e,nuc}$, is known, then by geometry and through use of Equation 2.42, an expression for the agglomerate nucleus radius, r_{agg}, can be derived. The final form is shown below [123].

$$r_{agg} = R \left[\frac{1 - \varepsilon - \varepsilon_e}{(1 - \varepsilon_{e,nuc})(1 - \varepsilon)} \right]^{1/3} \tag{2.43}$$

Similarly, the electrolyte and water film thicknesses, δ_e and δ_l, are shown below.

$$\delta_e = R_{agg} - r_{agg} \tag{2.44}$$

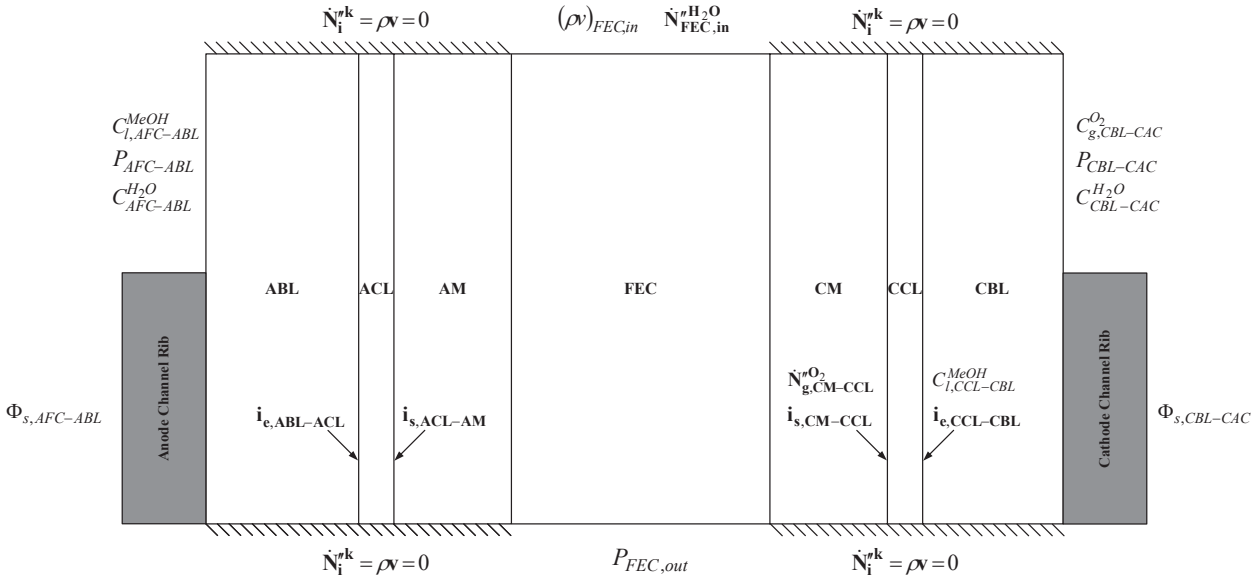

Figure 2.5: Boundary conditions used in the proposed model. The variables mentioned in the figure are values that are set as a boundary condition for the corresponding variable. The values of these variables are found in Table B.1.

$$\delta_l = R\left[\left(1 + \frac{\varepsilon s}{1-\varepsilon}\right)^{1/3} - 1\right] \tag{2.45}$$

2.6 Boundary Conditions

A schematic of the locations of the boundary conditions are shown in Figure 2.5, while the values and expressions for these boundary conditions are listed in Table B.1. The boundary conditions were chosen to be conditions that are easily controlled during the experiments conducted in this study. A more detailed explanation of these boundary conditions, and the regions in which each governing equation is confined to, are also described below. It should also be noted that the reduced area caused by the presence of the ribs was only accounted for in the electron transport equations. The reduced area in the mass, momentum and species transport equations caused non-convergent simulations and was not included for these equations. The ribs presented in Figure 2.5 are assumed to be equal to total thickness of each rib in the corresponding compartment.

- The continuity and momentum equations are solved throughout the whole domain, and known pressures are applied at the outer-most boundaries, except for the FEC inlet which has a known flow rate.

- The methanol concentration profile is solved from the AFC-ABL interface to the CCL-CBL interface, and each interface has a known concentration. An outlet condition is placed at the FEC outlet.

- The water concentration profile is solved throughout the whole domain and has known concentrations at the outer-most boundaries. A known molar flux and outlet condition are placed at the FEC inlet and outlet respectively.

- The oxygen concentration profile is confined to the cathode, and thus has a known concentration at the inlet and a no flux condition at the CM-CCL interface.

- The electron transport equations are solved within the anode and cathode, and have known potentials at the outer-most boundaries and no flux conditions at both CL-membrane interfaces.

- The proton transport equations are solved from electrode to electrode, where no flux conditions are applied at both boundaries.

2.7 Numerical Details

In the presented model, each governing equation was fit into the form of the 2D convective-diffusion-reaction equation, shown in Equaton 2.46. Here, Γ is the diffusion coefficient, $\mathbf{u}$ is the velocity, and S is a source term, each for an arbitrary variable ϕ.

$$\nabla \cdot \left[-\Gamma^{\phi} \left(\nabla \phi \right) + \mathbf{u}^{\phi} \phi \right] = S^{\phi} \tag{2.46}$$

Although the governing equations are set in 2D form, only one control volume in the

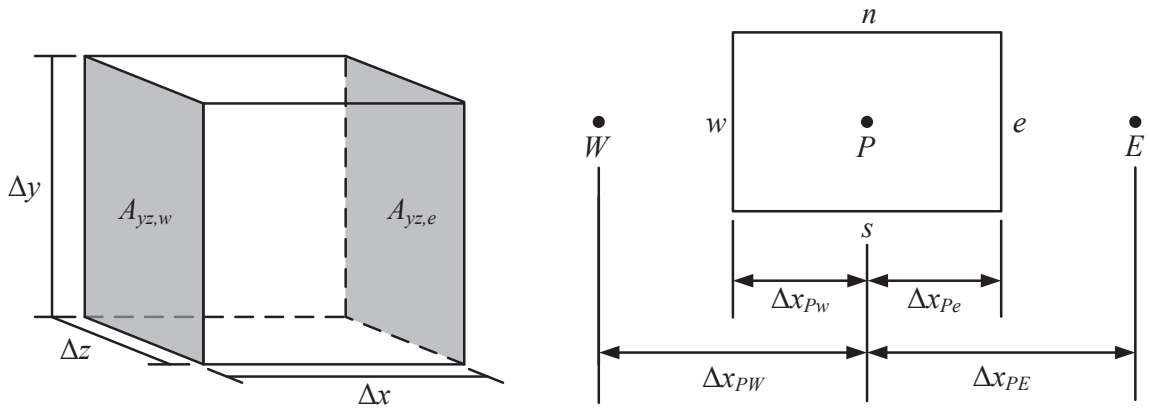

Figure 2.6: Schematic of a representative control volume and their dimensioning in the x-direction. The same approach is used for the y-direction.

y-direction is used. This allowed for a 1D problem to be formulated, that also accounted for the flow in the y-direction. Each equation was linearized using the finite volume method and solved using an in-house code written in MATLAB. The 2D discretized form of Equation 2.46 is shown below, where a represents a matrix coefficient and its subscripts W, E and P represent the nodal position at the west and east locations, relative to point P; as shown in Figure 2.6. All scalar variables were evaluated at the control volume centers (points W, P and E), while vectors were evaluated at the control volume faces (points w, e, n and s). The term $\bar{S}_P$ is the source term averaged over the differential volume, V_{xyz}, and F^{ϕ} is the flux.

$$- a_W \phi_W + a_P \phi_P - a_E \phi_E = \bar{S}_P V_{xyz} + (F_n^{\phi} - F_s^{\phi}) A_{xz} \tag{2.47}$$

The diffusive terms were discretized using central differencing, while the convective terms were estimated using the hybrid differencing scheme. This gives the form of the matrix coefficients shown below [124]. Here, Δx is the grid spacing in the x-direction, while A_{yz} is the surface area of the corresponding control volume face, as shown in Figure 2.6. The same approach is applied in cases where F^{ϕ} is to be determined in the y-direction.

$$a_W = A_{yz,w} \max \left[u_w^{\phi}, \left(\frac{\Gamma_w^{\phi}}{\Delta x_{PW}} + u_w^{\phi}(1 - f_w) \right), 0 \right] \tag{2.48a}$$

$$a_E = A_{yz,e} \max\left[-u_e^{\phi}, \left(\frac{\Gamma_e^{\phi}}{\Delta x_{PE}} - u_e^{\phi}(1 - f_e)\right), 0\right] \tag{2.48b}$$

$$a_P = a_W + a_E + (u_e^{\phi} A_{yz,e} - u_w^{\phi} A_{yz,w}) \tag{2.48c}$$

The factors f_e and f_w account for differences in grid spacing across the control volume faces and thus have the form shown below.

$$f_w = \frac{\Delta x_{wW}}{\Delta x_{PW}} \tag{2.49a}$$

$$f_e = \frac{\Delta x_{eE}}{\Delta x_{PE}} \tag{2.49b}$$

The interfacial diffusion coefficients, Γ_w and Γ_e, were estimated with the harmonic mean, as shown below [125], while all other interfacial scalars were linearly interpolated.

$$\Gamma_e = \frac{\Delta x_{PE}}{\frac{\Delta x_{Pe}}{\Gamma_P} + \frac{\Delta x_{eE}}{\Gamma_E}} \tag{2.50a}$$

$$\Gamma_w = \frac{\Delta x_{PW}}{\frac{\Delta x_{Pw}}{\Gamma_P} + \frac{\Delta x_{wW}}{\Gamma_W}} \tag{2.50b}$$

This approach allowed for the pressure and velocity fields to be efficiently solved using the SIMPLE algorithm; which is an iterative pressure-correction method used to couple and solve the continuity and momentum equations [124]. All other discretized scalar equations (Equation 2.47) were arranged in a tri-diagonal matrix and solved using Thomas' algorithm. The boundary conditions were implemented using the 'ghost node' approach.

The model was initiated with an initial guess, that was subsequently improved as each governing equation was solved iteratively. The solution was deemed converged if the sum of

the relative differences of each converged variable ($\phi = \{\mathbf{u}, \mathbf{v}, P, C_l^M, C_g^{O_2}, C^{H_2O}, \Phi_e, \Phi_s, \mathbf{I}\}$) at each location was less than 10^{-5} for three consecutive global iterations. This condition is shown in Equation 2.51. When solving for a specific variable, the convergence criterion was set to two orders of magnitude lower than the global convergence criterion. The solution procedure used for this model is summarized in Figure 2.7. Due to the non-linearity and sensitivity of the governing equations, several techniques had to be used to ensure a robust model. These issues and their proposed solutions are discussed in Section 2.7.1.

$$R_{total} = \left(\sum_{\phi} \sum_{x} \frac{\left| \left(|\phi^{new}| - |\phi^{old}| \right) \right|}{|\phi^{new}|} \right) < 10^{-5} \tag{2.51}$$

It should also be noted that the thermo-physical properties of all fluids were determined using compiled data from NIST [126], while the sulfuric acid conductivity was determined from data collected by Darling [127]. The boundary and operating conditions used in this study can be found in Table B.1, while the electrochemical properties can be found in Table B.2. The fuel cell dimensions, material properties are shown in Table B.3.

2.7.1 Numerical Challenges and Stability Considerations

Three major challenges, listed below, are discussed in this section. These challenges stem from the inherent properties, non-linearity and sensitivity of the governing equations and geometry of the fuel cell. Although some of these challenges are not unique to FE-DMFCs, the approaches used to solve these issues are often not discussed in literature. Therefore, for completeness, these challenges and the solution used in this work are discussed in this sub-section. The observed challenge is first mentioned in italics, and the proposed solution applied to this work is then discussed.

1. *From one internal iteration to the next, the solution of some variables can oscillate between different solutions due to their high sensitivity. This can either lead to non-convergent simulations or long computational times.*

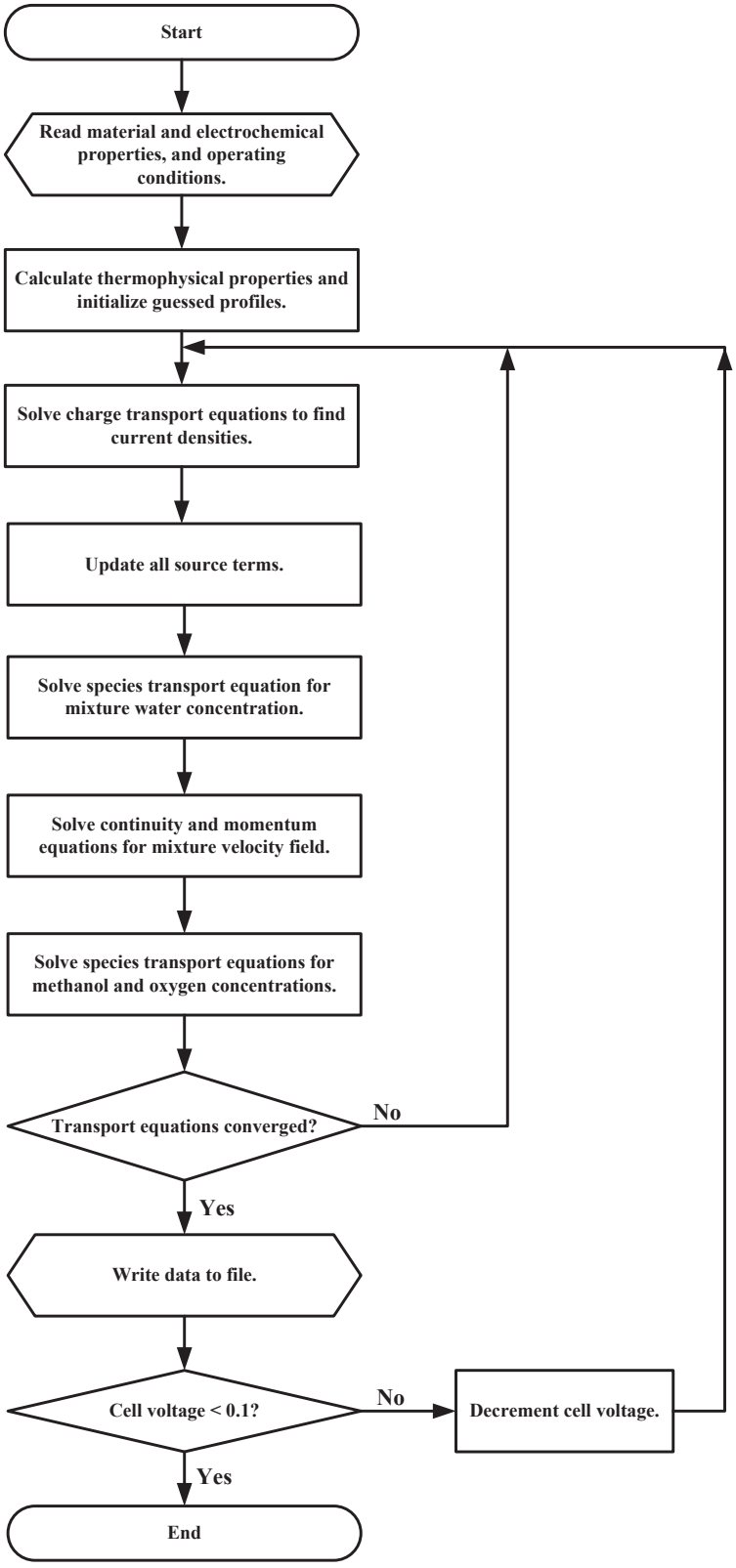

Figure 2.7: Flow chart showing the solution process for the proposed model.

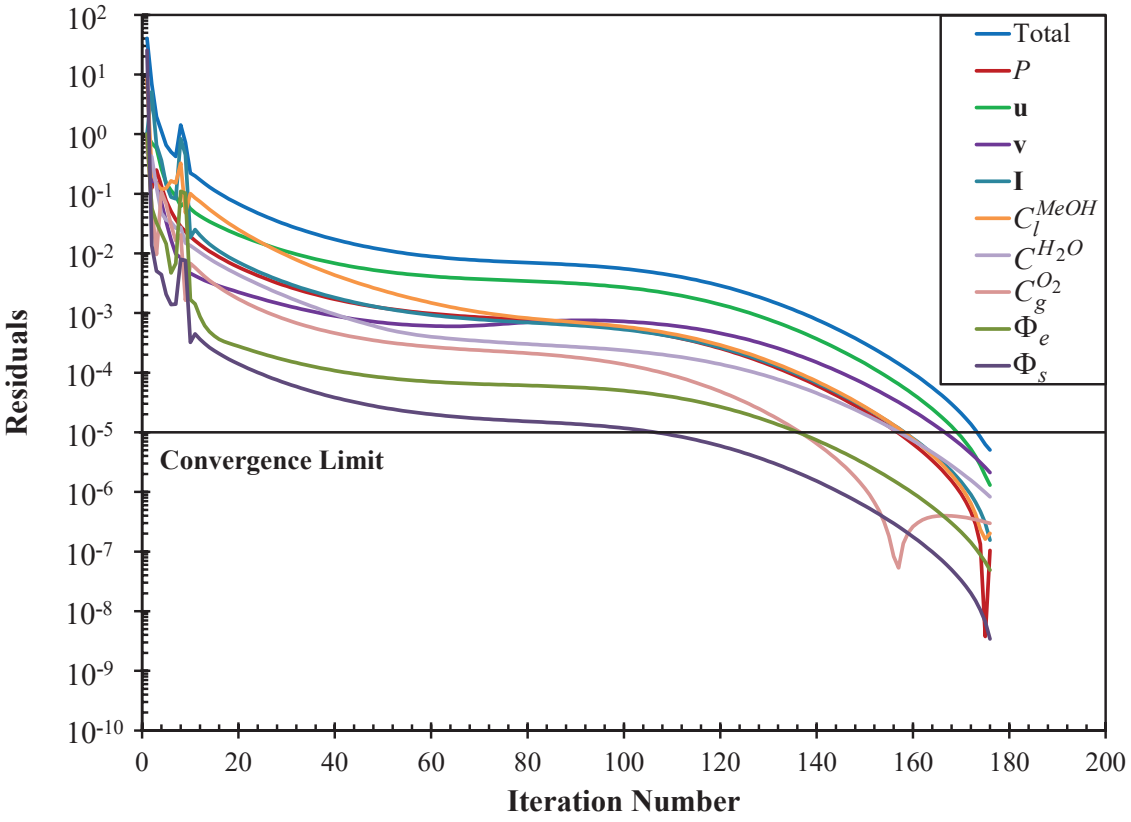

Figure 2.8: Convergence history for a typical simulation at 0.1 V.

Much of the solution's non-linearity stems from each variable's sensitivity, primarily their diffusion coefficient and effective two-phase velocity, to the liquid saturation and water content profiles. To maximize the chance of a successfully converged solution, a good initial guess had to be provided. This came from a simplified model, that assumed that all diffusion coefficients were constant. The solution to this scenario provided the initial guess to the actual model, where the diffusion coefficients were allowed to vary as governed by their constitutive equations. To stabilize the solution, an under-relaxation procedure, shown below, was used at the end of each internal iteration. In this work, the under-relaxation factor, ω, ranged from 0.5 – 1. More sensitive variables, such as C^{H_2O} and Φ_e required an $\omega < 1$.

$$\phi^{updated} = \omega\phi^{new} + (1-\omega)\phi^{old} \tag{2.52}$$

2. *The charge conservation equations are very sensitive due to their source terms' exponential dependency on Φ_e and Φ_s (see Equations 2.24 to 2.27). Without special care, these transport equations can easily diverge. Also, the proton transport equation's boundary conditions have zero flux conditions at the ABL-ACL and CCL-CBL interfaces. On their own, this set of conditions are insufficient to provide a unique solution, since Φ_e can take on any value as long as the slope at the boundaries are achieved. Therefore, a robust approach will be required to solve the charge transport equations, along with an additional condition to find a unique solution.*

To ensure a robust yet relatively simple approach to solve the charge transport equations, a predictor-corrector approach was applied. The prediction step was performed by solving both the proton and electron transport equations through Thomas' algorithm as previously described. To ensure a stable solution, it was found that the proton source term had to be linearized using a first-order Taylor series expansion with respect to Φ_e, as shown below. The first set of bracketed terms were solved using the information at the current iterative step, while the second set of terms were solved simultaneously with the solution. The MOR's source term gradient was determined analytically, whereas the ORR's source term gradient was determined numerically.

$$S_{gen}^{\Phi} = \left[S_{gen}^{\Phi,current} - \frac{\partial S_{gen}^{\Phi,current}}{\partial \Phi_e} \Phi_e^{current} \right] + \frac{\partial S_{gen}^{\Phi,current}}{\partial \Phi_e} \Phi_e^{updated} \tag{2.53}$$

The corrector step ensured that the total current generated in the ACL was consumed in the CCL, as shown below.

$$\int_{V_{ACL}} j \cdot dV = \int_{V_{CCL}} j \cdot dV \tag{2.54}$$

By linearizing Equation 2.54 as before, but with respect to the current and previous iterative steps, Equation 2.54 takes the form shown below [128].

$$\Phi_e^{new} = \Phi_e^{current} - \frac{\int_{V_{ACL}} j \cdot dV - \int_{V_{CCL}} j \cdot dV}{\int_{V_{ACL}} \frac{\partial j}{\partial \Phi_e} \cdot dV - \int_{V_{CCL}} \frac{\partial j}{\partial \Phi_e} \cdot dV} \tag{2.55}$$

It should be noted that the current density gradients, found in Equation 2.53, are very sensitive and at times caused unrealistic predictor step solutions. This in turn caused the corrector step, Equation 2.55, to fail. In such a case, the bisection search method was applied as a fail safe for that iteration. Once the solution was in a more stable region, the correction approach would default back to Equation 2.55.

3. *The value of ψ across material layer interfaces can be discontinuous. However, based on this work's formulation, this would cause $\mathbf{j_l} = \infty$, which is not physically meaningful, since P_{cap} is assumed to be continuous in this work. Therefore an approach to circumvent this issue was required.*

In literature, it is common to assume that the porous properties discontinuously vary across mating layer interfaces. However, as mentioned in the problem statement, this would give rise to $\nabla\psi = \nabla P_{cap} = \infty$; which is not physically meaningful. To bypass this issue, it was assumed that K and ψ both smoothly but rapidly vary across material interfaces. This assumption seems plausible, since the hot pressing procedure is designed to fuse the CL to the membrane, as well as ensure good electrical contact between the CL and the rest of the MEA. Furthermore, the applied pressure during

this process will likely force a portion of the adjacent layers into each other. The same effect is expected to occur when the fuel cell is fully assembled and fastened shut.

To account for these transitions, each layer's K and ψ were individually multiplied by a pulse function, shown below, which acts as a weighting factor, ranging in value between 0 and 1. A pulse value of 0 turns the material property "off", and a value of 1 turns the material property "on". To obtain the overall distribution, this pulse function is applied to each diffused variable in each layer, where the position, x, covered the full computational domain for all layers. From there, each layer's diffused variable are added together. Figure 2.9 displays examples of pulses for different values of the pulse diffusion index, δ. The remaining variables in Equation 2.56, $x_{trans,1}$ and $x_{trans,2}$, represents the locations of the pulse function's inflection points.

$$\vartheta = \frac{1}{2}\left[\tanh\left(\frac{x - x_{trans,1}}{\delta}\right) - \tanh\left(\frac{x - x_{trans,2}}{\delta}\right)\right] \tag{2.56}$$

Since a balance is required between accuracy, stability and computational time, a parametric study was conducted on δ, where its value was varied from 1 μm to 100 μm. It was found that although the concentration and velocity profiles were diffused due to the choice of δ, the final solution, consisting of polarization curves, methanol and water crossover fluxes and maximum power output, varied by no more than 0.6%. This insensitivity suggests that this could be a useful approach in large scale and multidimensional simulations where a large number of nodes are required, since the liquid saturation jumps can be resolved with a small additional computational cost; presuming a large δ can be applied. In the simulations presented in this work, δ was set to 1 μm such that the jumps can be treated as closely as possible to a sharp interface as is typically shown in literature.

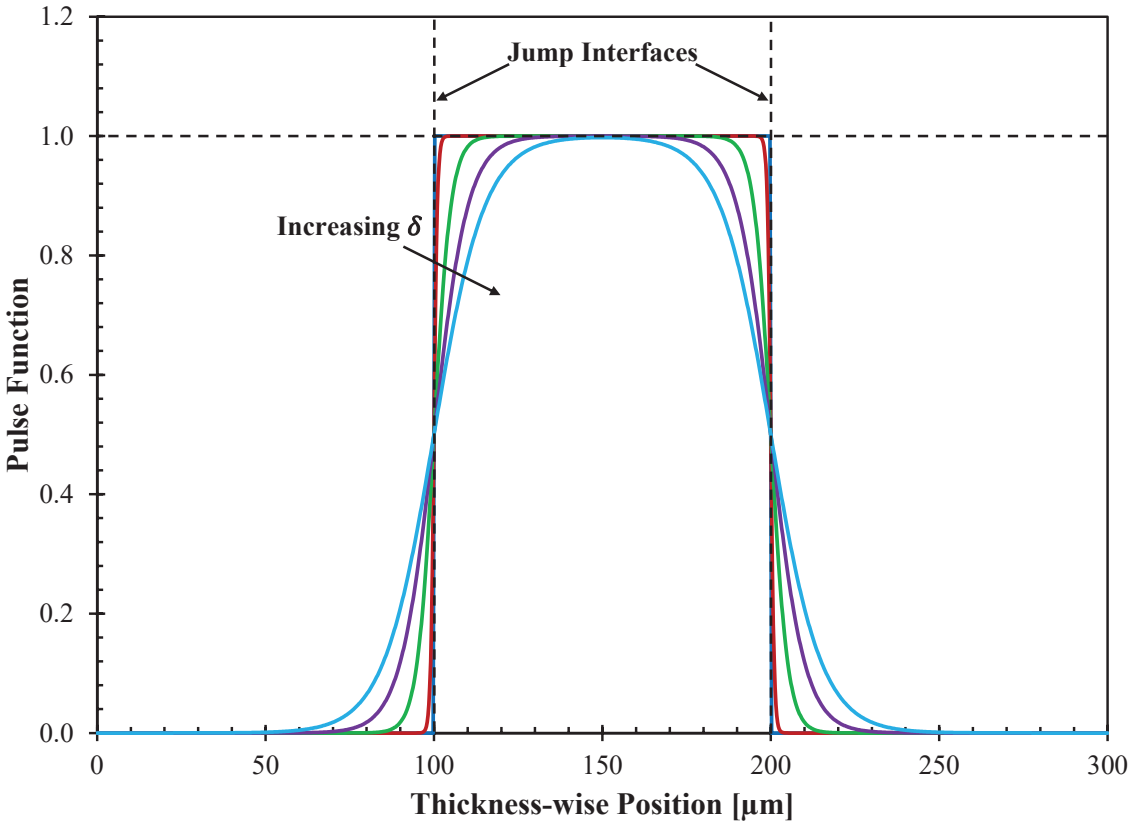

Figure 2.9: Sample pulse functions using Equation 2.56, with $\delta = 0.01$, 1, 5, 10, 15 and 20 μm, and the inflection points of the pulses are arbitrarily placed at 100 and 200 μm.

It should be noted that K and ψ were chosen to be used with the pulse function, as these two parameters minimized the distortion to the remaining variables, which included over and undershoots across the interface. This distortion arose from the multiplication of locally diffused and undiffused variables and due to the differences in magnitude that each variable varied across the interface. Although this distortion could be physical, it is not known how each variable actually varies across the interface. Therefore, to obtain consistent trends with literature, these two variables were chosen.

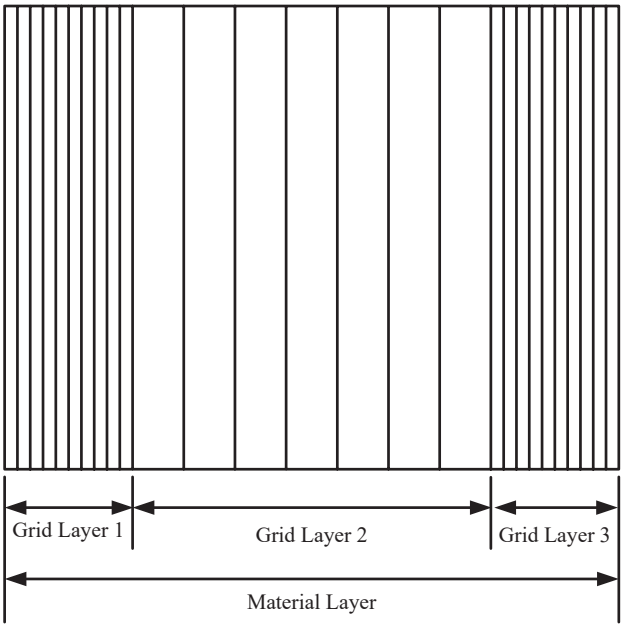

Figure 2.10: Schematic of the grid refinement approach used in this work, for an arbitrary material layer. Each grid layer has its own specified thickness and specified number of body-fitted nodes. This refinement template is repeated for each material layer.

2.8 Grid Generation and Independence

In this model, both P and especially C^{H_2O} have sharp gradients near material interfaces. Without sufficient grid resolution, the diffused interface will not be properly resolved, potentially causing near infinite velocities to be observed. This will then cause modeling errors which would propagate through the remaining solution. Therefore, this section details the grid generation and refinement procedure for each layer, and the approach used to determine the number of nodes required to achieve a grid independent solution.

2.8.1 Grid Generation

A disadvantage of the proposed model is that significant grid refinement is needed near regions that have dissimilar values of ψ. Although this issue could take advantage of an adaptive grid refinement technique, a simplified approach was adopted; whereby each material layer was split into 3 grid layers, each with a specified thickness and number of nodes. Within each grid layer, the nodes were uniform in size and fit to the specified grid layer

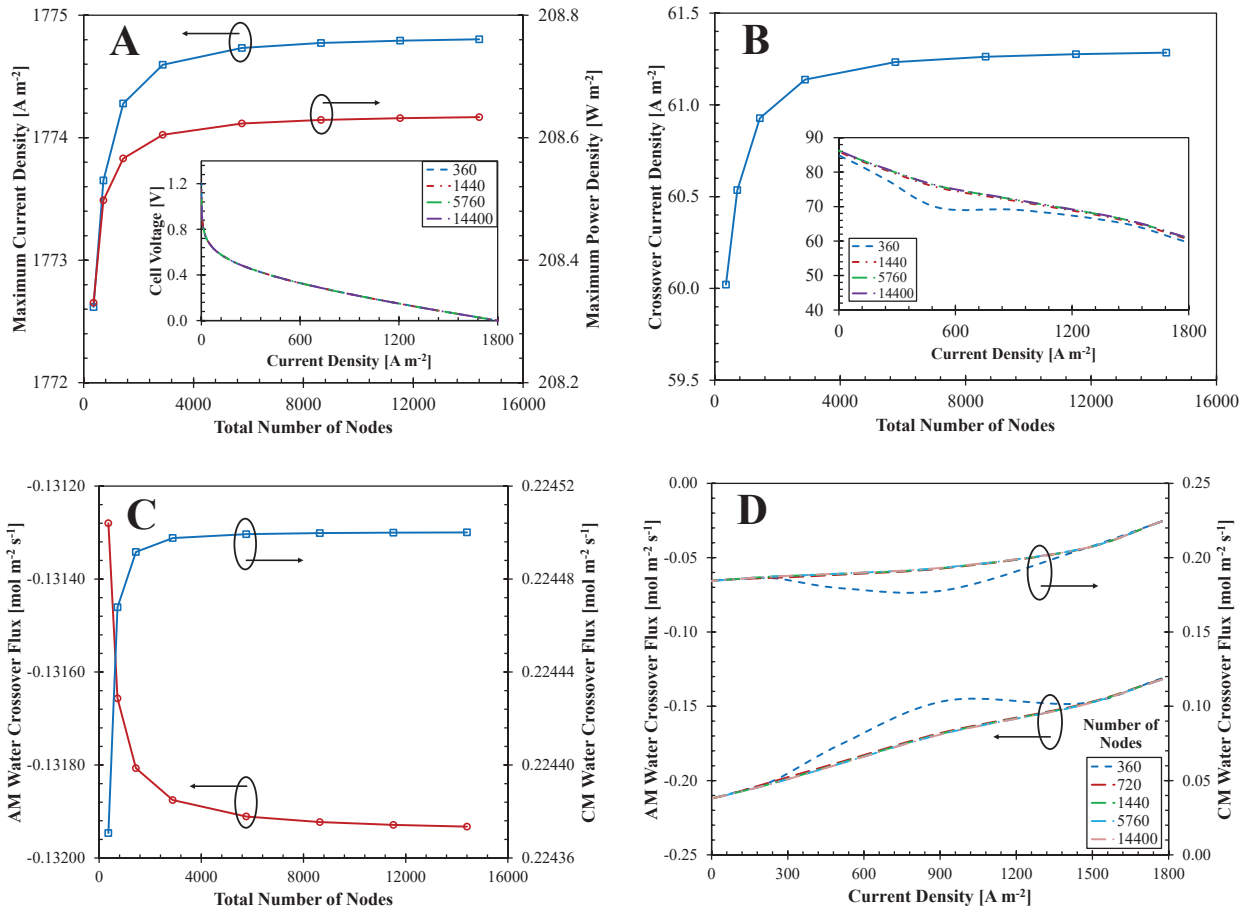

Figure 2.11: Comparison of baseline numerical results at different levels of grid refinement. The results in a-c are for a cell voltage of 0.1 V, whereas the results in d and within each sub-figure are for cell voltages from open circuit to 0.1 V.

thickness. This approach is shown schematically in Figure 2.10. To accurately capture the transition between each layer, the thickness of the refinement region was chosen to be the distance from the material interface to the location where the diffused ψ deviates by 1% from its undiffused value. It was found that a total of 2880 nodes (320 nodes in the BLs, FEC and membranes, and 640 nodes in the CLs) were needed for a grid independent solution. This was determined through a grid independence study, discussed in the next sub-section.

2.8.2 Grid Independence

Although it is common to use the fuel cell's performance (such as the polarization curve [119], or current density [129]) as a metric for grid independence. Mazumder [130] reported that in some cases the internal fluxes may still be far from grid independent even when the polarization curve or current density have reached grid independence. Therefore, in this study, the grid independence study was conducted in two steps. The first step involved the individual grid refinement of each material layer, with the nodes uniformly distributed across each grid layer. Once each material layer individually achieved grid independence, the second step was to continually double the number of nodes in all material layers simultaneously, until grid independence was achieved. In each case, grid independence was gauged on the relative difference of the polarization curves, maximum current and power densities, and methanol and water crossover fluxes, relative to the previous grid's solution. The simulation was deemed grid independent if the relative difference of all solutions between two grids was $\pm 0.5\%$.

To provide representative results, Figure 2.11 displays the comparison between each parameter used in the grid independence study at each grid size. Figures 2.11a-c are for a cell voltage of 0.1 V, whereas each sub-figure and Figure 2.11d are for the full current density range. As can be seen in Figure 2.11a, there was negligible change in the predicted performance with each grid size. However, examining the other figures shows that the internal fluxes are not initially grid independent. At small grid sizes, the simulation results deviated by as much as 13% from the converged results. This difference arises from the sensitivity of the water transport's two-phase diffusion coefficient, which affected the liquid saturation profile. However, by increasing the grid resolution, the simulations asymptotically approached a final converged result. A total grid size of 2880 nodes was deemed sufficient for grid independence.

Chapter 3

Model Verification and Validation

To test the model's accuracy, this chapter compares the predictions from the numerical model from Chapter 2 with three different test cases, summarized below. These test cases were chosen to ensure that the numerical model is capable of predicting the relevant physics within the fuel cell as well as provide accurate trends. A discussion of the results is presented within this chapter, while more detailed information concerning the derivations and experiments are found in Appendices C to F.

- A comparison to the analytical solution for a liquid saturation jump
- A comparison to the analytical single phase solution for the FE-DMFC
- A comparison to in-house experimental FE-DMFC data

3.1 Test Case 1 – Comparison to an Analytical Liquid Saturation Jump Model

In this test case, the numerical model is compared to an analytical solution where liquid water enters a domain with two mating materials of dissimilar porous properties yielding a liquid saturation jump. It is assumed that the mass flux entering the domain is constant and known at $x = 0$, and there is a known and constant liquid saturation at $x = t_1 + t_2 = L$; as

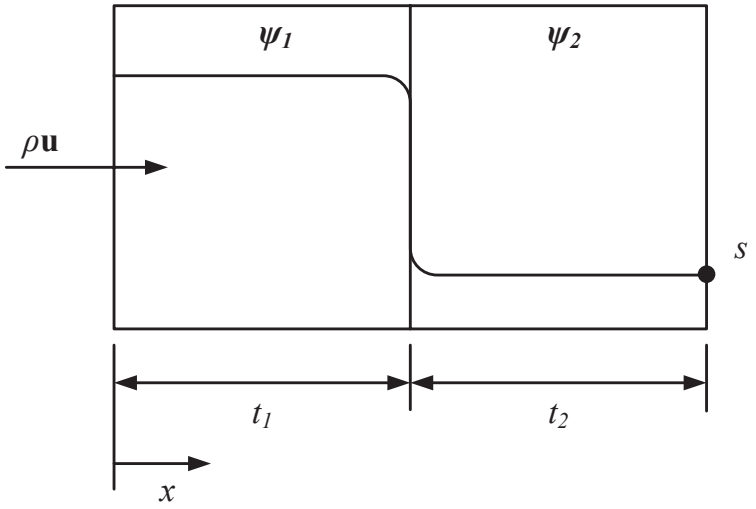

Figure 3.1: Schematic of two adjacent layers with differing Young-Laplace coefficients, where the mass flux at $x = 0$, and the liquid saturation at $x = t_1 + t_2$ are known.

defined in Figure 3.1. The derivation is provided in Appendix C, while the final equations are given by Equations 3.1a and 3.1b, for Layers 1 and 2 respectively. Here, $D = K\psi/\nu_l$, whereas $f\big|_{t_1}$ and $f\big|_L$ represent the left hand side value of Equations 3.1a and 3.1b, at $x = t_1$ and L, respectively. The remaining details for this test case are provided in Table 3.1.

$$s^4\left(0.63150s^2 - 0.84800s + 0.35425\right) = f\big|_{t_1} + \frac{(\rho u)_l}{D_1}(x - t_1) \tag{3.1a}$$

$$s^4\left(0.63150s^2 - 0.84800s + 0.35425\right) = f\big|_{L} + \frac{(\rho u)_l}{D_2}(x - L) \tag{3.1b}$$

Figure 3.2 displays the comparison between the numerical (dashed line) and analytical (solid black line) solutions for the case where Layer 1's contact angle is varied. As can be seen, there is excellent agreement between the analytical and numerical results, with $< 0.5\%$ relative difference between the results in the range of $95 \geq x \geq 105$ μm. However, near the liquid saturation jump, within the range of $95 < x < 105$ μm, the relative difference approached 50% for the cases with largest step changes, $\theta_c = 100°$ and $135°$. The large deviation in this range is expected, as the analytical solution treats the change in ψ between layers as a step change, where the numerical model artificially diffuses this transition. The

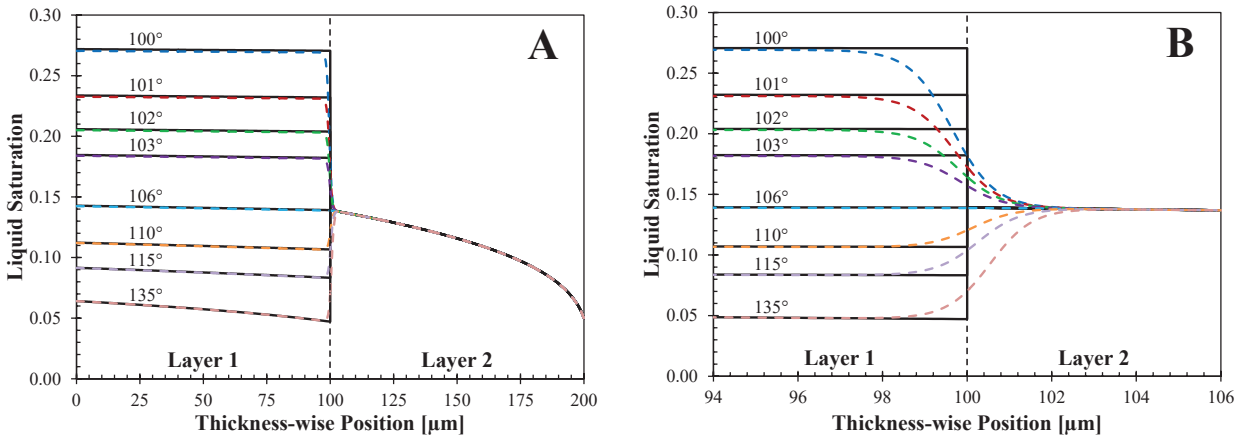

Figure 3.2: Comparison of the analytical (black line) and numerical (dashed coloured lines) MMM solutions of the saturation jump equations, for the case where Layer 1's contact angle is varied as shown in the graphs. a) Displays the full range of the two layers, whereas b) displays the solutions near the mating layers' interface.

Table 3.1: Summary of the boundary conditions, and geometric and porous properties of the two layers used for Test Case 1.

Variable	Symbol	Value	Units
Layer 1			
Thickness	t	100	μm
Permeability	K	10^{-13}	m^2
Porosity	ε	0.5	–
Contact Angle	θ_c	Varied	$^\circ$
Liquid Phase Velocity	u_l	1	μm s^{-1}
Layer 2			
Thickness	t	100	μm
Permeability	K	10^{-14}	m^2
Porosity	ε	0.5	–
Contact Angle	θ_c	95	$^\circ$
Liquid Saturation	s	0.05	–

trends between the two methods however are in agreement, and the numerical solution quickly approaches the analytical solution outside of the jump region, suggesting that the numerical model is capable of accurately predicting a liquid saturation jump.

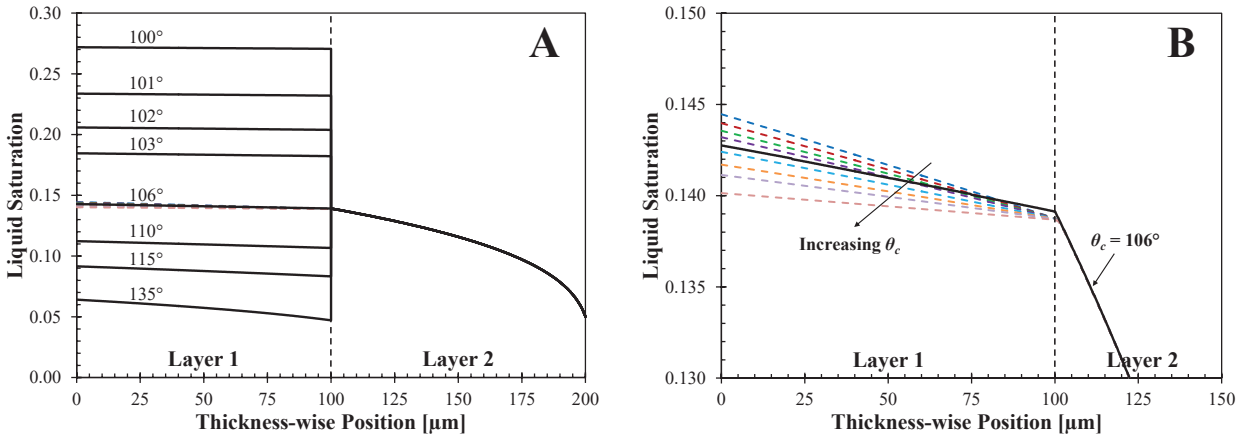

Figure 3.3: Comparison of the analytical (black line) and numerical (dashed coloured lines) MMM solutions of the saturation jump equations, for the case where $\nabla\psi = 0$ in the numerical model and Layer 1's contact angle is varied, as shown in the graphs. a) Displays the full range of the two layers, whereas b) displays the solutions within Layer 1 and near the mating layers' interface.

For comparison purposes, and to emphasize the importance of the inclusion of $\nabla\psi$, this test case was repeated with $\nabla\psi = 0$ set throughout the domain of the numerical model. To obtain stable numerical results, the distribution of ψ across the interface at $x = 100$ μm had to be artificially diffused as previously discussed. In this scenario, shown in Figure 3.3, the numerical model did not predict a liquid saturation jump and the numerical results between all values of Layer 1's θ_c were all very comparable. For example, the numerical model's liquid saturation at $x = 0$ only varied from 0.144 to 0.140, whereas the analytical solution predicts 0.272 to 0.064 for a Layer 1's θ_c of 100° and 135° respectively. Although the general decreasing trend in liquid saturation with increasing hydrophobicity is consistent between the analytical and numerical models, the magnitude of the numerical model's liquid saturation jump is shown to have a relative difference as high as 200%. Although this seems to be due to the simplification made for this test case, it should further be stated that the motion of fluid within a porous media is caused by a difference in capillary pressure, rather than a difference in liquid saturation, as given by the capillary diffusion flux, $\mathbf{j_l}$, in Table 2.1. This perspective of the driving force is another reason for the importance of including $\nabla\psi$ in this work as well as in multiphase fuel cell models.

3.2 Test Case 2 – Comparison to an Analytical Single Phase FE-DMFC Model

In this section, the numerical model is compared to the limiting case where the fuel cell is operating under single phase conditions. It is assumed that liquid only exists from the AFC-ABL to CM-CCL interfaces, whereas gas only exists from the CM-CCL to CBL-CAC interfaces. This scenario allows for an analytical solution to be formed, as derived in Appendix D, and will help to gauge if the numerical model's equations have been correctly implemented. The analytical model accounts for the convective and diffusive modes of transport in all layers, and the back pressure within the FEC. However, to ensure an analytical solution is possible, the CLs are treated as interfaces, and the thickness-wise velocity within the FEC is averaged. Due to these simplifications, there will be differences in the analytical and numerical results. As such, these models are examined for their qualitative agreement, by ensuring the predicted values for each variable are comparable, and that the predicted trends are consistent. It should be noted that this section will focus on the comparison between the analytical and numerical models, whereas the behaviour and physics within the system will be discussed in detail in Chapter 4.

To provide representative results, the analytical and numerical models are compared using the operating conditions and electrochemical properties listed in Tables B.1 and F.1 respectively, which are considered to be the 'baseline operating conditions' for this dissertation. In this scenario, it is assumed that that the anode and cathode have zero back pressure, as this allowed for better visualization of the differences between the analytical and numerical solutions. The comparison between the two models are presented in Figure 3.4 for specified current densities of 100 A m^{-2}, 500 A m^{-2} and 1500 A m^{-2}.

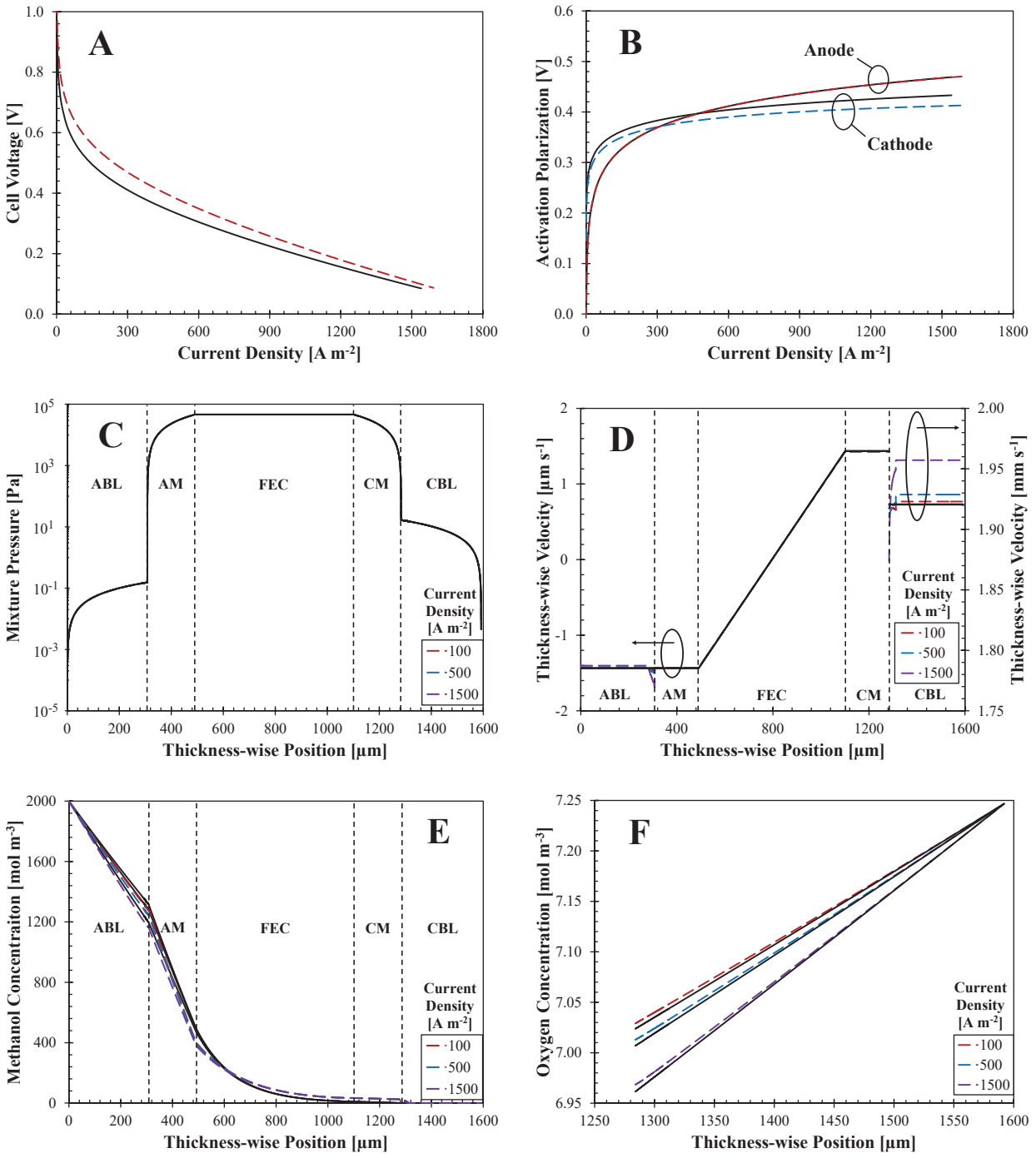

Figure 3.4: Comparison between the analytical (black solid line) and numerical (coloured dashed line) results, under bas line operating conditions and varied current densities. The following figures display the following profiles: (a) polarization curves, (b) anode and cathode activation polarization, (c) gauge pressure distributions, (d) mixture velocity distribution (note the change in units on the secondary axis), (e) methanol concentration distribution, and (f) oxygen concentration distribution.

Overall the predicted trends and values agree well between the two models. The polarization curves provide comparable performances, where the analytical model underpredicts the fuel cell's performance, as seen in Figure 3.4a. This was found to be due to the differences in the predicted ξ^{O_2} between models, causing the analytical model's cathode activation polarization curve to be higher, as seen in Figure 3.4b. For comparison, the analytical model predicted a $\xi^{O_2} = 0.065$, which corresponds closely with the value of $k_{H,e}^{O_2}$, while the numerical model predicted an average $\xi^{O_2} = 0.095$. The difference in ξ^{O_2} between the two models stem from the approximation made to ξ^{O_2} to allow for analytical solution to be obtained, as discussed in Section D.5.

The pressure and velocity distributions are also consistent between the two models, as observed in Figure 3.4c-d. There is a peak pressure within the FEC and lower pressure within the anode and cathode compartments, causing the bulk fluid to move from the FEC to the anode and cathode compartments respectively. Note that to better visualize the differences between the analytical and numerical solutions, the velocities from the AFC-ABL interface to the CM-CBL interface follow the primary y-axis, whereas the velocities within the CBL follow the secondary y-axis with a different scale. Discontinuities in the velocity profile are predicted by both models. The cause of these discontinuities will be discussed in detail in Section 4.1. However, the two models predict a consistent discontinuity at the CM-CCL interface (note the change in scale on Figure 3.4d's secondary y-axis), whereas the numerical model predicts an additional set of discontinuities near the AM and CM, which correspond to the ACL and CCL. The discontinuities in the CLs are also caused by the transport of methanol within the electrolyte phase of the CLs, as governed by Equation 2.31. The analytical model does not account for this behaviour.

The two models also predict consistent behaviour for the methanol and oxygen concentration profiles, as shown in Figures 3.4e-f; where the concentration profiles are shown to

have a decreasing trend from the respective inlet to the CLs, as well as when the current density is increased. Through examination of these results, there are slight differences in these concentration profiles, which are expected to be due to the differences in the analytical and numerical velocity fields and how the two models treat the convective terms within the system. For example, the numerical model predicts a discontinuous velocity across the BL-CL interfaces, as well as accounts for the variation in velocity within the FEC. The analytical model does not account for these effects.

From the findings in this test case, both models seem to provide consistent and comparable results in each profile. Since the differences in results seem to be caused by the assumptions built into the two models, the numerical model is deemed sufficiently accurate in determining the proper trends and behaviour of the fuel cell.

3.3 Test Case 3 – Comparison to Experimental FE-DMFC Data

In this test case, the numerical model is compared to in-house experimental FE-DMFC data and is intended to determine if the numerical model is capable of accurately reproducing the performance of an actual fuel cell. The details of the fuel cell design and experiment are provided in this section, whereas Appendix E details the uncertainty analysis.

3.3.1 Fuel Cell Assembly and Design

The design of the fuel cell used in this work is the same as the one developed by Kablou [81]. The flow field is of parallel serpentine design with seven square 1.5 mm channels with a square active area of 25 cm^2. The channels are also machined on 12.7 mm (0.50 in) thick graphite plates (AR-08) and are fastened to two 3.2 mm (0.125 in) thick copper plates with six stainless steel bolts (1/4 in - 20), each at a torque of 6.78±0.06 N m (60±0.5 lbf in).

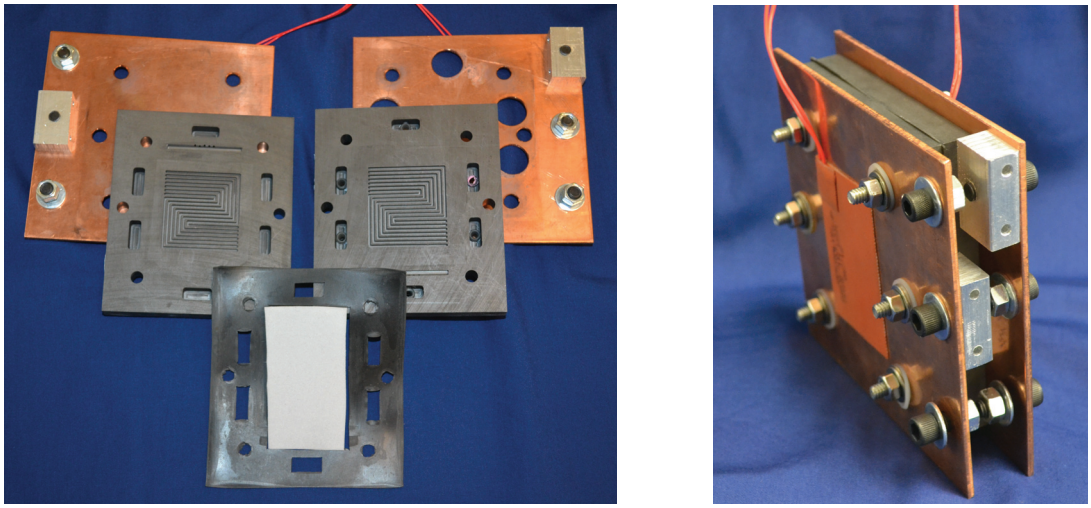

Figure 3.5: Photograph displaying the layout of the FE-DMFC components (left) as well as the fully assembled cell (right).

The bolts were electrically insulated from the fuel cell by fitting shrink wrap around each bolt, as well as utilizing nylon washers, which were placed between the current collectors and the stainless steel nut/bolt cap and washers. To seal the fuel cell, a 0.75 mm Viton® gasket was used, with space cut out to allow for a 0.61 mm porous polyethylene spacer to be inserted. This spacer is used as the flowing electrolyte channel. Figure 3.5a displays the graphite plates, flow field, current collectors, gasket and porous FEC material used in the tested fuel cell. Figure 3.5b displays the fully assembled FE-DMFC. For more details in the fabrication and assembly of the fuel cell, the reader is referred to Kablou [81]. It should be noted that during operation, methanol was supplied from the bottom of the flow field and air was supplied from the top of the flow field. This was done to allow for any produced carbon dioxide bubbles and water droplets to be easily expelled due to buoyancy.

To ensure consistent measurements from the electronic load controller, an aluminum plate was tightly fastened to each copper plate, as shown in Figure 3.5. Each aluminum plate had a 0.363 mm (5/32 in) hole drilled in to allow the load controller's voltage sensing leads to be inserted. These voltage sensing leads were soldered to male banana connectors that were friction fitted to the drilled holes in the aluminum plates. The load controller's

Table 3.2: Mass loading of each component within the ACL and CCL.

Component	Mass Loading [mg cm^{-2}]	
	ACL	CCL
Platinum	2.70	2.00
Ruthenium	1.35	0.00
Carbon	8.00	4.00
Nafion ®	8.00	4.00

current carrying leads were firmly bolted to the base of the copper plates. The continuity setting on a digital multimeter was used to test if the bolts were electrically insulated from the fuel cell. To check if the fuel cell is fully sealed, compressed air was fed through each channel (anode, flowing electrolyte and cathode), while water was passed through the other channels. This gave a visual indication of any air leakage through the gaskets or membranes. In each of the presented cases, no leakage was observed nor were any of the bolts in electrical contact with the fuel cell.

The half-MEAs used in this work were made of commercially available carbon paper (Toray® TGP-H-090), catalyst and Nafion® 117 (N117) membranes. The composition of each CL is summarized in Table 3.2. Each Nafion® membrane was hydrated by being boiled for at least an hour at 90°C in 1.28 mol dm^{-3} hydrogen peroxide and then in 0.50 mol dm^{-3} sulfuric acid. After each step, the membranes were boiled in distilled water for at least an hour. The hydrated membranes were then stored in a sealed container filled with distilled water until they were required for use. To assemble the half-MEAs, a hot press (Carver Laboratory Press, model no: 2697-5) was used, following the same method as Sabet-Sharghi [80] (180°C at 3 MPa for 3 min). During the assembly of the fuel cell, the half-MEAs were secured to the graphite plates with a sheet of 88.9 μm (0.0035 in.) thick Teflon® tape that was sufficiently wide to cover the whole face of the graphite plate. The tape was cut around the half-MEAs' active area to allow protons to be transported across. An assembled half-MEA

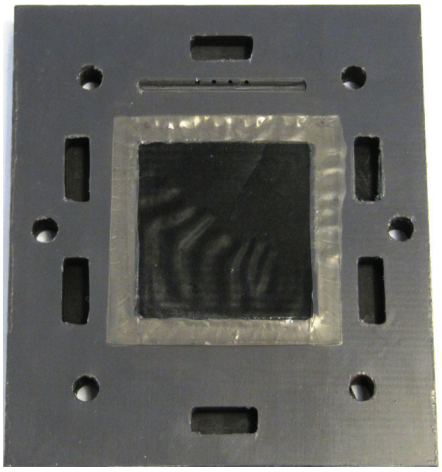

Figure 3.6: Photograph of a half-MEA fastened to the graphite plate with a sheet of Teflon tape.

that is fastened to a graphite plate is shown in Figure 3.6.

3.3.2 Experimental Setup

A photograph and schematic of the experimental setup used for all measurements, are provided in Figures 3.7 and 3.8.

In this system, diluted HPLC grade methanol is fed into the anode with a peristaltic pump (Omega Engineering Inc., MASTERFlex C/L-77122-22) and preheated with a 64 W ribbon heater (Omega Engineering Inc., HTC-030), where the temperature of the preheater is controlled with a temperature controller (Omega Engineering Inc., OMEGA CN-79000). The outlet of the anode is collected in a waste container. Diluted ACS grade sulfuric acid is fed into the inlet of the FEC via peristaltic pump (Fluid Metering Inc., RHB-PM6013) and the sulfuric acid and crossed over methanol are collected at the outlet, in a waste container. The same process is utilized for the oxygen, where pressurized air (at 120±10 kPa) is fed to the system via a compressed air line, and the flow rate is maintained using a flow meter (Gilmont, GF-9360). The outlet of the cathode is allowed to flow to atmosphere. The fuel cell is also heated using a heating pad (Omega Engineering Inc., SRFG-203/10-P) on each

Figure 3.7: Photograph of the experimental setup used in this study.

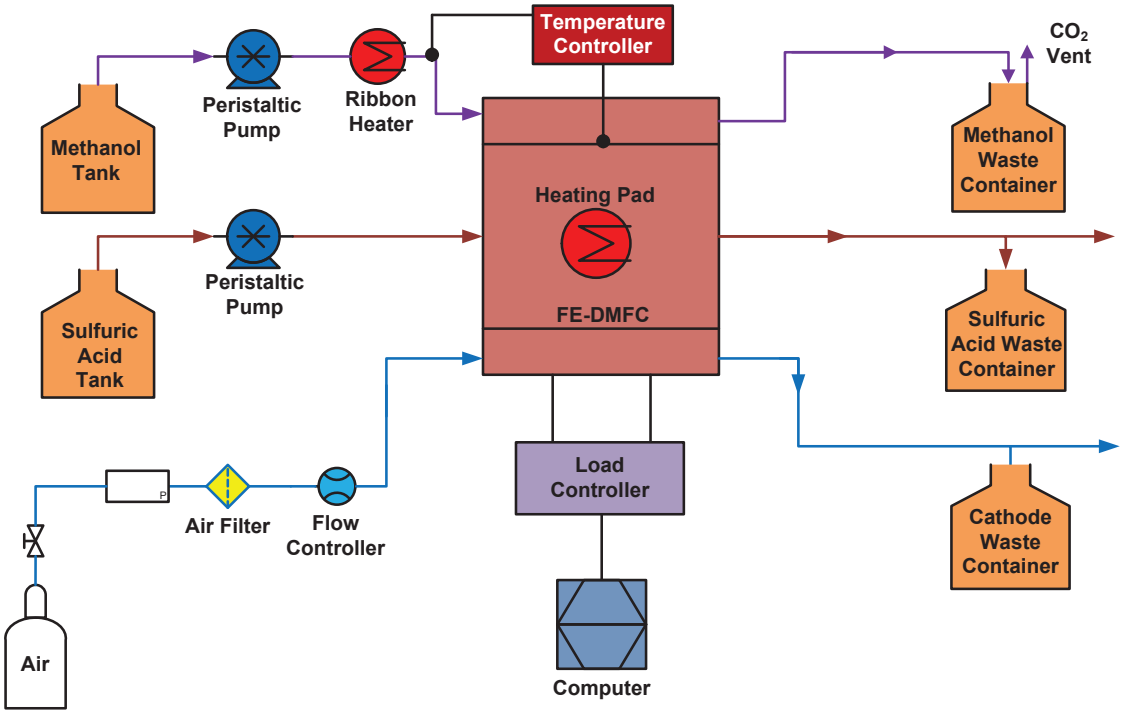

Figure 3.8: Schematic of the experimental setup used for the operating fuel cell measurements.

Table 3.3: Baseline operating conditions for the experiments with estimated bias errors.

Operating Condition	Set Point	Units
Cell Temperature	80 ± 2.3	°C
Anode		
Methanol Inlet Concentration	2000 ± 6	mol m^{-3}
Methanol Inlet Flow Rate	10 ± 0.5	cm^3 min^{-1}
Flowing Electrolyte Channel		
Sulfuric Acid Inlet Concentration	650 ± 4	mol m^{-3}
Sulfuric Acid Inlet Flow Rate	10 ± 0.5	cm^3 min^{-1}
Cathode		
Cathode Inlet Pressure	120 ± 10	kPa
Air Inlet Flow Rate	500 ± 64	cm^3 min^{-1}

side of the fuel cell, each rated at 1.55 W cm^{-2} (10 W in^{-2}), and are controlled using the same temperature controller as previously mentioned. The temperature observed by the controller was measured using a K-type thermocouple (J-KEM Scientific Inc., TWT-K), and the signal is sent to the same temperature controller as previously mentioned. Table 3.3 lists the baseline operating conditions for the fuel cell tests.

Fuel Cell Activation Procedure

To ensure that the membranes are well hydrated and the half-MEAs are 'broken in' prior to testing, the procedure summarized below is applied [15].

- First, distilled water is supplied to the anode and flowing electrolyte channels for several hours and is then allowed to sit within these channels overnight.
- Diluted methanol, sulfuric acid and air are then supplied to the anode, FEC and cathode, respectively, at the baseline operating conditions shown in Table 3.3.
- Once the open circuit voltage (OCV) has stabilized, the fuel cell is set to provide 300 mV for a minimum of 15 min. Afterward, the fuel cell is switched to OCV for a

minimum of 15 min.

- The process is repeated until the voltage and current have stabilized between both operating conditions.

Polarization Data Acquisition

In this work, the presented polarization curves were measured potentiodynamically, from 100 mV to 900 mV at a rate of 2 mV s^{-1} with a Fideris Innovator Series (250 W) electronic load controller. To ensure accurate and repeatable measurements, the experiments were conducted three times, each on a separate day. On each repetition, five polarization curves were collected, and this procedure was applied to three MEAs of the same construction. The average of all 45 polarization curves were taken to produce the experimental results presented in this work. An in-house post-processing program was used to average all sets of polarization curves and to perform the uncertainty and statistical analysis on them. The process applied in this program is discussed in Appendix E. For reference, the lowest, average and highest uncertainties in these measurements are summarized in Table 3.4. In general, the uncertainty in the current density was greater at lower cell voltages (increasing current density), whereas the opposite trend was observed for the cell voltage.

Table 3.4: Summary of the lowest, average and highest uncertainties for the experimental measurements presented in Test Case 3. Details of these uncertainties can be found in Appendix E.

	Current Density [A m^{-2}]	**Cell Voltage [mV]**
Lowest	±87	±18
Average	±125	±60
Highest	±280	±150

3.3.3 Comparison between Experimental and Simulated Results

The numerical model's predictions are compared to polarization curves at three different cell temperatures (40°C, 60°C and 80°C) and three different inlet methanol concentrations (1000 mol m^{-3}, 2000 mol m^{-3} and 4000 mol m^{-3}). For clarity, the error bars are not presented in the figures presented in this test case. However, these same measurements with the error bars are presented in Figures E.2 and E.3, for reference. Furthermore, Appendix F details the approach used to calibrate the numerical model to the experimental data. The calibrated parameters are summarized in Table F.1.

The comparison between the modeled and experimental polarization curves are shown in Figure 3.9a and b, for the case of varied cell temperature and inlet methanol concentration, respectively. The parity plots for each data set are shown in Figure 3.10, where each axis is normalized by the highest current density for each operating condition. As can be seen in Figures 3.9a and 3.10a, the calibrated model captures the temperature dependency very well, with an average deviation of 3%. The greatest deviation was found to be with the varied inlet methanol concentration, shown in Figures 3.9b and 3.10b, with an average deviation of 4.7%. The experimental data suggests that with increasing methanol concentrations, the activation polarization also increases, likely due to increased methanol crossover. This can be seen by the lower cell voltages at a current density of 200 A m^{-2} in Figure 3.9b. Although the model displays the same trend, the amount of methanol crossover predicted by the model is found to be very small, due to the strong FEC sink; where the maximum modeled crossover current density was predicted to be 37.8 A m^{-2}, 75.6 A m^{-2} and 150.8 A m^{-2} for the 1000 mol m^{-3}, 2000 mol m^{-3} and 4000 mol m^{-3} cases respectively; all of which occurred at open circuit voltage (OCV). This discrepancy suggests that there could be other dominant driving forces that are not accounted for and need to be included. However, the model does show the correct general trend of the polarization curve in all cases and the model's predictions are well within the uncertainties of the experimental data summarized in Table 3.4.

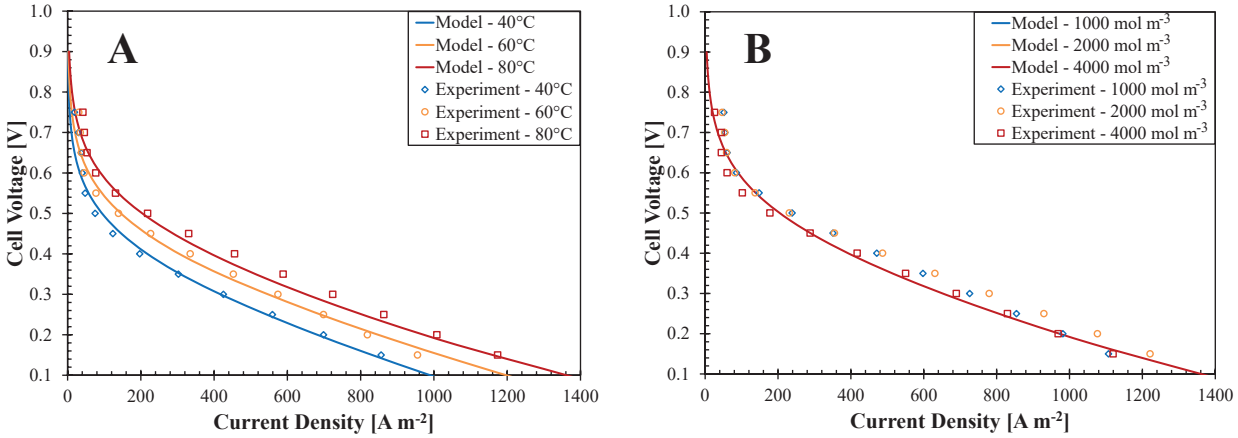

Figure 3.9: Comparison between the experimental (data points) and numerical (solid lines) results, for: (a) varied cell temperature, and (b) varied inlet methanol concentration.

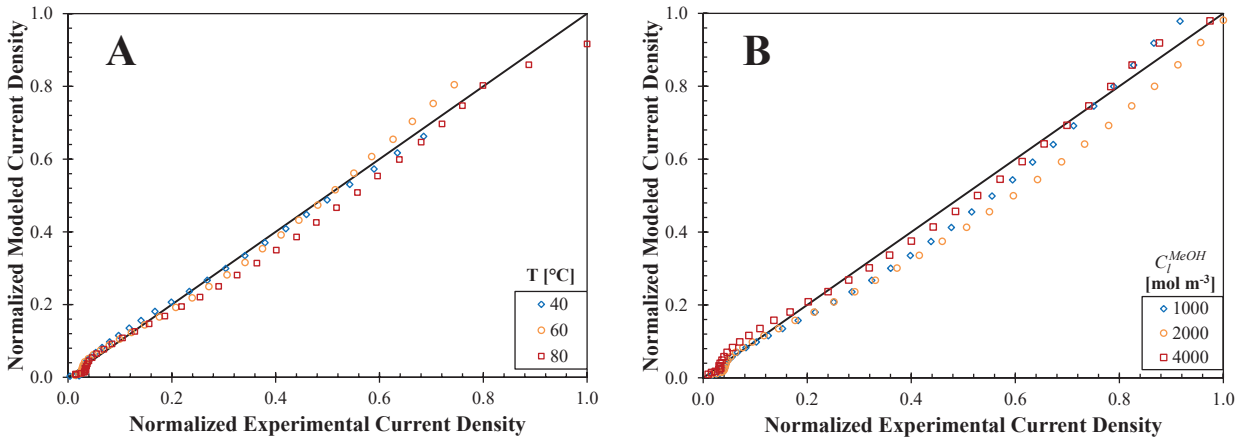

Figure 3.10: Normalized parity plot (i/i_{max}) showing all experimental data points for the (a) varied cell temperature experiments, and (b) varied inlet methanol concentration experiments.

Chapter 4

Modeling Case Studies

In this chapter, the general behaviour of the FE-DMFC, and a series of parametric studies are performed to help lay the foundation to describe the physics and performance of the FE-DMFC. A focus is placed on understanding the role in which the porous properties and geometry of the FEC, and the geometry of the two membranes play on the fuel cell's performance. These studies begin with the variation of various operating conditions, and then the optimization of each layer within the fuel cell.

4.1 Baseline Performance Characteristics

To understand the underlying physics of this fuel cell, the characteristics of each of the major variables (P, u, C_l^{MeOH}, $C_g^{O_2}$, s and λ_{wc}) are discussed under the baseline operating conditions, which can be found in Table B.1.

4.1.1 Pressure and Velocity Distributions

Beginning with the mixture gauge pressure, P, shown in Figure 4.1a, it can be seen that there is a slight increase in pressure across the anode, while there is a slight decrease in pressure across the cathode ($\Delta P \sim +1$ Pa and -60 Pa, respectively). This causes the mixture velocity, u, shown in Figure 4.1b, to be on average –3 μm s^{-1} within the anode,

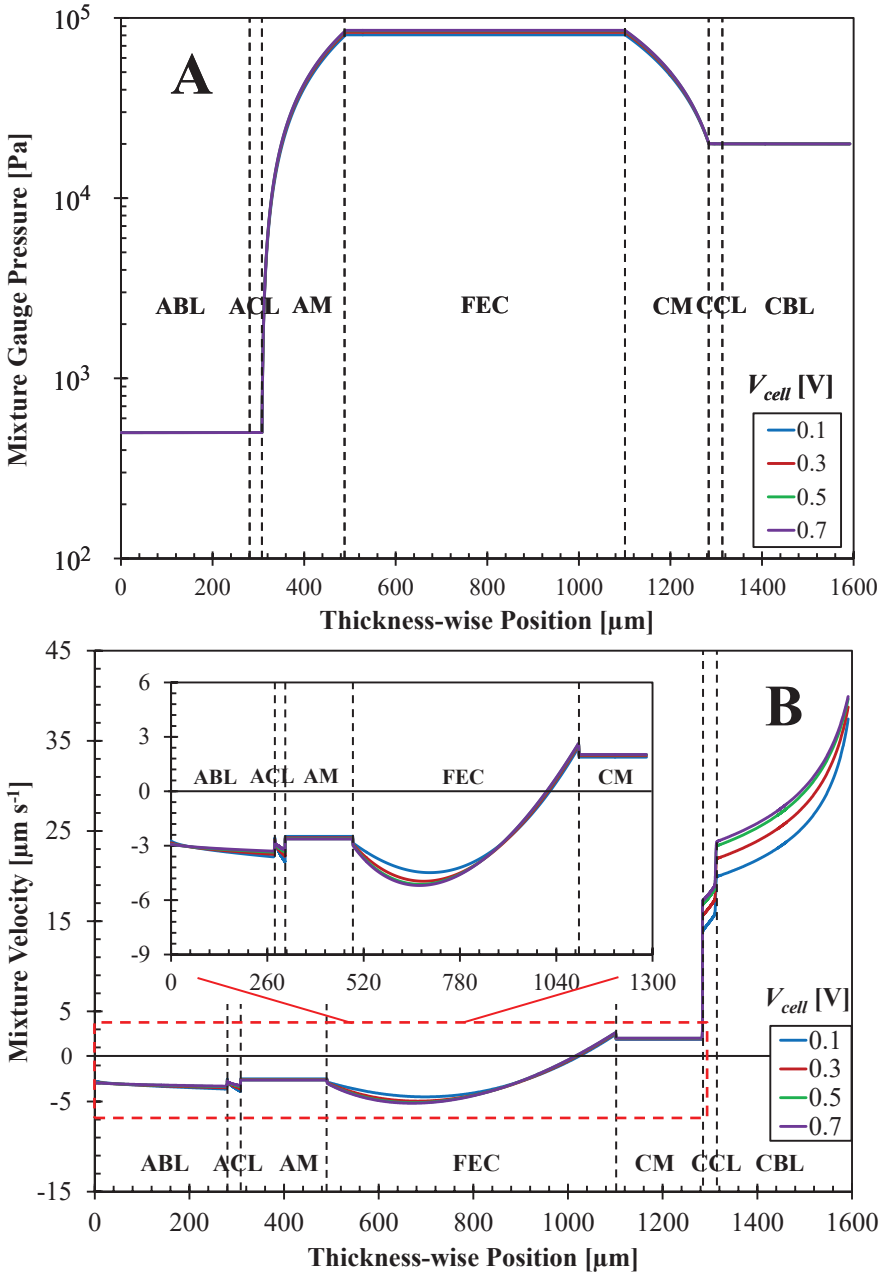

Figure 4.1: Modeled effect of current density on (a) mixture gauge pressure, and (b) mixture velocity, both under the baseline conditions.

and +24 μm s^{-1} within the cathode. Note that a negative u signifies flow towards the AFC, whereas a positive u is towards the CAC. As can be seen in this figure, the mixture velocity displays discontinuities across the interfaces adjacent to the CLs. This is due to two reasons. The first is that within the CLs, an electrolyte phase is present, where methanol and water can be absorbed. The transport of methanol and water within the

electrolyte phases are not directly accounted for within the mixture phase; therefore, a source term (Equation 2.29) was required to ensure that all mass and species are conserved. This source term subtracts from the mixture velocity, and thus causes the discontinuity in the mixture velocity within the CLs. The second reason is due to the very rapid changes in liquid saturation across the interfaces adjacent to the CLs. Since the pores of the membranes are hydrophilic, the liquid saturation within the membranes can be assumed to good approximation, equal to one [73]. In the presented numerical cases, the liquid saturation is less than one within the porous layers. This causes large changes in the mixture kinematic viscosity and mixture density, which in turn cause jumps in the mixture velocity to ensure continuity. The mixture density and kinematic viscosity are shown in Figure 4.2 for reference. In this work the mixture pressure is assumed to be continuous across all layers.

Across the membranes, there is a large pressure difference ($\Delta P \sim 65$ kPa) relative to other pressure differentials in the fuel cell, which is caused by the water that is introduced into the fuel cell from the FEC. Because the membranes have a low permeability, they act as a barrier requiring a high pressure for water to be transported out of the FEC and towards the anode and cathode, which are both at lower pressure. Physically, this high pressure would also be due to the back pressure required to sustain the flow of sulfuric acid through the FEC. The bulk flow of water from the FEC causes an inflection point in the magnitude of u in the FEC (at $\sim$1023 μm), where u transitions from a negative to positive value. Within the CBL, u also increases in magnitude due to the decrease in mixture dynamic viscosity ($\mu = \rho\nu$), caused by the decreasing trend in liquid saturation from the CCL to the CAC. Since the gaseous state has a lower dynamic viscosity than the liquid state, the mixture must increase in velocity to conserve mass.

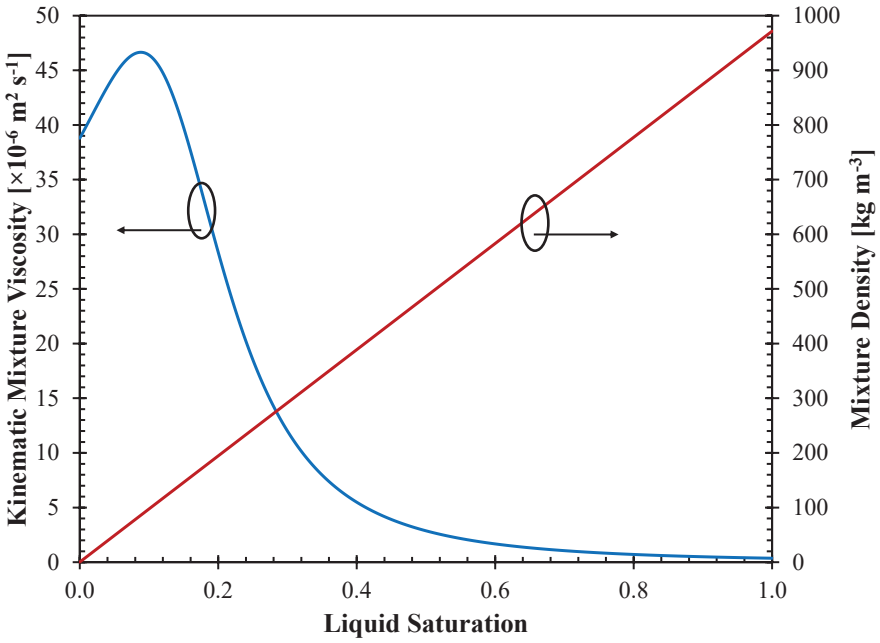

Figure 4.2: Variation of mixture kinematic viscosity, ν, and mixture density, ρ, with respect to liquid saturation at a temperature of 80°C.

4.1.2 Liquid Saturation and Water Content Distributions

The liquid saturation and water content profiles are shown in Figure 4.3. Note that the liquid saturation applies to the porous regions (ABL, ACL, FEC, CCL and CBL) as given by the left y-axis, whereas the water content applies to the electrolyte layers (ACL, AM, FEC, CM and CCL) as given by the right y-axis. It can be seen that the liquid saturation follows a decreasing trend in the anode as the current density is increased, due to the generation of CO_2 by the MOR in the ACL. In the cathode, the liquid saturation increases with increased current density, due to the increased production of water by the ORR. The liquid saturation profile within the FEC is nearly uniform in comparison, due to the lack of chemical reactions within the layer, the introduction of water at the FEC inlet, and due to the electro-osmotic drag (EOD) of water through this layer.

Across the BL-CL interfaces, there is a liquid saturation jump which is caused by the differences in porous properties. In both CLs, there is a higher liquid saturation than in the

BLs, because the CLs used in this study are more hydrophilic than their adjacent BLs. It is also observed that a liquid saturation jump does not occur at the CL-membrane interface since the Young-Laplace diffusion coefficient (Equation 2.11) is equal to zero within the membranes, due to the membranes' purely liquid saturated state ($s = 1$). Although this seems to contradict what is presented in Figure 4.3, it should be remembered that the liquid saturation distribution presented within the membranes are fictitious as they are only used to calculate the water content. As such, the true liquid saturation within the membranes are assumed to be equal to one.

In the AM, the water content becomes more uniform with increased current density, which is due to the increasing dominance of the electro-osmotic drag (EOD), as shown in Figure 4.4a. The greater uniformity of the AM's water content reduces the concentration gradient and decreases the diffusive flux. Furthermore, since u is negative in the AM, this causes a strong counterflow, which reduces the overall water crossover flux through the AM. At low current densities, the back-flow of water is the most dominant driving force, which causes the net flow of water through the AM to flow towards the anode. However, as the EOD becomes more dominant at higher current densities, the flow of water transitions to a flow towards the FEC. This finding demonstrates the importance of the convective flow which is sometimes neglected in DMFC modeling literature, as well as the importance of accounting for the back-pressure associated with the flow of the flowing electrolyte, which has been neglected in previous FE-DMFC models.

Through the CM, the increasing rate of water transport through the anode as well as the water introduced by the FEC causes a net increasing rate of water entering the cathode, as shown in Figure 4.4b. Since all the driving forces act in the same direction, there is no counterflow. Furthermore, since the water content at the FEC-CM interface increases with current density due to the increasing dominance of EOD, this causes a strong concentration

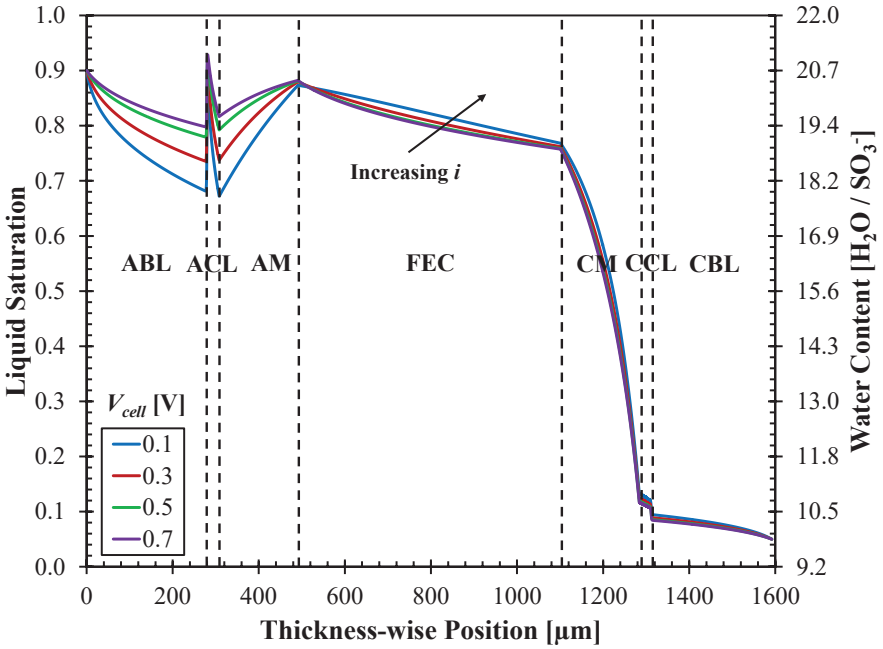

Figure 4.3: Modeled effect of current density on the liquid saturation and water content distributions, under the baseline operating conditions.

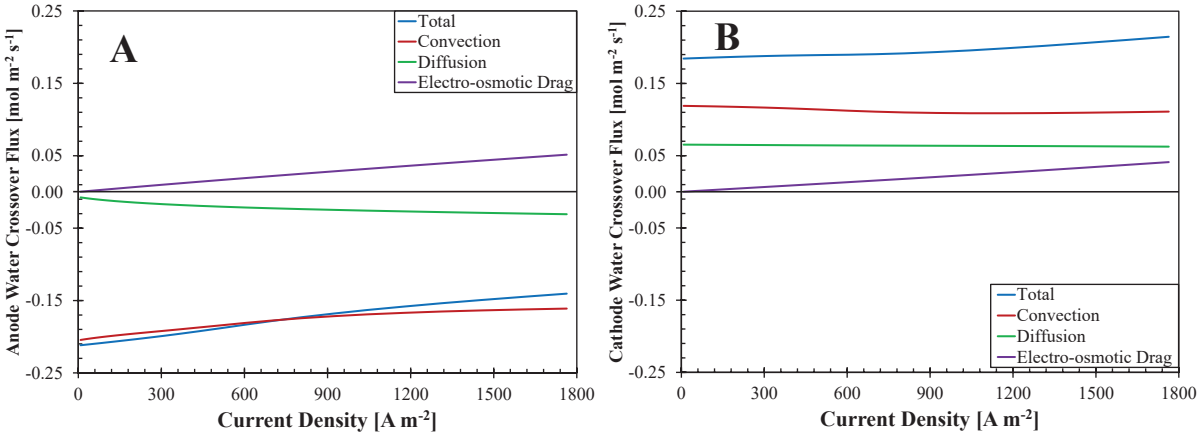

Figure 4.4: Modeled effect of current density on (a) the molar flux of water and its components through the AM, and (b) molar flux of water and its components through the CM, all under the baseline operating conditions.

gradient across the CM, which causes 74% of the crossed over water to be driven by diffusion at open circuit voltage (OCV). This proportion drops to 58% at 1460 A m^{-2}, where the other modes of transport each account for 21% of the total flux. The increasing dominance of the convective flow is largely due to the increased hydration of the membranes, allowing more water to crossover. The increased hydration of the membranes also cause the ionic

resistance of the membranes to decrease. However, due to the second membrane and the FEC, the ohmic resistance is still high. At 1460 A m^{-2}, the ohmic polarization was estimated to be 0.27 V, accounting for 25% of the total losses. The anode and cathode activation polarizations are estimated to account for the remaining 41% and 34%, respectively. Overall, these observations and trends are consistent with the ones discussed in DMFC modeling literature [55, 75].

4.1.3 Liquid Methanol Concentration Distribution

The liquid methanol concentration profile, C_l^{MeOH}, shown in Figure 4.5a, indicates a decreasing trend with increasing current density, primarily due to the increased rate of the MOR within the ACL. Within the FEC, methanol is effectively removed from the fuel cell, with only 2% of the total methanol crossover from the anode reaching the cathode. This low rate of methanol crossover is indicated by the low concentrations within the FEC, CM and CCL, (shown in Figure 4.5's sub-figures) and the large difference in crossover current density through the AM and CM given by Figures 4.6a-b. The model suggests that the crossover current density within the CCL was as high as 73 A m^{-2}, where for comparison, the rate of methanol crossover for a DMFC, with similar operating conditions, is typically on the order of 1400 A m^{-2} [19, 131]; a 20-fold reduction in methanol crossover. Due to the low C_l^{MeOH} in the CM of the FE-DMFC, the convective and EOD components of the crossover current density become very small, cumulatively accounting for 2% of the total crossover. This suggests that these components could be neglected from the calculation of the parasitic current, if the flux is calculated purely based on the incoming flux to the CCL ($i_{xover} = 6F\ \dot{N}''^{MeOH}\Big|_{CM-CCL}$).

When comparing the presented methanol concentration profile, in Figure 4.6a, to those in DMFC literature, it is found that the FE-DMFC's concentration profile is much lower for the same current density and comparable operating conditions. Although this will be

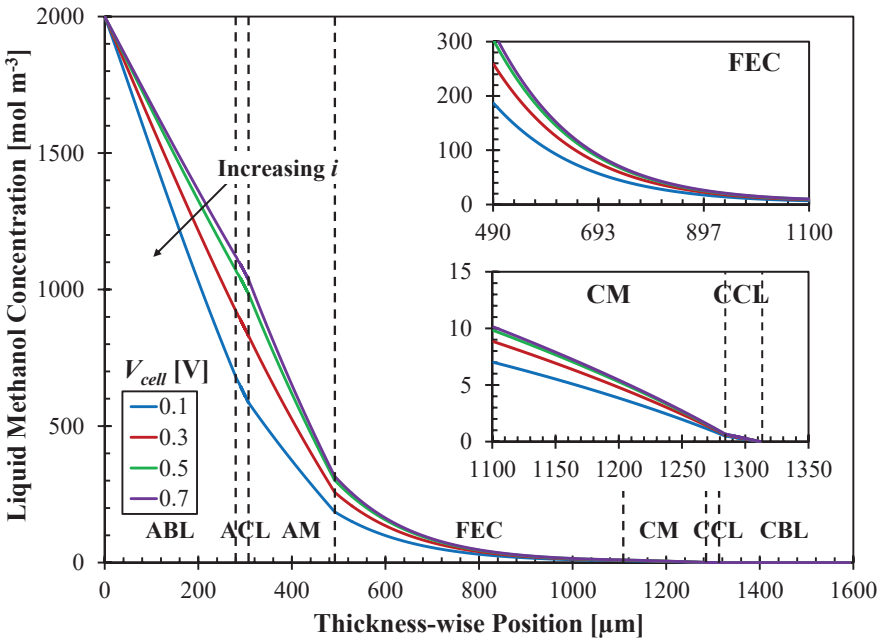

Figure 4.5: Modeled effect of current density on (a) the liquid methanol concentration, and (b) the distribution of methanol crossover and its components, through the CM under baseline operating conditions.

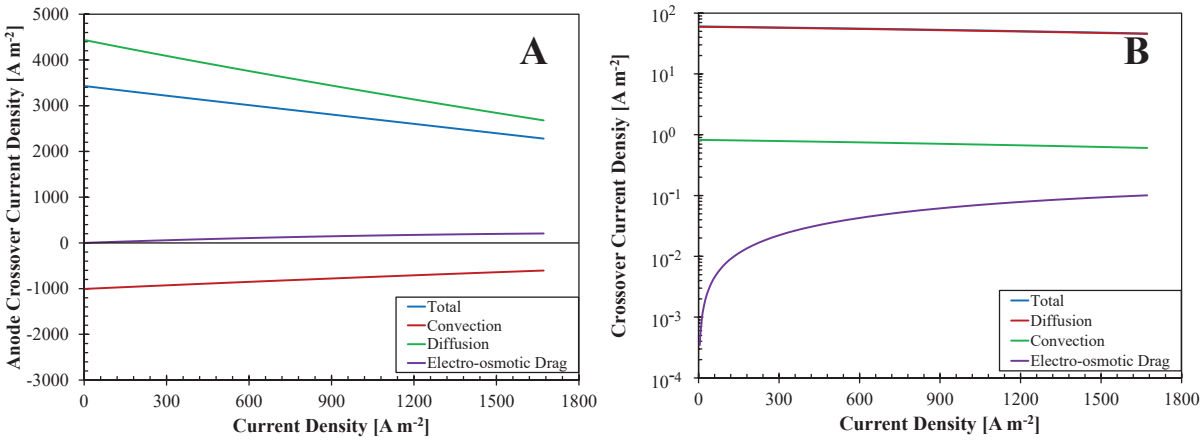

Figure 4.6: Modeled effect of current density on the methanol crossover current density through (a) the anode membrane, and (b) cathode membrane, under baseline operating conditions. Note that for legibility, both figures' y-axes have different scales.

discussed in more detail in Section 4.5, the primary reason for this discrepancy is due to the strong counterflow imposed by the FEC, which accounts for 25% of the total methanol flux through the AM, as shown in Figure 4.6a. This counterflow is double sided. On one hand the counterflow aids in reducing methanol crossover, as previously noted. However, this counterflow also reduces the methanol concentration within the ACL, thereby increasing the

anode's activation and concentration polarizations and thus reducing fuel cell's performance. The latter point is also valid for the cathode, as the counterflow also hinders the oxygen transport. However, this counterflow does not seem to affect the incoming oxygen to the same degree, as it does for methanol, likely due to oxygen's greater mobility within the cathode. As such, to reduce these side effects, this fuel cell could benefit from a FEC that has a higher porosity or permeability, thereby reducing the back-pressure within the FEC.

It should also be noted that in the investigated configuration, the liquid electrolyte is flown through the FEC once and the removed methanol is not recycled. This configuration severely impacts the fuel cell's fuel efficiency, η_{fuel}, given by Equation 4.1, and would seem to be impractical for commercial applications. Within Equation 4.1, $\bar{\mathbf{i}}_{\mathbf{a}}$ and $\bar{\mathbf{i}}_{\mathbf{xover}}$ represent the amount of oxidized methanol within the ACL and CCL, respectively, whereas $\bar{\mathbf{i}}_{\mathbf{FEC}}$ represents the amount of methanol removed by the FEC in the form of a current density, determined from Faraday's Law. Each of these terms are averaged in the thickness-wise direction.

$$\eta_{fuel} = \frac{\bar{\mathbf{i}}_{\mathbf{a}}}{\bar{\mathbf{i}}_{\mathbf{a}} + \bar{\mathbf{i}}_{\mathbf{FEC}} + \bar{\mathbf{i}}_{\mathbf{xover}}} \tag{4.1}$$

Under the base line operating conditions, η_{fuel} increased with increasing current density, as shown in Figure 4.7. This was found to be due to the decreasing amount of methanol crossover with increasing current density, as discussed earlier and shown graphically in Figure 4.6, and due to the increasing fuel utilization within the anode, making $\bar{\mathbf{i}}_{\mathbf{a}}$ more dominant. The maximum η_{fuel} was found to be 44% at a current density of 1360 A m^{-2} and cell voltage of 0.1 V. This low η_{fuel} is caused by the large amount of fuel that is removed by the FEC and is not reused ($\bar{\mathbf{i}}_{\mathbf{FEC}}$ averaging at $\sim$ 3200 A m^{-2}). This fuel wastage is similar in principle to the methanol that crosses over and is oxidized within the CCL. However, this removed methanol could in fact be recycle if it were separated from the liquid electrolyte. This could be achieved through a distillation, electrochemical or membrane separation process, as discussed in Kordesch *et al.* [5], or through novel fuel cell designs such as the one proposed

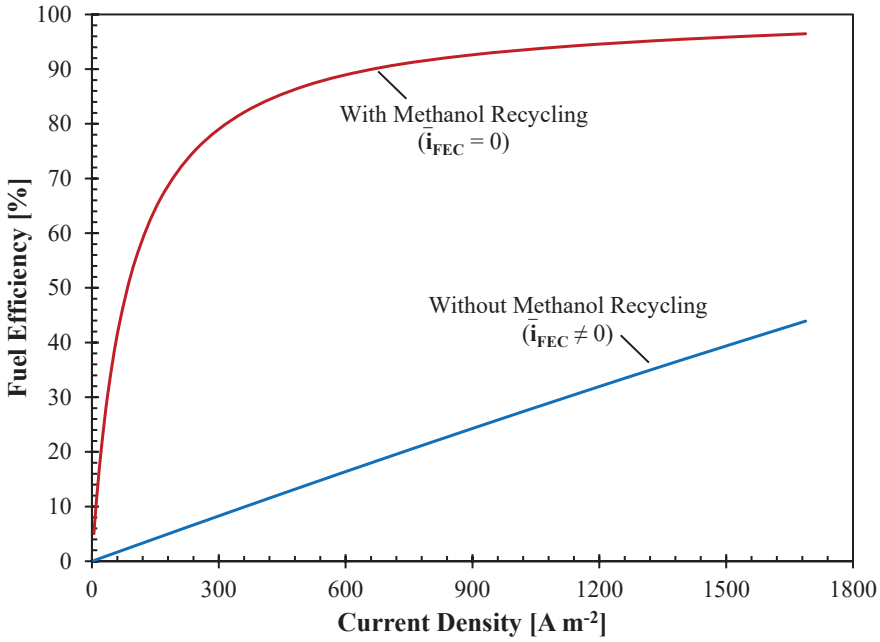

Figure 4.7: Modeled comparison of the fuel efficiency, when the removed methanol at the FEC outlet is and is not recycled to the anode inlet.

in Ouellette *et al.* [9], where the liquid electrolyte was chosen to be an intermediate of the MOR. This was done so that the FEC outlet could be routed directly to the anode inlet. If all the removed methanol were to be recycled (making $\bar{\mathbf{i}}_{\mathbf{FEC}} = 0$), η_{fuel} was found to increase substantially to a maximum of 98%. This would suggest that a configuration that recycles the removed methanol would be a more viable option for commercial applications.

4.1.4 Gaseous Oxygen Concentration Distribution

The gaseous concentration of oxygen, $C_g^{O_2}$, profile is shown in Figure 4.8. It can be seen that the $C_g^{O_2}$ decreases with current density due to the increased rate of the ORR. The rate of decrease in $C_g^{O_2}$ is less than that of the methanol concentration profile, which is largely due to the much larger molecular diffusivity of oxygen ($D_g^{O_2}/D_l^{MeOH} \sim 5000$) and very small rate of methanol crossover, as discussed previously. This suggests that the mass transfer resistance of oxygen is rather small, which is in agreement with DMFC models [18, 54].

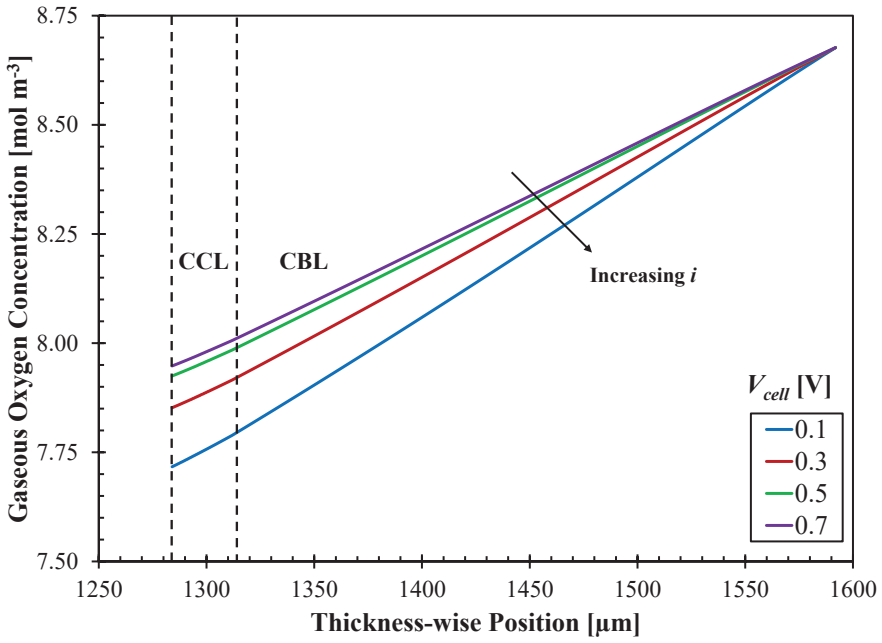

Figure 4.8: Modeled effect of current density on the gaseous concentration of oxygen.

4.1.5 Cathode Catalyst Layer Performance

As discussed in Section 2.5, the CCL utilizes an agglomerate model to account for the effects of its porous structure and composition on the ORR. The derivation presented in Section 2.5 led to an expression for the agglomerate correction factor, ξ^{O_2}. It was found that ξ^{O_2} had an average value of 0.09, which is indicative of the solubility of the oxygen in water. The model also suggested that ξ^{O_2} decreased when the current density was increased and when approaching the CM-CCL interface as shown in Figure 4.9a. This behaviour was found to follow that of the agglomerate effectiveness factor, E, shown in Figure 4.9b, since the n_{agg} was approximately 2 orders of magnitude larger than the remaining terms in the denominator. This allowed for the following approximation to be made, $\xi^{O_2} \approx Ek^{O_2}_{H,l}$. It was found that this approximation was valid as long as agglomerate radius was less than 500 nm, to achieve less than 5% error, relative to Equation 2.38. When the agglomerate radius becomes larger than this threshold, the mass transport resistance within the water and electrolyte films, and within the agglomerate nucleus become more significant due to their larger relative size. For comparison, a 0.2% error was found for an agglomerate radius

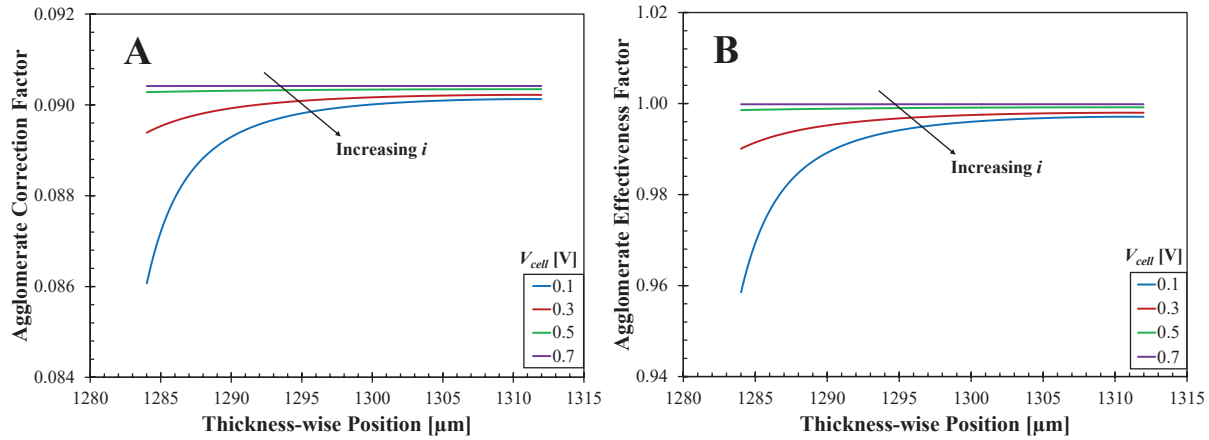

Figure 4.9: Modeled effect of current density on the CCL's (a) agglomerate correction factor and (b) agglomerate effectiveness factor.

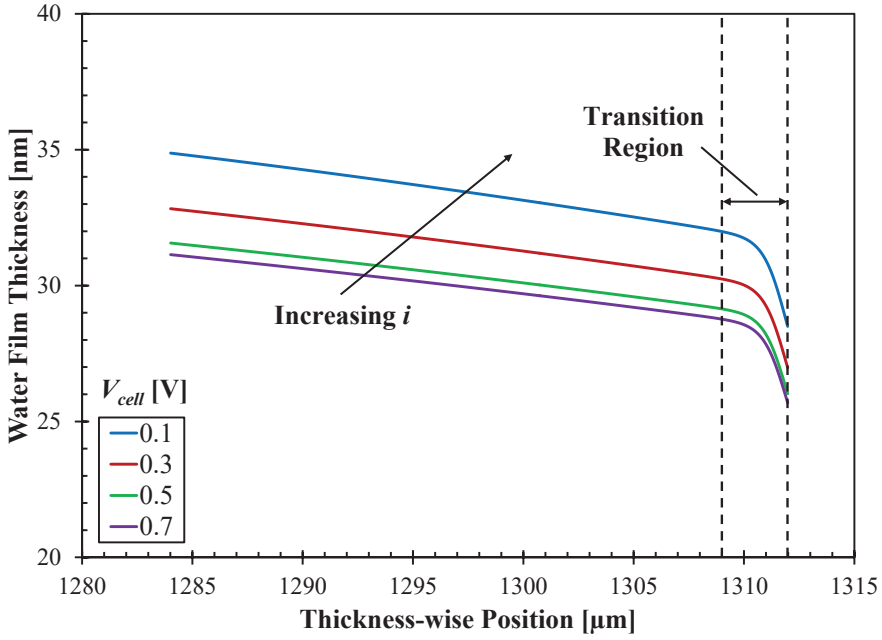

Figure 4.10: Modeled effect of current density on the water film thickness surrounding the CCL agglomerates.

of 100 nm, whereas 20% error was found for an agglomerate radius of 1000 nm.

The water film surrounding the agglomerate was found to have an average thickness of 32 nm, which increased with current density, as shown in Figure 4.10. In the range of 1309 - 1312 μm, it can be seen that the water film thickness rapidly increases. This rapid increase is caused by the liquid saturation jump which was introduced in Figure 4.4. Since this

jump and the water film thickness both follow the diffused ψ profile, the observed 'transition region' is in some sense a numerical artifact. However, it is conjectured that there could be some physical significance to this behaviour, as mating layers will likely form a transition region with some intermediate porous properties (as was discussed in Section 2.7.1), creating the observed rapid increase in water film thickness.

4.2 Effect of FEC Thickness

A method to reduce the amount of methanol reaching the CCL is to increase the FEC's thickness, t_{FEC}. Therefore to understand what other roles t_{FEC} plays on the fuel cell's performance, this section, examines t_{FEC} in the range of 0.5 - 2 mm, while all other conditions remained constant. Smaller thicknesses were not examined as the Reynolds number within the FEC would exceed the range of applicability for Darcy's Law. The simulation results suggest the fuel cell performance increased with decreasing FEC thickness, which is primarily attributed to lower Ohmic resistance. Due to the dominant resistance of the FEC, the average cell resistance increased linearly with increasing t_{FEC}. A method to counteract this could be to increase the concentration of sulfuric acid. For example, the model suggests that by increasing the sulfuric acid concentration from 0.65 mol dm^{-3} to 4.5 mol dm^{-3} would increase the power density by 15%; from 210 W m^{-2} to 240 W m^{-2}. Although it should be noted that this increase could lead to other challenges regarding the containment and durability of the fuel cell.

The numerical model also suggests that increased FEC thicknesses also cause the methanol and water crossover (both anode and cathode) fluxes to also decrease, as shown in Figure 4.11. This was found to be due to the decreasing back-pressure within the FEC. For example, the 0.5 mm channel provided a maximum back-pressure of nearly 95 kPa, whereas the 2 mm channel provided a back-pressure of nearly 20 kPa; following a nearly

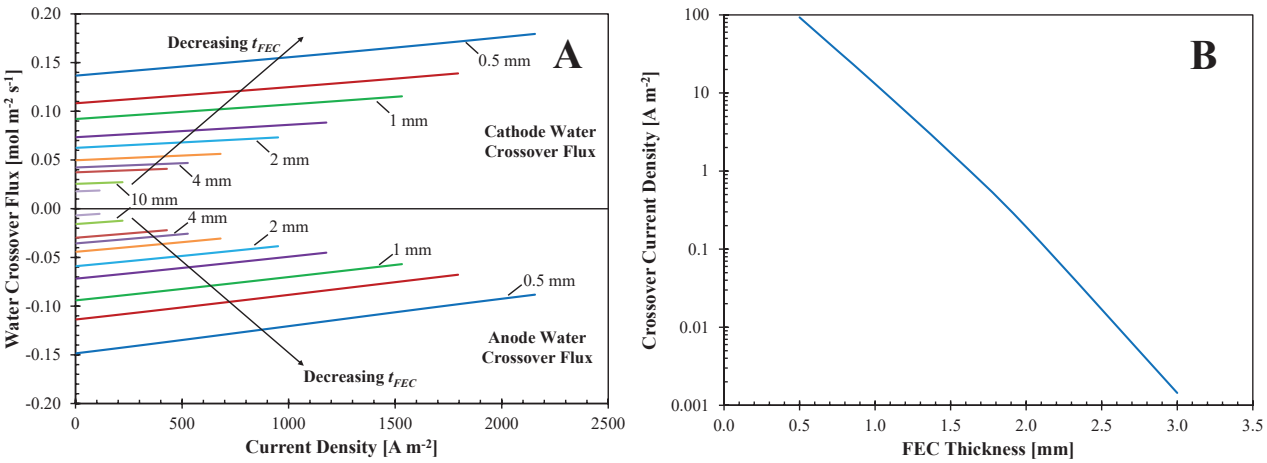

Figure 4.11: Modeled effect of the FEC's thickness on (a) water crossover flux, and (b) crossover current density. Crossover current densities calculated for $t_{FEC} > 3$ mm were not shown, as they were deemed negligible.

inverse proportionality, as would be expected from Darcy's Law. The deviations from this proportionality are due to the non-uniformities in the mixture density and mixture kinematic viscosity between tested cases. Beyond a t_{FEC} of 1 mm, the maximum crossover current density is predicted to be below 10 A m^{-2}, which could be thought of effectively zero crossover; where for comparison, at 0.5 mm, the crossover current density was 95 A m^{-2}. Due to the sensitivity of the fuel cell's performance on the FEC's thickness, the results seem to suggest that a thin FEC should be used, such as approximately 0.5 mm. Although consideration should be given to ensure that the back-pressure within the FEC does not degrade the FEC material. Furthermore, at lower thicknesses, below ∼0.3 mm, consideration should be given to account for the non-uniform velocity profile within the FEC [82].

4.3 Effect of FEC Porosity

The FEC's porosity, ε_{FEC}, is strongly linked with all diffusion coefficients by the Bruggeman correlation, as shown in Table 2.1, as well as to the capillary pressure and FEC's conductivity. This makes ε_{FEC} an important factor to examine to understand the mass transport within the fuel cell. In this section, ε_{FEC} is varied from 0.3 – 0.8, while all other

parameters are held constant. Physically, this could be achieved by modifying the pore diameter as needed [110].

As ε_{FEC} is increased, the model suggested that the effective conductivity of the FEC also increased, as described by the Bruggeman correlation. This allowed for greater current and power densities to be achieved. For example, the maximum current density ranged from 1000 to 1700 A m^{-2} for a ε_{FEC} of 0.3 and 0.8 respectively, and the maximum power density ranged from 170 to 225 W m^{-2}, for a ε_{FEC} of 0.3 and 0.8 respectively. The model suggested that the change in the FEC's conductivity had the greatest impact on the fuel cell's performance. The variation in the fuel cell's resistance and maximum power density are shown in Figure 4.12a. Extrapolating the trend shown in Figure 4.12 would suggest that a completely open FEC should be used to minimize ohmic losses. However, it was experimentally demonstrated by Sabet-Sharghi *et al.*, that with the current FE-DMFC design, an open FEC would in fact decrease the performance of the fuel cell [15]. This is due to the anode and cathode half-MEAs collapsing into the FEC, restricting the flow within the FEC, and thus decreasing the FEC's effectiveness. If more rigid BLs and CLs were used in the half-MEA architectures, and a robust method to control the back-pressure within the FEC, an open FEC and membraneless FE-DMFC could be possible. In this case, however, special care regarding the wettability of the anode and cathode materials will be needed, to prevent seepage of the electrolyte into the anode and cathode compartments.

Since higher current densities were achievable at higher ε_{FEC}, the model suggested that the EOD components of the methanol and water crossover fluxes also became more dominant at higher ε_{FEC}. The water crossover fluxes however, both for the anode and cathode, did not deviate significantly ($< 2\%$) from their trends between each tested ε_{FEC}. Although greater water crossover rates were found due to higher achievable current densities. The methanol crossover flux on the other hand showed much greater variation with ε_{FEC}, where

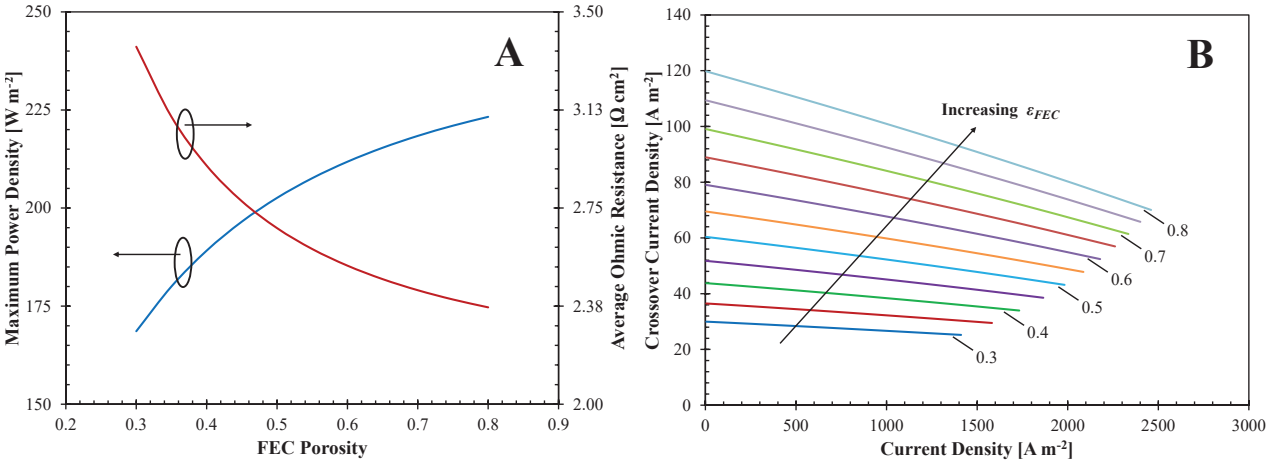

Figure 4.12: Modeled effect of the FEC's porosity on (a) the average area specific resistance and maximum power density of the fuel cell, and (b) the crossover current density.

for example, the methanol crossover flux ranged from a maximum of 30 A m^{-2} to a maximum of 120 A m^{-2}, both at OCV. It was determined that a higher ε_{FEC} would lower methanol's mass transport resistance within the FEC, thereby allowing more methanol to be transported towards the cathode. Although in the current fuel cell design, this flux is sufficiently low that it negligibly affects the fuel cell's performance.

4.4 Effect of Anode and Cathode Membrane Thickness

Since the FE-DMFC has two membranes as well as a FEC, the ohmic losses are high, accounting for $\sim$ 30% for total losses. Therefore, there is a need to determine a membrane arrangement that would reduce ohmic losses, while also reducing both methanol and water crossover fluxes. Here, the AM and CM thicknesses are individually varied and the corresponding average water crossover fluxes and crossover current density are shown in Figures 4.13 and 4.14 respectively.

The simulated results suggest that when the AM thickness, t_{AM}, is increased, the average water flux also increases in magnitude towards the cathode. The added thickness of the AM causes a lower pressure gradient across the AM, thereby diverting more of the flow

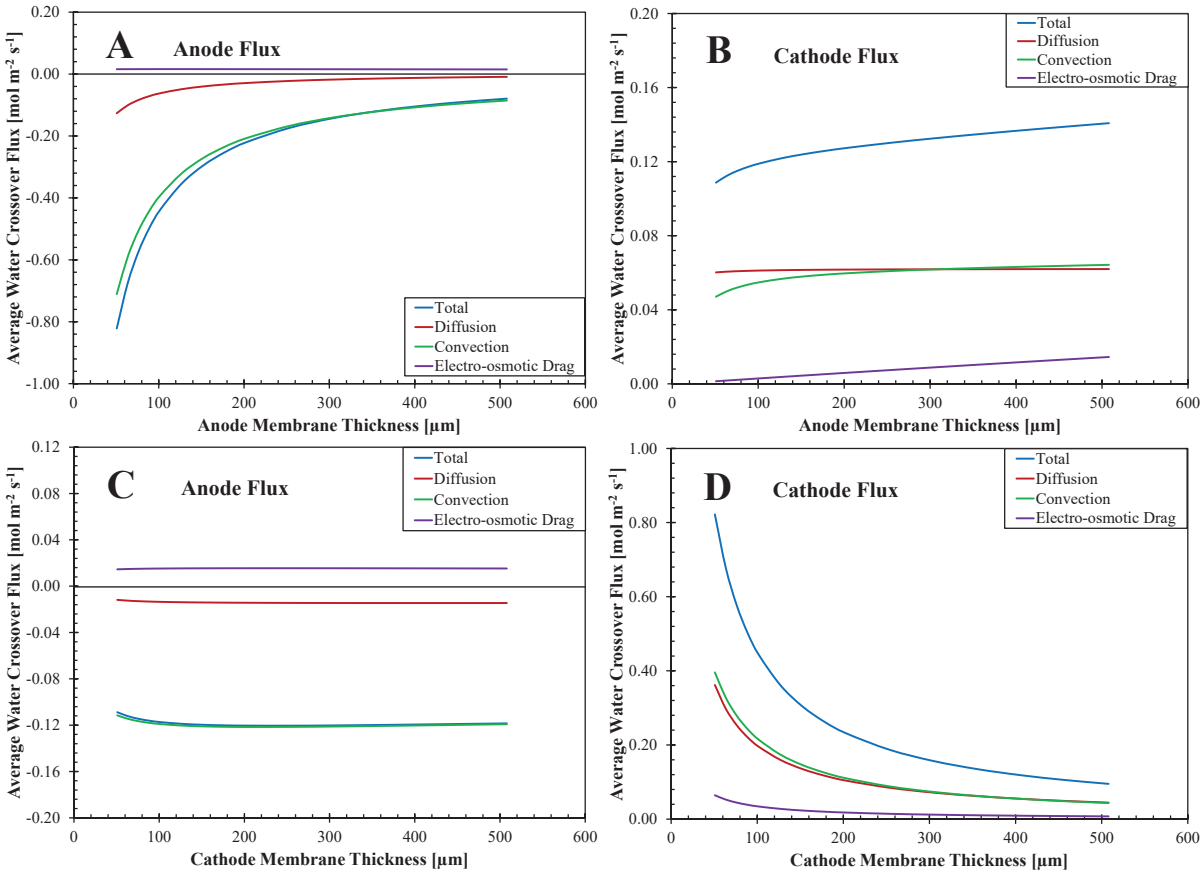

Figure 4.13: The first two figures display the modeled effect of the AM thickness on the average (a) anode and (b) cathode water crossover fluxes. Whereas the last two figures display the modeled effect of the CM thickness on the average water crossover flux in the (a) anode and (b) cathode water crossover fluxes.

towards the cathode compartment. For comparison, when $t_{AM} = 508$ μm, the average water crossover flux is estimated to be -0.08 and +0.14 mol m^{-2} s^{-1}, for the anode and cathode fluxes respectively. The anode flux was found to be primarily driven by convection, whereas the cathode flux was driven by diffusion and convection in nearly equal parts. In the reverse scenario, when the t_{AM} is decreased, more water is diverted towards the anode primarily by convection. This can be seen in Figure 4.13a-b. In the case where t_{AM} is 50.8 μm, the average water crossover flux in the anode was estimated to be -0.82 mol m^{-2} s^{-1}, which changed proportional with the AM thickness. Although this flux is high, the corresponding u within the anode compartment for a t_{AM} of 50.8 μm and 508 μm was found to be, on average, -2.5 μm s^{-1} and -22 μm s^{-1} respectively.

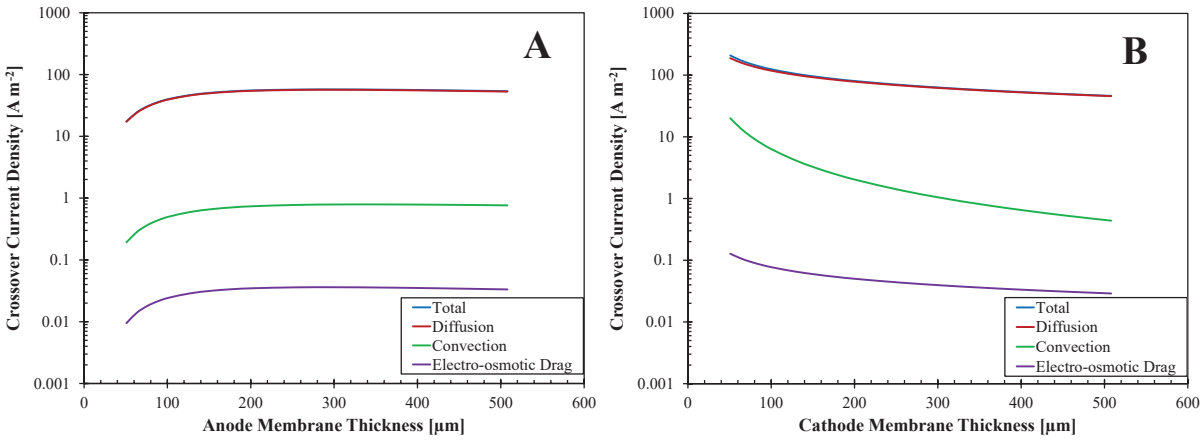

Figure 4.14: Modeled effect of the (a) AM and (b) CM thickness on the average crossover current density.

This difference in the u in both cases causes a proportional change to the crossover current density, as seen in Figure 4.14a. For comparison, in the 50.8 μm AM scenario, the strong counterflow caused little methanol crossover, 17 A m^{-2}, whereas in the 508 μm AM thickness scenario, the lower u within the anode compartment yielded a higher crossover current density of 54 A m^{-2}.

In the case where the CM thickness is varied, the same type of behaviour is observed; where a thin CM caused a higher water crossover rate towards the cathode. This thin CM diverts more water towards the cathode, yielding a higher u towards the cathode. As such, a thin CM generates a lower u within the anode compartment, thus causing a a lower mass transfer resistance within the anode, thereby increasing the methanol crossover flux. In this study, the CM thickness played a stronger role in the degree of methanol crossover, where a t_{CM} = 50.8 μm yielded a crossover current density of 210 A m^{-2}, where a CM caused the lowest crossover current density of 46 A m^{-2}.

From this analysis, the model suggests that to maximize power density, the optimal membrane arrangement is a thin AM and thick CM, as shown in Figure 4.15. From the tested cases, this corresponds to a t_{AM} = 88.9 μm and t_{CM} = 177.8 μm, corresponding

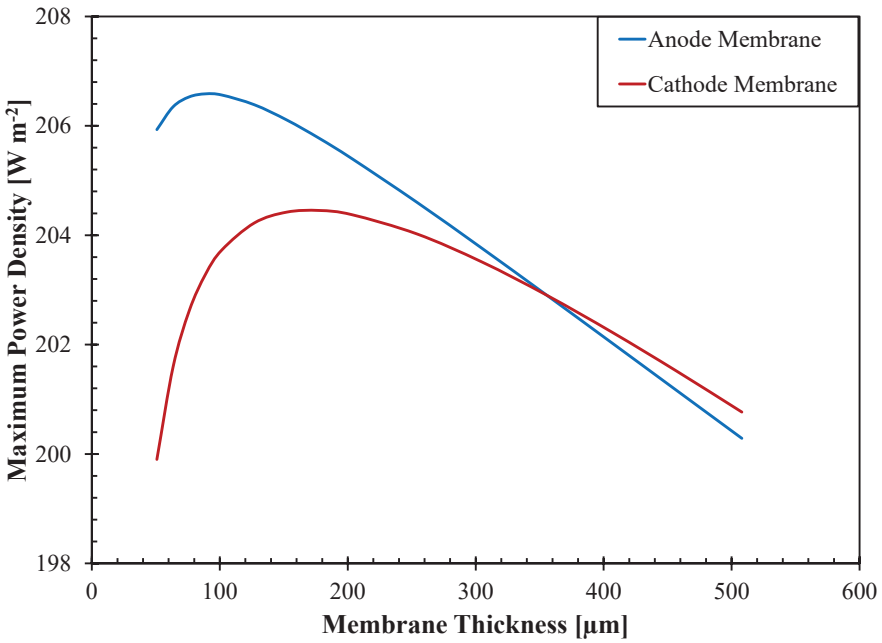

Figure 4.15: Modeled effect of the individually varied AM and CM thicknesses on the maximum power density.

closely to a Nafion® 1135 AM and a Nafion® 117 CM. This trend is consistent with Sabet-Sharghi *et al.*'s experimental findings [15]. Also, from this figure, the results suggest that the fuel cell's performance is very sensitive to the CM thickness. When the CM's thickness was decreased below the baseline thickness, this caused water to be diverted from the anode and FEC to the cathode, thereby decreasing their liquid saturation levels and in turn, decreased their conductivities. However, when the CM thickness was increased, the added thickness of the CM caused its Ohmic resistance to increase, thereby limiting the fuel cell's performance. Although this behaviour is consistent with the case where the AM thickness is varied, the diverted water mainly came from the FEC, thereby mostly dehydrating the FEC, while the AM becomes more hydrated.

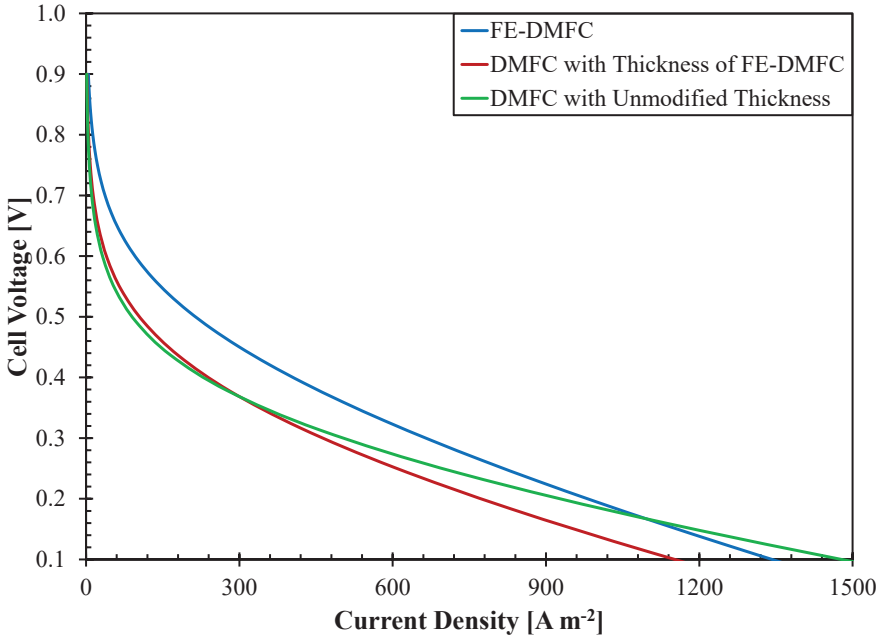

Figure 4.16: Modeled effect of the individually varied AM and CM thicknesses on the maximum power density.

4.5 Comparison of DMFC and FE-DMFC Performance

Since the FE-DMFC is intended to improve the DMFC's performance by reducing the methanol crossover flux, it is helpful to determine how effectively the FE-DMFC functions relative to the DMFC. As such, this section will compare these two fuel cells, where two DMFC configurations are compared. One where the membrane thickness is equivalent to that of the combined thickness of the AM, FEC and CM. The second DMFC only has a thickness of a traditional DMFC, with a Nafion® 117 membrane.

As can be seen in Figure 4.16, the FE-DMFC outperforms both DMFC designs up until a current density of 1100 A m^{-2}. After which, the traditional, or unmodified, DMFC outperforms the FE-DMFC and the second DMFC configuration. The improved performance of the FE-DMFC is due to the comparatively low rates of methanol crossover, shown in Figure 4.17a. Where, for example, the the FE-DMFC has a predicted $i_{xover} = 70$ A m^{-2},

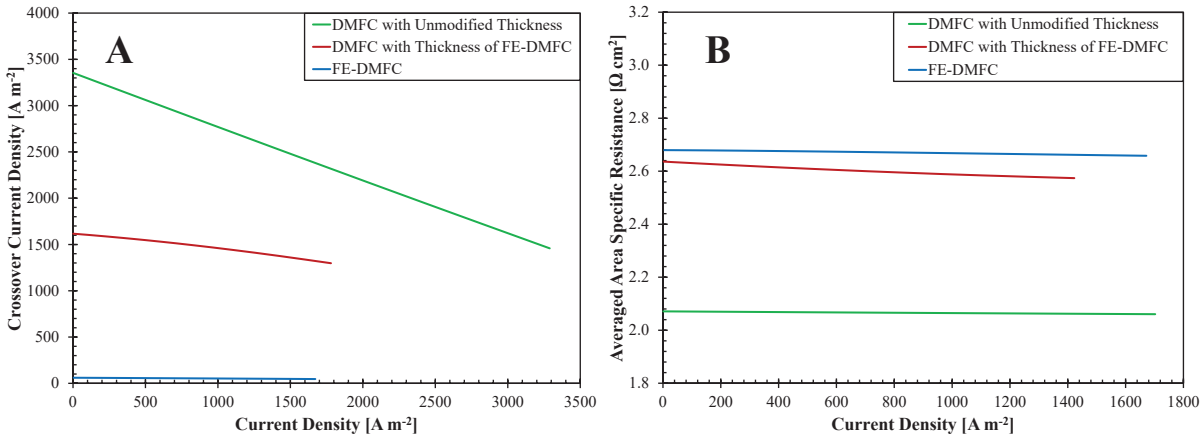

Figure 4.17: Comparison of each fuel cell configuration's modeled (a) crossover current density and (b) area specific resistance.

whereas the two DMFCs had an $i_{xover} = 3350$ A m^{-2} and 1160 A m^{-2}, for the unmodified and modified DMFCs respectively. The unmodified DMFC's i_{xover} is greater than the other configurations due to its thinner electrolyte region (membrane), which creates a greater concentration gradient across the membrane, thereby driving more methanol from the anode to the cathode. At higher operating current densities, the unmodified DMFC's lower internal resistance, shown in Figure 4.17b, allowed this fuel cell to have greater performance, thereby outperformed the other two fuel cells. Through closer examination of Figure 4.16, it can be seen that the FE-DMFC outperformed the modified DMFC, since the concentration of sulfuric acid has a corresponding conductivity that is higher than the Nafion® membranes, thereby having lower Ohmic losses. Since the unmodified DMFC's maximum current density is greater than the FE-DMFC's, primarily due to lower Ohmic losses, the FE-DMFC might benefit from a combination of very thin membranes, along within a thin and highly porous spacer. Although according to the previous findings this would likely cause a large amount of water crossover to the cathode, this could be counteracted with a higher cathode pressure.

To demonstrate the differences in the liquid methanol concentration profiles and to further show the importance of the convective transport within the FE-DMFC, the modified DMFC's and the FE-DMFC's liquid methanol concentration profiles are compared in Figure 4.18. As

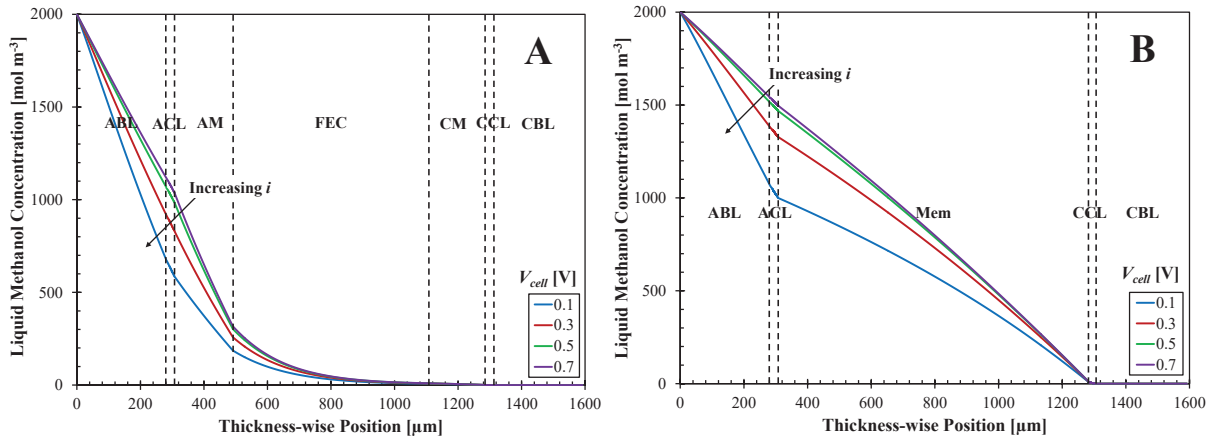

Figure 4.18: Comparison of the (a) FE-DMFC's and (b) the modified DMFC's liquid methanol concentration profile.

can be seen, the FE-DMFC's concentration within the ACL is lower than that of the DMFC's. As previously discussed, the FE-DMFC's anode is exposed to strong counterflow, caused by water crossing from the FEC to the anode, causing a reduction in the methanol concentration within the anode. The DMFC's anode does not experience this flux to the same degree, as the largest velocity within the DMFC's anode was -0.2 μm s^{-1}; whereas the FE-DMFC's mixture velocity was more than 20 times this value, at -4.4 μm s^{-1}.

Chapter 5

Conclusions and Future Work

5.1 Conclusions and Contributions

The goal of this dissertation is to understand the performance and physics of the FE-DMFC with the help of a quasi-2D multiphase model. This model improves upon the well-known MMM, by treating the whole FE-DMFC as a single domain and by formulating the governing equations in such a way where only the mixture variables are required. This formulation was achieved through a mathematical transformation that links the liquid saturation to the electrolyte concentration, removing the need for any interfacial conditions and decoupling the gaseous state from the solution process. Part of the novelty of this model is that the derivation accounts for the FEC's cross flow (which is a 2D phenomena) in a 1D manner. This inclusion was demonstrated to be capable of accounting for the net accumulation/removal of water and the net removal of methanol by the FEC, as well as account for the FEC's back-pressure needed to maintain the FEC's flow. The latter effect was shown to be of great importance in FE-DMFCs, since this back-pressure was shown be to be sufficiently high to cause water to flow from the FEC to the anode and cathode compartments. This caused flooding within the cathode, and methanol to be diluted within the anode compartment. This behaviour was verified with an analytical single phase model.

This model also demonstrated the importance of the inclusion of the material property gradient ($\nabla\psi$) when calculating the liquid saturation distribution. This term was demonstrated to account for liquid saturation jumps in a single domain manner, removing the need for explicit interfacial conditions to cause a jump to take place. This single domain approach was validated against a multi-domain analytical test case proposed in this work. The associated derivation to achieve the single domain liquid saturation jump model was also applied to the MFM approach, allowing other researchers to directly apply the derivation to their modeling work. In this work various approaches that can be used to help solve and stabilize the numerical solution are provided. Notably, a pulse function was proposed to smooth th material interfaces and allowing for a more stable model. The numerical results suggest that the choice of the pulse diffusion index, δ, within the pulse function, is rather insensitive when examined in the range of 1 μm to 100 μm. This finding could be useful for large scale computational problems where a large number of nodes are required, and liquid saturation jumps could then be resolved with little additional grid refinement. During the derivation of the model, it was shown that each governing equation could be treated as a convection-diffusion-reaction equation, thereby allowing all equations to be solved in a similar manner.

From an examination of the baseline conditions and the parametric studies, it was found that the FE-DMFC is capable of removing 98% of methanol entering through the AM. Although the examined fuel cell configuration did not recycle the FEC effluent, this caused a fuel efficiency of 44%. If the removed methanol from the FEC outlet were to be completely recycled, the fuel efficiency could be enhanced 98%. To improve the fuel cell's performance, the model suggests that a FEC thickness of 0.5 mm or less and an open FEC (porosity of one) should be used. Although an open FEC contradicts existing experimental findings, suggestions concerning the use of more rigid MEAs and the selection of properties to minimize electrolyte seepage into the anode and cathode compartments are provided. The model also

suggests that a thin AM and thick CM should be used, where the equivalent thicknesses are Nafion® 1135 and 117 for the AM and CM, respectively.

5.2 Recommendations for Future Work

From the current study there are several paths that this work could progress, both in regards to experimental and modeling studies. The recommendations for future work on the experimental and modeling analysis are listed below, beginning with the experimental studies.

- Further experimental studies could be used to help validate the numerical model. Since the numerical model used polarization curves for verification and validation, it would be useful to obtain other measurements such as activation and ohmic polarization measurements, methanol and water balance measurements, and even current distribution measurements.

- The flowing electrolyte used in this study was diluted sulfuric acid. Since this is a strong acid, it is difficult to design a fuel cell that is completely resistant to the acid. It would be useful to examine other electrolytes, both acids and bases, to determine which would be the most suitable to work with, while maintaining high performance.

- Since the majority of work done in the area of FE-DMFCs is to flow the electrolyte through the fuel cell once, it would be useful to examine alternative systems that can either recycle or separate the methanol-electrolyte mixture. These novel systems would be more practical for commerical applications and could be very beneficial on the stack level.

As for the modeling analysis, the following recommendations are made:

- Now that there is a better understanding of how the FE-DMFC functions, it would be useful to conduct both experimental and numerical optimization studies on the fuel cell to develop more efficient and powerful FE-DMFCs.

- Current FE-DMFC models assume isothermal behaviour. It would be useful to have an understanding of under what conditions this assumption is valid.

- This work demonstrated the importance of including the back-pressure caused by the cross flow within the FEC. As such, it would also be useful to account for multidimensional effects in the fuel cell to understand how the distribution of water crossover from the FEC would affect the performance of the fuel cell and the methanol crossover.

- The model assumed that the sulfuric acid could be treated as a resistor to ion conduction. In reality, the electrolyte is an aqueous solution containing anions and cations. Therefore, it would be useful to treat the FEC as an aqueous solution of ions, rather than a resistor. This inclusion could account for the hygroscopic nature of Nafion, and could potentially be accomplished through the inclusion of osmotic pressure and an activity gradient.

- The presence of the anode and cathode channels have been neglected in this study. However, it would be useful to include the effects of two-phase flow within the channels as well as the MEA through use of a separated flow model as proposed by Kablou [81]. The results obtained from this technique could also be compared to experimental observations from a flow visualization study through use of transparent flow fields.

- Once these effects have been accounted for, and have been locally validated as suggested earlier, it would be useful to perform an optimization study on the fuel cell to allow for improved FE-DMFC designs.

List of References

[1] J. Larminie and A. Dicks, *Fuel Cell Systems Explained, 2nd Edition*. West Sussex, England: John Wiley & Sons Inc., 2003.

[2] Y. Wang, K. S. Chen, J. Mishler, S. C. Cho, and X. C. Adroher, "A review of polymer electrolyte membrane fuel cells: Technology, applications, and needs on fundamental research," *Journal of Applied Energy*, vol. 88, pp. 981–1007, 2011.

[3] G. Apanel and E. Johnson, "Direct methanol fuel cells - ready to go commercial?," *Fuel Cells Bulletin*, vol. 7, pp. 12–17, 2004.

[4] T. S. Zhao, C. Xu, R. Chen, and W. W. Yang, "Mass transport phenomena in direct methanol fuel cells," *Progress in Energy and Combustion Science*, vol. 35, pp. 275–292, 2009.

[5] K. Kordesch, V. Hacker, and U. Bachhiesl, "Direct methanol-air fuel cells with membranes plus circulating electrolyte," *Journal of Power Sources*, vol. 96, pp. 200–203, 2001.

[6] G. Hoogers, *Fuel Cell Technology Handbook*. New York, New York: CRC Press, 2003.

[7] Y. P. Sun, L. Xing, and K. Scott, "Analysis of the kinetics of methanol oxidation in a porous PtRu anode," *Journal of Power Sources*, vol. 195, pp. 1–10, 2010.

[8] H. A. Gasteiger, N. Marković, P. N. Ross, and E. L. Cairns, "Methanol electrooxidation on well-characterized Pt-Ru alloys," *Journal of Physical Chemistry*, vol. 97, pp. 12020–12029, 1993.

[9] D. Ouellette, C. A. Cruickshank, and E. Matida, "Experimental investigation on the performance of a formic acid electrolyte - direct methanol fuel cell," *Journal of Fuel Cell Science and Technology*, vol. 11, pp. 26–33, 2013.

[10] V. B. Oliveira, D. S. F. ao, C. M. Rangel, and A. M. F. R. Pinto, "Heat and mass transfer effects in a direct methanol fuel cell: A 1D model," *International Journal of Hydrogen Energy*, vol. 33, pp. 3818–3828, 2008.

[11] F. Liu, *Optimizing Membrane Electrode Assembly of Direct Methanol Fuel Cells for Portable Power*. PhD thesis, Pennsylvania State University, August 2006.

[12] S. Motupally, A. J. Becker, and J. W. Weidner, "Diffusion of water in Nafion 115 membranes," *Journal of The Electrochemical Society*, vol. 147, pp. 3171–3177, 2000.

[13] K. Jiao and X. Li, "Review of water transport in polymer electrolyte membrane fuel cells," *Progress in Energy and Combustion Science*, vol. 37, pp. 221–291, 2011.

[14] N. Agmon, "The Grotthuss mechanism," *Chemical Physics Letters*, vol. 244, pp. 456–462, 1995.

[15] N. Sabet-Sharghi, C. A. Cruickshank, E. Matida, and F. Hamdullahpur, "Performance measurements of a single cell flowing electrolye-direct methanol fuel cell (FE-DMFC)," *Journal of Power Sources*, vol. 230, pp. 194–200, 2013.

[16] I. Barin, F. Sauert, E. Schultze-Rhonhof, and W. S. Sheng, *Thermochemical Data of Pure Substances - Part I*. VCH, 1989.

[17] I. Barin, F. Sauert, E. Schultze-Rhonhof, and W. S. Sheng, *Thermochemical Data of Pure Substances - Part 2*. VCH, 1989.

[18] F. Q. Liu and C. Y. Wang, "Mixed potential in a direct methanol fuel cell. Modeling and experiments," *Journal of The Electrochemical Society*, vol. 154, pp. B514–B522, 2007.

[19] A. Casalegno, P. Grassini, and R. Marchesi, "Experimental analysis of methanol cross-over in a direct methanol fuel cell," *Applied Thermal Energy*, vol. 27, pp. 748–754, 2007.

[20] K. Scott, W. M. Taama, P. Argyropoulos, and K. Sundmacher, "The impact of mass transport and methanol crossover on the direct methanol fuel cell," *Journal of Power Sources*, vol. 83, pp. 204–216, 1999.

[21] Z. Wang and C. Y. Wang, "Mathematical modeling of liquid-feed direct methanol fuel cells," *Journal of The Electrochemical Society*, vol. 150, pp. 508–519, 2003.

[22] A. J. Bard and L. R. Faulkner, *Electrochemical Methods - Fundamentals and Applications, Second edition*. John Wiley & Sons Inc., 2001.

[23] J. Newman and K. E. Thomas-Alyea, *Electrochemical Systems, 3rd Edition*. New York, New York: John Wiley & Sons Inc., 2004.

[24] J. P. Meyers and J. Newman, "Simulation of the Direct Methanol Fuel Cell - II. Modeling and Data Analysis of Transport Kinetic Phenomena," *Journal of The Electrochemical Society*, vol. 149, pp. A718–A728, 2002.

[25] K. Scott and P. Argyropoulos, "A one dimensional model of a methanol fuel cell anode," *Journal of Power Sources*, vol. 137, pp. 228–238, 2004.

[26] D. Kareemulla and S. Jayanti, "Comprehensive one-dimensional, semi-analytical, mathematical model for liquid-feed polymer electrolyte membrane direct methanol fuel cells," *Journal of Power Sources*, vol. 188, pp. 367–378, 2009.

[27] X. Ren, P. Zelenay, S. Thomas, J. Davey, and S. Gottesfeld, "Recent advances in direct methanol fuel cells at Los Alamos National Laboratory," *Journal of Power Sources*, vol. 86, pp. 111–116, 2000.

[28] M. Moore, A. Putz, and M. Secanell, "Investigation of the ORR using the double-trap intrinsic kinetic model," *Journal of The Electrochemical Society*, vol. 160, pp. F670–F681, 2013.

[29] T. Schultz, U. Krewer, and K. Sundmacher, "Impact of electrode kinetics on the dynamic response of a DMFC to change of methanol feed concentration," *Journal of Power Sources*, vol. 165, pp. 138–151, 2007.

[30] W. Sun, B. A. Peppley, and K. Karan, "An improved two-dimensional agglomerate cathode model to study the influence of catalyst layer structural parameters," *Electrochimica Acta*, vol. 50, pp. 3359–3374, 2005.

[31] A. Shah, G. S. Kim, W. Gervais, A. Young, K. Promislow, J. Li, and S. Ye, "The effects of water and microstructure on the performance of polymer electrolyte fuel cells," *Journal of Power Sources*, vol. 160, pp. 1251–1268, 2006.

[32] Z. Miao, Y. L. He, X. L. Li, and J. Q. Zou, "A two-dimensional two-phase mass transport model for direct methanol fuel cells adopting a modified agglomerate approach," *Journal of Power Sources*, vol. 185, pp. 1233–1246, 2008.

[33] P. K. Das, X. Li, and Z. S. Liu, "A three-dimensional agglomerate model for the cathode catalyst layer of PEM fuel cells," *Journal of Power Sources*, vol. 179, pp. 186–199, 2008.

[34] S. Kamarajugadda and S. Mazumder, "Generalized flooded agglomerate model for the cathode catalyst layer of a polymer electrolyte membrane fuel cell," *Journal of Power Sources*, vol. 208, pp. 328–339, 2012.

[35] C. O. Colpan, C. A. Cruickshank, E. Matida, and F. Hamdullahpur, "1D modeling of a flowing electrolyte-direct methanol fuel cell," *Journal of Power Sources*, vol. 196, pp. 3572–3582, 2011.

[36] M. Secanell, K. Karan, A. Suleman, and N. Djilali, "Optimal design of ultralow-platinum PEMFC anode electrodes," *Journal of The Electrochemical Society*, vol. 155, pp. B125–B134, 2008.

[37] S. Sharma and B. G. Pollet, "Support materials for PEMFC and DMFC electrocatalysts - A review," *Journal of Power Sources*, vol. 208, pp. 96–119, 2012.

[38] M. Ahmed and I. Dincer, "A review on methanol crossover in direct methanol fuel cell: challenges and achievements," *International Journal of Energy Research*, vol. 35, pp. 1213–1228, 2011.

[39] V. Neburchilov, J. Martin, H. Wang, and J. Zhang, "A review of polymer electrolyte membranes for direct methanol fuel cells," *Journal of Power Sources*, vol. 169, pp. 221–238, 2007.

[40] X. Y. Li, W. W. Yang, Y. L. He, T. S. Zhao, and Z. G. Qu, "Effect of anode micro-porous layer on species crossover through the membrane of the liquid-feed direct methanol fuel cells," *Applied Thermal Energy*, vol. 48, pp. 392–401, 2012.

[41] C. Shaffer and C. Y. Wang, "Role of hydrophobic anode MPL in controlling water crossover in DMFC," *Electrochimica Acta*, vol. 54, pp. 5761–5769, 2009.

[42] G. Zehl, P. Bogdanoff, I. Dorbandt, S. Fiechter, K. Wippermann, and C. Hartnig, "Carbon supported Ru-Se as methanol tolerant catalysts for DMFC cathodes. Part I: preparation and characterization of catalysts," *Journal of Applied Electrochemistry*, vol. 37, pp. 1475–1484, 2007.

[43] K. Wippermann, B. Richter, K. Klafki, J. Mergel, G. Zehl, I. Dorbandt, P. Bogdanoff, S. Fiechter, and S. Kaytakoglu, "Carbon supported Ru-Se as methanol tolerant catalysts for DMFC cathodes. Part II: preparation and characterization of MEAs," *Journal of Applied Electrochemistry*, vol. 37, pp. 1399–1411, 2007.

[44] H. Li, Y. Tang, Z. Wang, Z. Shi, S. Wu, D. Song, J. Zhang, K. Fatih, J. Zhang, H. Wang, Z. Liu, R. Abouatallah, and A. Mazza, "A review of water flooding issues in the proton exchange membrane fuel cell," *Journal of Power Sources*, vol. 178, pp. 103–117, 2008.

[45] W. Dai, H. Wang, X. Z. Yuan, J. J. Martin, D. Yang, J. Qiao, and J. Ma, "A review on water balance in the membrane electrode assembly of proton exchange membrane fuel cells," *International Journal of Hydrogen Energy*, vol. 34, pp. 9461–9478, 2009.

[46] M. Zago, A. Casalegno, F. Bresciani, and R. Marchesi, "Effect of anode MPL on water and methanol transport in DMFC: Experimental and modeling analyses," *International Journal of Hydrogen Energy*, vol. 39, pp. 21620–21630, 2014.

[47] M. Ji and Z. Wei, "A review of water management in polymer electrolyte membrane fuel cells," *Energies*, vol. 2, pp. 1057–1106, 2009.

[48] P. Argyropoulos, K. Scott, and W. M. Taama, "Carbon dioxide evolution patterns in direct methanol fuel cells," *Electrochimica Acta*, vol. 44, pp. 3575–3584, 1999.

[49] H. Yang, T. S. Zhao, and Q. Ye, "In situ visualization study of CO_2 gas bubble behavior in DMFC anode flow fields," *Journal of Power Sources*, vol. 139, pp. 79–90, 2005.

[50] N. S. Rosenthal, S. A. Vilekar, and R. Datta, "A comprehensive yet comprehensible analytical model for the direct methanol fuel cell," *Journal of Power Sources*, vol. 206, pp. 129–143, 2012.

[51] K. Scott, P. Argyropoulos, and K. Sundmacher, "A model for the liquid feed direct methanol fuel cell," *Journal of Electroanalytical Chemistry*, vol. 477, pp. 97–110, 1999.

[52] R. Chen, T. S. Zhao, W. W. Yang, and C. Xu, "Two-dimensional two-phase thermal model for passive direct methanol fuel cells," *Journal of Power Sources*, vol. 175, pp. 276–287, 2008.

[53] J. H. Nam and M. Kaviany, "Effective diffusivity and water-saturation distribution in single- and two-layer PEMFC diffusion medium," *International Journal of Heat and Mass Transfer*, vol. 46, pp. 4595–4611, 2003.

[54] W. W. Yang and T. S. Zhao, "A two-dimensional, two-phase mass transport model for liquid-feed DMFCs," *Electrochimica Acta*, vol. 52, pp. 6125–6140, 2007.

[55] C. Xu, T. S. Zhao, and W. W. Yang, "Modeling of water transport through membrane electrode assembly of direct methanol fuel cells," *Journal of Power Sources*, vol. 178, pp. 291–308, 2008.

[56] J. Rice and A. Faghri, "A transient, multi-phase and multi-component model of a new passive DMFC," *International Journal of Heat and Mass Transfer*, vol. 49, pp. 4804–4820, 2006.

[57] C. Y. Wang and P. Chen, "A multiphase mixture model for multiphase, multicomponent transport in capillary porous media - I. Model development," *International Journal of Heat and Mass Transfer*, vol. 39, pp. 3607–3618, 1996.

[58] W. Liu and C. Y. Wang, "Three-dimensional simulations of liquid feed direct methanol fuel cells," *Journal of The Electrochemical Society*, vol. 154, pp. B352–B361, 2007.

[59] U. Pasaogullari and C. Y. Wang, "Two-phase transport and the role of micro-porous layer in polymer electrolyte fuel cells," *Electrochimica Acta*, vol. 49, pp. 4359–4369, 2004.

[60] U. Pasaogullari and C. Y. Wang, "Two-phase modeling and flooding prediction of polymer electrolyte fuel cells," *Journal of The Electrochemical Society*, vol. 152, pp. A380–A390, 2005.

[61] C. Y. Wang and C. Beckermann, "A two-phase mixture model of liquid-gas flow and heat transfer in capillary porous media - l. Formulation," *International Journal of Heat and Mass Transfer*, vol. 36, pp. 2747–2758, 1993.

[62] C. Y. Wang and P. Cheng, "Multiphase flow and heat transfer in porous media," *Advances in Heat Transfer*, vol. 30, pp. 93–196, 1997.

[63] S. Mazumder and J. V. Cole, "Rigorous 3-D mathematical modeling of PEM fuel cells: I. model predictions without liquid water transport," *Journal of The Electrochemical Society*, vol. 150, pp. A1503–A1509, 2003.

[64] S. Mazumder and J. V. Cole, "Rigorous 3-D mathematical modeling of PEM fuel cells: II. model predictions with liquid water transport," *Journal of The Electrochemical Society*, vol. 150, pp. A1510–A1517, 2003.

[65] P. C. Sui, S. Kumar, and N. Djilali, "Advanced computational tools for PEM fuel cell design. Part 1. Development and base case simulations," *Journal of Power Sources*, vol. 180, pp. 410–422, 2008.

[66] X. Wang and T. V. Nguyen, "Modeling the effects of capillary property of the porous media on the performance of the cathode of a PEMFC," *Journal of The Electrochemical Society*, vol. 155, pp. B1085–B1092, 2008.

[67] S. Jung, "Non-isothermal multi-dimensional direct methanol fuel cell model with micro-porous layers mitigating water/methanol crossover," *Journal of Power Sources*, vol. 231, pp. 60–81, 2013.

[68] N. P. Siegel, M. W. Ellis, D. J. Nelson, and M. R. von Spakovsky, "Single domain PEMFC model based on agglomerate catalyst geometry," *Journal of Power Sources*, vol. 115, pp. 81–89, 2003.

[69] S. Um, C. Y. Wang, and K. S. Chen, "Computational fluid dynamics modeling of proton exchange membrane fuel cells," *Journal of The Electrochemical Society*, vol. 147, pp. 4485–4493, 2000.

[70] J. J. Baschuk and X. Li, "A comprehensive, consistent and systematic mathematical model of PEM fuel cells," *Journal of Applied Energy*, vol. 86, pp. 181–193, 2009.

[71] V. Gurau, H. Liu, and S. Kakac, "Two-dimensional model for proton exchange membrane fuel cells," *AIChE Journal*, vol. 44, pp. 2410–2422, 1998.

[72] U. Pasaogullari, C. Y. Wang, and K. S. Chen, "Two-phase transport in polymer electrolyte fuel cells with bilayer cathode gas diffusion media," *Journal of The Electrochemical Society*, vol. 152, pp. A1574–A1582, 2005.

[73] A. Z. Weber and J. Newman, "Effects of microporous layers in polymer electrolyte fuel cells," *Journal of The Electrochemical Society*, vol. 152, pp. A677–A688, 2005.

[74] X. Wang and T. V. Nguyen, "Modeling the effects of the microporous layer on the net water transport rate across the membrane in a PEM fuel cell," *Journal of The Electrochemical Society*, vol. 157, pp. B496–B505, 2010.

[75] W. W. Yang and T. S. Zhao, "Numerical investigation of effect of membrane electrode assembly structure on water crossover in a liquid-feed direct methanol fuel cell," *Journal of Power Sources*, vol. 188, pp. 433–446, 2009.

[76] Q. Ye and T. V. Nguyen, "Three-dimensional simulation of liquid water distribution in a PEMFC with experimentally measured capillary functions," *Journal of The Electrochemical Society*, vol. 154, pp. B1242–B1251, 2007.

[77] H. Wu, X. Li, and P. Berg, "On the modeling of water transport in polymer electrolyte membrane fuel cells," *Electrochimica Acta*, vol. 54, pp. 6913–6927, 2009.

[78] Z. Miao, Y. L. He, and J. Q. Zou, "Modeling the effect of anisotropy of gas diffusion layer on transport phenomena in a direct methanol fuel cell," *Journal of Power Sources*, vol. 195, pp. 3693–3708, 2010.

[79] K. Kang and H. Ju, "Numerical modeling and analysis of micro-porous layer effects in polymer electrolyte fuel cells," *Journal of Power Sources*, vol. 194, pp. 763–773, 2009.

[80] N. Sabet-Sharghi, "Experimental analysis of a single cell flowing electrolyte-direct methanol fuel cell," Master's thesis, Carleton University, August 2011.

[81] Y. Kablou, "Hydrodynamic modelling and experimental analysis of FE-DMFC stacks," Master's thesis, Carleton University, April 2012.

[82] E. Duivesteyn, "Fluid dynamics modelling and experimental studies of the flowing electrolyte channel in a flowing electrolyte - direct methanol fuel cell," Master's thesis, Carleton University, December 2013.

[83] E. Kjeang, J. Goldak, M. Golriz, J. Gu, D. James, and K. Kordesch, "A parametric study of methanol crossover in a flowing electrolyte-direct methanol fuel cell," *Journal of Power Sources*, vol. 153, pp. 90–99, 2006.

[84] E. Kjeang, J. Goldak, M. Golriz, J. Gu, D. James, and K. Kordesch, "Modeling methanol crossover by diffusion and electro-osmosis in a flowing electrolyte-direct methanol fuel cell," *Fuel Cells*, vol. 4, pp. 486–498, 2005.

[85] C. O. Colpan, A. Fung, and F. Hamdullahpur, "2D modeling of a flowing electrolyte-direct methanol fuel cell," *Journal of Power Sources*, vol. 209, pp. 301–311, 2012.

[86] E. Duivesteyn, C. A. Cruickshank, and E. Matida, "Modelling of a porous flowing electrolyte layer in a flowing electrolyte direct methanol fuel cell," *International Journal of Hydrogen Energy*, vol. 38, pp. 13434–13442, 2013.

[87] E. Duivesteyn, C. A. Cruickshank, and E. Matida, "Nonisothermal hydrodynamic modeling of the flowing electrolyte channel in a flowing electrolyte-direct methanol fuel cell," *Journal of Fuel Cell Science and Technology*, vol. 11, pp. 85–90, 2013.

[88] J. Ge and H. Liu, "A three-dimensional two-phase model for a liquid-feed direct methanol fuel cell," *Journal of Power Sources*, vol. 163, pp. 907–915, 2007.

[89] H. Meng and C. Y. Wang, "Model of two-phase flow and flooding dynamics in polymer electrolyte fuel cells," *Journal of The Electrochemical Society*, vol. 152, pp. A1733–A1741, 2005.

[90] D. Ouellette, C. O. Colpan, E. Matida, C. A. Cruickshank, and F. Hamdullahpur, "A comprehensive 1D model of a flowing electrolyte - direct methanol fuel cell with experimental validation," *International Journal of Energy Research*, vol. 39, pp. 33–45, 2015.

[91] D. Ouellette, C. O. Colpan, E. Matida, and C. A. Cruickshank, "A single domain approach to modeling the multiphase flow within a flowing electrolyte - direct methanol fuel cell," *International Journal of Hydrogen Energy*, vol. 40, pp. 7817–7828, 2015.

[92] D. Ouellette, C. O. Colpan, C. A. Cruickshank, and E. Matida, "Parametric studies on the membrane arrangement and porous properties of the flowing electrolyte channel in a flowing electrolyte - direct methanol fuel cell," *International Journal of Hydrogen Energy*, vol. 40, pp. 7732–7742, 2015.

[93] F. Bresciani, A. Casalegno, J. L. Bonde, M. Odgaard, and R. Marchesi, "A comparison of operating strategies to reduce DMFC degradation," *International Journal of Energy Research*, vol. 38, pp. 117–124, 2014.

[94] F. Bresciani, A. Casalegno, M. Zago, and R. Marchesi, "A parametric analysis on DMFC anode degradation," *Fuel Cells*, vol. 14, pp. 386–394, 2014.

[95] A. A. Kulikovsky, "A model for carbon and Ru corrosion due to methanol depletion in DMFC," *Electrochimica Acta*, vol. 56, pp. 9846–9850, 2011.

[96] H. Bajpai, M. Khandelwal, E. C. Kumbur, and M. M. Mench, "A computational model for assessing impact of interfacial morphology on polymer electrolyte fuel cell performance," *Journal of Power Sources*, vol. 195, pp. 4196–4205, 2010.

[97] D. S. Falcao, V. B. Oliveira, C. M. Rangel, and A. M. F. R. Pinto, "Water transport through a PEM fuel cell: A one-dimensional model with heat transfer effects," *Chemical Engineering Science*, vol. 64, pp. 2216–2225, 2009.

[98] E. Afshari and S. A. Jazayeri, "Analyses of heat and water transport interactions in a proton exchange membrane fuel cell," *Journal of Power Sources*, vol. 194, pp. 423–432, 2009.

[99] N. Djilali and D. Lu, "Influence of heat transfer on gas and water transfer in fuel cells," *International Journal of Thermal Sciences*, vol. 41, pp. 29–40, 2002.

[100] K. S. Pitzer, "Thermodynamics of electrolytes. I. Theoretical basis and general equations," *Journal of Physical Chemistry*, vol. 77, pp. 268–277, 1973.

[101] S. Ge, X. Li, B. Yi, and I. M. Hsing, "Absorption, desorption and transport of water in polymer electrolyte membranes for fuel cells," *Journal of The Electrochemical Society*, vol. 152, pp. A1149–A1157, 2005.

[102] H. Wu, *Mathematical modeling of transient transport phenomena in PEM fuel cells*. PhD thesis, University of Waterloo, 2009.

[103] I. Nitta, T. Hottinen, O. Himanen, and M. Mikkola, "Inhomogeneous compression of PEMFC gas diffusion layer. Part I. Experimental," *Journal of Power Sources*, vol. 171, pp. 26–36, 2007.

[104] T. Hottinen, O. Himanen, S. Karvonen, and I. Nitta, "Inhomogeneous compression of PEMFC gas diffusion layer. Part II. Modeling the effect," *Journal of Power Sources*, vol. 171, pp. 113–121, 2007.

[105] P. C. Sui and N. Djilali, "Analysis of coupled electron and mass transport in the gas diffusion layer of a PEM fuel cell," *Journal of Power Sources*, vol. 161, pp. 294–300, 2006.

[106] A. Weber, *Modeling water management in polymer-electrolyte fuel cells*. PhD thesis, University of California, Berkeley, 2004.

[107] A. Z. Weber, R. M. Darling, and J. Newman, "Modeling two phase behavior in PEFCs," *Journal of The Electrochemical Society*, vol. 151, pp. A1715–A1727, 2004.

[108] J. T. Wang, S. Wasmus, and R. F. Savinell, "Real-time mass spectrometric study of the methanol crossover in a direct methanol fuel cell," *Journal of The Electrochemical Society*, vol. 143, pp. 1233–1239, 1996.

[109] Y. Wang and C. Y. Wang, "Modeling polymer electrolyte fuel cells with large density and velocity changes," *Journal of The Electrochemical Society*, vol. 152, pp. A445–A453, 2005.

[110] M. Kaviany, *Principles of Heat Transfer in Porous Media*. New York, New York: Springer, 1999.

[111] M. Muskat and R. D. Wyckoff, *The Flow of Homogeneous Fluids Through Porous Media, First Edition*. Ann Arbor, Michigan: McGraw-Hill Book Company, Inc., 1937.

[112] J. C. Slattery, "Two-phase flow through porous media," *American Institute of Chemical Engineers Journal*, vol. 16, pp. 345–352, 1970.

[113] C. Hartnig, I. Manke, J. Schloesser, P. Krüger, R. Kuhn, H. Riesemeier, K. Wippermann, and J. Banhart, "High resolution synchrotron X-ray investigation of carbon dioxide evolution in operating direct methanol fuel cells," *Electrochemistry Communications*, vol. 11, pp. 1559–1562, 2009.

[114] G. Q. Lu and C. Y. Wang, "Electrochemical and flow characterization of a direct methanol fuel cell," *Journal of Power Sources*, vol. 134, pp. 33–40, 2004.

[115] H. Yang and T. S. Zhao, "In situ visualization study of CO_2 gas bubble behavior in DMFC anode flow fields," *Journal of Power Sources*, vol. 139, pp. 79–90, 2005.

[116] U. Pasaogullari, *Two-Phase Transport and Prediction of Flooding in Polymer Electrolyte Fuel Cells*. PhD thesis, Pennsylvania State University, August 2005.

[117] K. D. Kreuer, "On the development of proton conducting polymer membranes for hydrogen and methanol fuel cells," *Journal of Membrane Science*, vol. 185, pp. 29–39, 2001.

[118] S. Motupally, A. J. Becker, and J. W. Weidner, "Diffusion of water in Nafion 115 membranes," *Journal of The Electrochemical Society*, vol. 147, pp. 3171–3177, 2000.

[119] S. Kamarajugadda and S. Mazumder, "Numerical investigation of the effect of cathode catalyst layer structure and composition on polymer electrolyte membrane fuel cell performance," *Journal of Power Sources*, vol. 183, pp. 629–642, 2008.

[120] J. Nordlund and G. Lindbergh, "A model for the porous direct methanol fuel cell anode," *Journal of The Electrochemical Society*, vol. 149, pp. A1107–A1113, 2002.

[121] G. Lin, W. He, and T. V. Nguyen, "Modeling liquid water effects in the gas diffusion and catalyst layers of the cathode of the PEM fuel cell," *Journal of The Electrochemical Society*, vol. 151, pp. A1999–A2006, 2004.

[122] R. M. Rao and R. Rengaswamy, "A distributed dynamic model for chronoamperometry, chronopotentiometry and gas starvation studies in PEM fuel cell cathode," *Chemical Engineering Science*, vol. 61, pp. 7393–7409, 2006.

[123] N. Khajeh-Hosseini, M. Fesanghary, K. Fushinobu, and K. Okazaki, "A study of the agglomerate catalyst layer for the cathode side of a proton exchange membrane fuel cell: Modeling and optimization," *Electrochimica Acta*, vol. 60, pp. 55–65, 2012.

[124] H. K. Versteeg and W. Malalasekera, *Computational Fluid Dynamics - The Finite Volume Method, Second Edition*. Essex, England: Pearson Education Ltd., 2007.

[125] S. V. Patankar, *Numerical Heat Transfer and Fluid Flow*. New York, New York: Hemisphere Publishing Corporation, 1980.

[126] National Institute of Standards and Technology, "Thermophysical Properties of Fluid Systems," July 2011.

[127] H. E. Darling, "Conductivity of sulfuric acid solutions," *Journal of Chemical and Engineering Data*, vol. 9, pp. 421–426, 1964.

[128] A. A. Kulikovsky, J. Divisek, and A. A. Kornyshev, "Two-dimensional simulation of direct methanol fuel cell - A new (embedded) type of current collector," *Journal of The Electrochemical Society*, vol. 147, pp. 953–959, 2000.

[129] L. Xing, X. Song, K. Scott, V. Pickert, and W. Cao, "Multi-variable optimisation of PEMFC cathodes based on surrogate modelling," *International Journal of Hydrogen Energy*, vol. 38, pp. 14295–14313, 2013.

[130] S. Mazumder, "A generalized phenomenological model and database for the transport of water and current in polymer electrolyte membranes," *Journal of The Electrochemical Society*, vol. 152, pp. A1633–A1644, 2005.

[131] F. Q. Liu and C. Y. Wang, "Low crossover of methanol and water through thin membranes in direct methanol fuel cell," *Journal of The Electrochemical Society*, vol. 153, pp. A543–A553, 2006.

[132] F. Meier, J. Kerres, and G. Eigenberger, "Methanol diffusion in water swollen ionomer membranes for DMFC applications," *Journal of Membrane Science*, vol. 241, pp. 137–141, 2004.

[133] R. B. Bird, W. E. Stewart, and E. N. Lightfoot, *Transport Phenomena, 2^{nd} Edition*. New York, New York: John Wiley & Sons Inc., 2007.

[134] R. H. Perry, D. W. Green, and J. O. Maloney, *Perry's Chemical Engineer's Handbook, Seventh Edition*. New York, New York: McGraw-Hill, 1997.

[135] L. Xing, X. Liu, T. Alaje, R. Kumar, M. Mamlouk, and K. Scott, "A two-phase flow and non-isothermal agglomerate model for a proton exchange membrane (PEM) fuel cell," *Energy*, vol. 73, pp. 618–634, 2014.

[136] J. C. Amphlett, R. M. Baumert, R. F. Mann, B. A. Peppley, P. R. Roberge, and T. J. Harris, "Performance modeling of the Ballard Mark IV solid polymer electrolyte fuel cell. I. Mechanistic model development," *Journal of The Electrochemical Society*, vol. 142, pp. 1–8, 1995.

[137] K. Scott, W. Taama, and J. Cruickshank, "Performance and modelling of a direct methanol solid polymer electrolyte fuel cell," *Journal of Power Sources*, vol. 65, pp. 159–171, 1997.

[138] T. E. Springer, T. A. Zawodzinski, and S. Gottensfeld, "Polymer electrolyte fuel cell model," *Journal of The Electrochemical Society*, vol. 138, pp. 2334–2342, 1991.

[139] J. Ge and H. Liu, "A three-dimensional mathematical model for a liquid-feed direct methanol fuel cell," *Journal of Power Sources*, vol. 160, pp. 413–421, 2006.

[140] S. H. Jung, *Modeling and Control of Two-Phase Flow in Direct Methanol Fuel Cells*. PhD thesis, Pennsylvania State University, August 2010.

[141] U. Pasaogullari and C. Y. Wang, "Liquid water transport in gas diffusion layer of polymer electrolyte fuel cells," *Journal of The Electrochemical Society*, vol. 151, pp. A399–A406, 2004.

[142] P. K. Das, X. Li, and Z. S. Liu, "Analysis of liquid water transport in cathode catalyst layer of PEM fuel cells," *International Journal of Hydrogen Energy*, vol. 35, pp. 2403–2416, 2010.

[143] ASME, *Measurement Uncertainty - Part 1. Instruments and Apparatus*. ANSI/ASME PTC 19.1, 1985.

[144] F. Bresciani, A. Casalegno, M. Zago, and R. Marchesi, "Systematic experimental analysis of a direct methanol fuel cell," *Journal of Fuel Cell Engineering, Science and Technology*, vol. 4, pp. 418–424, 2006.

[145] T. G. Kolda, R. M. Lewis, and V. Torczon, "Optimization by direct search: New perspectives on some classical and modern methods," *SIAM Review*, vol. 45, pp. 385–482, 2003.

[146] P. Argyropoulos, K. Scott, A. K. Shukla, and C. Jackson, "Empirical model equations for the direct methanol fuel cell," *Fuel Cells*, vol. 2, pp. 78–82, 2002.

[147] W. Q. Tao, C. H. Min, X. L. Liu, Y. L. He, B. H. Yin, and W. Jiang, "Parameter sensitivity examination and discussion of PEM fuel cell simulation model validation. Part I. Current status of modeling research and model development," *Journal of Power Sources*, vol. 160, pp. 359–373, 2006.

[148] C. H. Min, Y. L. He, X. L. Liu, B. H. Yin, W. Jiang, and W. Q. Tao, "Parameter sensitivity examination and discussion of PEM fuel cell simulation model validation. Part II. Results of sensitivity analysis and validation of the model," *Journal of Power Sources*, vol. 160, pp. 374–385, 2006.

[149] H. Guo and C. Ma, "2D analytical model of a direct methanol fuel cell," *Electrochemistry Communications*, vol. 6, pp. 306–312, 2004.

[150] B. L. García, V. A. Sethuraman, J. W. Weidner, R. E. White, and R. Dougal, "Mathematical model of a direct methanol fuel cell," *Journal of Fuel Cell Science and Technology*, vol. 1, pp. 43–48, 2004.

Appendix A

Derivation of the Liquid Saturation Equation for the Multi-Fluid Model (MFM)

Even though the MFM is not used in this dissertation, a single domain liquid saturation equation can still be derived by applying of the approach detailed in Section 2.3.4. The advantage of this proposed approach, is that liquid saturation jumps can now occur without the need of any explicit interfacial treatment. The extension to the MFM is provided in this appendix for completeness. Typically, in the MFM, the liquid saturation is inferred from the liquid phase continuity and momentum equations. Assuming Darcy's Law holds, the momentum equation can be substituted into the continuity equation, taking the form shown below. Any additional terms, such as body forces, are assumed to be bundled into the liquid phase source term, $S_{gen,l}$.

$$\nabla \cdot \left[-\frac{K k_{rl}}{\nu_l} (\nabla P_l) \right] = S_{gen,l} \tag{A.1}$$

If the capillary pressure equation follows the same form as discussed in this dissertation (i.e.: $P_{cap} = P_g - P_l$), then this equation can be rearranged for the liquid phase pressure and substituted into Equation A.1, as shown below.

$$\nabla \cdot \left[\frac{K k_{rl}}{\nu_l} (\nabla P_{cap}) - \frac{K k_{rl}}{\nu_l} (\nabla P_g) \right] = S_{gen,l} \tag{A.2}$$

The gaseous pressure gradient from the previous equation can then be replaced by Darcy's Law of the gaseous phase and substituted into Equation A.2. This produces a set of terms (the second set of terms on the left hand side of Equation A.3) which accounts for the interfacial drag between the gaseous and liquid phases.

$$\nabla \cdot \left[\frac{K k_{rl}}{\nu_l} (\nabla P_{cap}) + \frac{k_{rl} \nu_g}{k_{rg} \nu_l} (\rho_g \mathbf{u_g}) \right] = S_{gen,l} \tag{A.3}$$

The functional form of the capillary pressure can be separated into its liquid saturation and material property dependencies through the chain rule, as shown below. It should be noted that the mixture concentration of water, C^{H_2O}, is not used in Equation A.4, since this modeling approach treats each phase separately and thus not as a mixture.

$$\nabla \cdot \left[\frac{K k_{rl}}{\nu_l} \left(\frac{\partial P_{cap}}{\partial s} (\nabla s) + \frac{\partial P_{cap}}{\partial \psi} (\nabla \psi) \right) + \frac{k_{rl} \nu_g}{k_{rg} \nu_l} (\rho_g \mathbf{u_g}) \right] = S_{gen,l} \tag{A.4}$$

Assuming the capillary pressure - liquid saturation relationship follows the Young-Laplace equation ($P_{cap} = \psi J$), then Equation A.4 takes the form shown below.

$$\nabla \cdot \left[-D^s_{cap} (\nabla s) - D^{\psi}_{cap} (\nabla \psi) + \frac{k_{rl} \nu_g}{k_{rg} \nu_l} (\rho_g \mathbf{u_g}) \right] = S_{gen,l} \tag{A.5}$$

The liquid saturation and Young-Laplace capillary diffusion coefficients, D^s_{cap} and D^{ψ}_{cap} respectively, take the form shown below.

$$D^s_{cap} = -\frac{K k_{rl} \psi}{\nu_l} \frac{\partial J}{\partial s} \tag{A.6a}$$

$$D^{\psi}_{cap} = -\frac{K k_{rl}}{\nu_l} J \tag{A.6b}$$

As can be seen, Equation A.5 is the same form as used in many previous MFM models [76–78]. However, this dissertation proposes the use of an extra set of terms that accounts for the non-uniformity in material properties (the second set of terms in Equation A.5). This

new set of terms allows for any required jump to occur to the liquid saturation, without the need of any explicit interfacial treatment. If required, the derivation can be applied to the gaseous continuity and momentum equations, rather than the liquid state, to achieve the same end. The final results are shown below.

$$\nabla \cdot \left[-D^{s}_{cap}(\nabla s) - D^{\psi}_{cap}(\nabla \psi) + \frac{k_{rg}\nu_l}{k_{rl}\nu_g}(\rho_l \mathbf{u_l}) \right] = S_{gen,g} \tag{A.7a}$$

$$D^{s}_{cap} = -\frac{K k_{rg} \psi}{\nu_g} \frac{\partial J}{\partial s} \tag{A.7b}$$

$$D^{\psi}_{cap} = -\frac{K k_{rg}}{\nu_g} J \tag{A.7c}$$

Appendix B

Correlations and Properties Used for Modeling Studies

Table B.1: Boundary conditions used for the baseline operating conditions in the presented modeling studies. The second set of subscripts under the the symbol column represents the corresponding interfaces for that variable.

Variable	Symbol	Value	Units
Molar Concentration			
C_l^{MeOH}	$C_{l,AFC-ABL}^{MeOH}$	2000	mol m^{-3}
	$C_{l,CCL-CBL}^{MeOH}$	0	mol m^{-3}
C^{H_2O}	$s_{AFC-ABL}$	0.9	-
	$s_{CBL-CAC}$	0.05	-
	$RH_{CBL-CAC}$	1	-
$C_g^{O_2}$	$C_{g,CBL-CAC}^{O_2}$	$x^{O_2}\frac{P_{CBL-CAC}}{\bar{R}T}$	mol m^{-3}
	$\dot{\mathbf{N}}''^{\mathbf{O_2}}_{\mathbf{g,CM-CCL}}$	0	mol m^{-3}
Inlet Pressures			
P	$P_{AFC-ABL}$	0.5	kPa$_g$
	$P_{CBL-CAC}$	20	kPa$_g$
Electronic and Ionic Potential			
Φ_s	$\Phi_{s,AFC-ABL}$	$-\frac{I}{A_{rib}}R_{contact}$	V
	$\mathbf{i_{s,ACL-AM}}$	0	A m^{-2}
	$\mathbf{i_{s,CM-CCL}}$	0	A m^{-2}
Φ_e	$\Phi_{s,CBL-CAC}$	V_{cell}	V
	$\mathbf{i_{e,ABL-ACL}}$	0	A m^{-2}
	$\mathbf{i_{e,CCL-CBL}}$	0	A m^{-2}

Table B.2: Electrochemical and transport properties used in modeling study.

Parameter	Symbol	Expression	Units	Reference
Diffusion Coefficients				
Methanol in water	$D_{o,l}^{MeOH}$	$1.58 \times 10^{-9} \exp\left[0.02623(T - 298.15)\right]$	$m^2\ s^{-1}$	[55]
Methanol in Nafion®	D_e^{MeOH}	$10^{-10}\left(0.12\lambda_{wc} + 2.58\right)\exp\left[\left(-2882 + 14.126\lambda_{wc}\right)\left(\frac{1}{T} - \frac{1}{298.15}\right)\right]$	$m^2\ s^{-1}$	[132]
Water in gas	$D_{o,g}^{H_2O}$	$2.56 \times 10^{-5}\left(\frac{T}{307.15}\right)^{2.334}$	$m^2\ s^{-1}$	[21]
Water in Nafion®	$D_e^{H_2O}$	$\begin{cases} 3.10 \times 10^{-7}\lambda_{wc}\left[-1 + \exp\left(0.28\lambda_{wc}\right)\right]\exp\left(\frac{-2436}{T}\right) & \lambda_{wc} \leq 3 \\ 4.17 \times 10^{-8}\lambda_{wc}\left[1 + 161\exp\left(-\lambda_{wc}\right)\right]\exp\left(\frac{-2436}{T}\right) & \lambda_{wc} > 3 \end{cases}$	$m^2\ s^{-1}$	[118]
Oxygen in gas	$D_{o,g}^{O_2}$	$1.775 \times 10^{-5}\left(\frac{T}{328.15}\right)^{1.823}$	$m^2\ s^{-1}$	[55]
Oxygen in water	$D_{o,l}^{O_2}$	$6.748 \times 10^{-15}\left(\frac{T}{\rho_l \nu_l}\right)$	$m^2\ s^{-1}$	[133, 134]
Oxygen in Nafion®	$D_{o,e}^{O_2}$	$10^{-10}\left[\lambda_{wc}^{0.708}\left(1.3926\exp\left(\frac{T - 273.15}{106.65}\right) - 1.6461\right) + 5.2\right]$	$m^2\ s^{-1}$	[135]
Henry's Law coefficient				
Methanol in Water	k_{H,H_2O}^{MeOH}	$2.2\bar{R}T\exp\left[5200\left(\frac{1}{T} - \frac{1}{298.15}\right)\right]$	-	[126]
Oxygen in Water	$k_{H,H_2O}^{O_2}$	$7.518 \times 10^{-6}\bar{R}T\exp\left(\frac{498}{T}\right)$	-	[136]
Oxygen in Nafion®	$k_{H,e}^{O_2}$	$\frac{\bar{R}T}{0.11552}\exp\left[\left(\frac{666}{T}\right) - 0.0302\lambda_{wc} - 14.1\right]$	-	[135]
Reversible Cell Voltage				
Overall Cell Voltage	V_{rev}	$1.213 - (1.4 \times 10^{-4})(T - 298.15)$	V	[137]
Anode Half-Cell Voltage	U_a^0	-0.03	V	[137]
Cathode Half-Cell Voltage	U_c^0	1.24	V	[137]
Coefficient of Electro-osmotic Drag (EOD)				
Coefficient of EOD of Water	$n_d^{H_2O}$	$\begin{cases} \left(\frac{\lambda_{wc} - 14}{8}\right)\left(n_{d,ref}^{H_2O} - 1\right) + 1 & \lambda_{wc} \geq 14 \\ 1 & \lambda_{wc} < 14 \end{cases}$	-	[41]
Reference Coefficient of EOD	$n_{d,ref}^{H_2O}$	$1.6767 + 0.0155 \cdot (T - 273.15) + (8.9074 \times 10^{-5}) \cdot (T - 273.15)^2$	-	[41]
Proton Conductivity				
AM and CM	$\kappa_{o,AM}$ and $\kappa_{o,CM}$	$(0.5139\lambda_{wc} - 0.326)\exp\left[-1268\left(\frac{1}{T} - \frac{1}{303.15}\right)\right]$	$S\ m^{-1}$	[138]
FEC	$\kappa_{o,FEC}$	38.65	$S\ m^{-1}$	[127]
Methanol Oxidation Reaction Constant				
Anode and Cathode MOR	K_a and K_c	2.265×10^{-3}	$mol\ m^{-3}$	[24]
Reference Oxygen Concentration	$C_{ref}^{O_2}$	$0.21\frac{P}{\bar{R}T}$	$mol\ m^{-3}$	[52]

Table B.3: Fuel cell dimensions and material properties used in modeling study.

Parameter	Symbol	Value	Units	Reference
Length				
Cell	L_{cell}	50×10^{-3}	m	(measured)
Channel	$\bar{L}_{ch}$	0.147	m	(measured)
Active area of the cell	A	2.5×10^{-3}	m^2	(measured)
Thickness				
ABL and CBL	t_{ABL}, t_{CBL}	0.28×10^{-3}	m	(measured)
ACL and CCL	t_{ACL}, t_{CCL}	30×10^{-6}	m	(measured)
AM and CM	t_{AM}, t_{CM}	0.183×10^{-3}	m	(measured)
FEC	t_{FEC}	0.61×10^{-3}	m	(measured)
Channel	t_{ch}	1×10^{-3}	m	(measured)
Porosity				
ABL and CBL	ε_{ABL}, ε_{CBL}	0.60	-	[139]
FEC	ε_{FEC}	0.47	-	(measured)
Permeability				
ABL and CBL	K_{ABL}, K_{CBL}	1.0×10^{-12}	m^2	[140]
ACL and CCL	K_{ACL}, K_{CCL}	1.0×10^{-13}	m^2	[67]
AM and CM	K_{AM}, K_{CM}	2.0×10^{-18}	m^2	[85]
FEC	K_{FEC}	2.0×10^{-12}	m^2	(estimated)
Tortuosity				
ABL, CBL, FEC	τ_{ABL}, τ_{CBL}, τ_{FEC}	1.5	-	[85]
ACL, CCL	τ_{ACL}, τ_{CCL}	1.5	-	-
Contact Angle				
ABL, CBL	θ_c	110	degrees	[18]
FEC	θ_c	110	degrees	(estimated)
ACL, CCL	θ_c	95	degrees	[67]
Electric Conductivity				
ABL, CBL	$\kappa_{o,ABL}$, $\kappa_{o,CBL}$	8884	S m^{-1}	[36]
ACL, CCL	$\kappa_{o,ACL}$, $\kappa_{o,CCL}$	8884	S m^{-1}	-
AM, CM and FEC	$\kappa_{o,AM}$, $\kappa_{o,CM}$, $\kappa_{o,FEC}$	0	S m^{-1}	-
Agglomerate Radius				
ACL, CCL	$R_{agg,ACL}$, $R_{agg,CCL}$	200	nm	(estimated)
Electrolyte Volume Fraction				
ACL, CCL	$\varepsilon_{e,nuc,ACL}$, $\varepsilon_{e,nuc,CCL}$	0.5	-	(assumed)

Appendix C

Derivation of the Analytical Liquid Saturation Distribution for Test Case 1

This appendix provides the derivation of the analytical liquid saturation jump solution used for Test Case 1, discussed in Section 3.1. The approach used to develop this analytical solution is based off of the derivation presented in Pasaogullari and Wang [141], and Das *et al.* [142]. In this test case, liquid water enters a domain with two mating material layers of dissimilar porous properties, yielding a liquid saturation jump. It is assumed that the liquid mass flux into the domain is constant and known at $x = 0$, and there is a constant liquid saturation at $x = t_1 + t_2 = L$; as defined in Figure 3.2. The advantage of these boundary conditions, is that it allows for the same form of analytical solution to be used in all layers. As such, only the boundary value changes for each layer.

In the case where both domains have very low liquid saturations, or a negligible gaseous velocity compared to the liquid velocity, then the gaseous pressure gradient can be neglected, yielding $\nabla P_l \approx -\nabla P_{cap}$. Substituting this expression into Darcy's Law, the liquid phase continuity equation takes the form shown below, for the case where its source term is zero.

$$\nabla \cdot \left[\frac{K k_{rl}}{\nu_l} (\nabla P_{cap}) \right] = 0 \tag{C.1}$$

If each material layer's porous properties are assumed to be constant, this causes $\nabla\psi = 0$. Therefore, expanding the capillary pressure gradient using the chain rule, the continuity equation takes the form shown below.

$$\nabla \cdot \left[\frac{K k_{rl} \psi}{\nu_l} \frac{\partial J}{\partial s} (\nabla s) \right] = 0 \tag{C.2}$$

Substituting the relationships for k_{rl} and $\partial J/\partial s$ for a hydrophobic media, from Table 2.1, into the continuity equation, Equation C.2 now takes the form shown below.

$$\nabla \cdot \left[\frac{K\psi}{\nu_l} s^3 (3.789 s^2 - 4.24 s + 1.417)(\nabla s) \right] = 0 \tag{C.3}$$

From here, Equation C.3 can be integrated across each layer to obtain the 1D liquid saturation distribution, shown below for Layers 1 and 2, respectively. In these equations, $D = K\psi/\nu_l$, whereas $f\big|_{t_1}$ and $f\big|_L$ represent the value of the left hand side of Equations C.4a and C.4b at $x = t_1$ and L, respectively. As can be seen from the equations below, it is simply the value of f that changes between layers, allowing for a simple analytical test case.

$$s^4 \left(0.63150 s^2 - 0.84800 s + 0.35425 \right) = f\big|_{t_1} + \frac{(\rho u)_l}{D_1} (x - t_1) \tag{C.4a}$$

$$s^4 \left(0.63150 s^2 - 0.84800 s + 0.35425 \right) = f\big|_{L} + \frac{(\rho u)_l}{D_2} (x - L) \tag{C.4b}$$

Since the liquid saturation at $x = L$ is known, $f\big|_L$ can be readily calculated, allowing the liquid saturation and P_{cap} distributions to be determined anywhere within Layer 2. To solve for $f\big|_{t_1}$, the P_{cap} of both materials at $x = t_1$ are equated to give the equation shown below, after the substitution of the Young-Laplace equation. Here, the subscripts $-$ and $+$ represent the position left and right of the interface, respectively.

$$J_- = \frac{\psi_+}{\psi_-} J_+ \tag{C.5}$$

This equation can be solved through a root-finding procedure, such as the Newton-Raphson method. From here, Layer 1's newly obtained liquid saturation can be used as the boundary value for Equation C.4a, to complete the analytical liquid saturation profile.

Appendix D

Derivation of the Analytical Single Phase Model for Test Case 2

In this appendix, an analytical single phase model is derived for the FE-DMFC, which is subsequently used to qualitatively verify the accuracy of the numerical model in Test Case 2, in Section 3.2. The analytical model extends Colpan *et al.*'s 1D model [35], by accounting for the convective mode of transport in all material layers, and the back-pressure within the FEC. This appendix begins with an overview of the assumptions made in this analytical model, and then moves to the derivation of the mass, momentum and and species equations.

D.1 Modeling Assumptions

Many of the assumptions made in this model are similar to those mentioned in Colpan *et al.*'s model [35], as well as the ones discussed in Section 2.2. A list of the assumptions in this analytical model are listed below. The computational domain for this model is the same as the one used for the numerical model, shown in Figure 2.1.

1. The fuel cell operates under steady state and isothermal conditions
2. All fluids are ideal and exist in equilibrium with one another
3. Each media is homogeneous and isotropic

4. Only the liquid phase is assumed to be present within the anode, membranes and FEC, while only gas is present within the CBL.

5. The membranes are taken to be fully hydrated at all times and impermeable to the gaseous state

6. The CLs are considered as an interface

7. All crossed over methanol is fully consumed at the cathode catalyst layer

8. The velocity profile within the FEC is uniform

D.2 Mass and Momentum Transport

Since the CLs are infinitely thin and each layer has uniform material properties, the momentum equation (Darcy's Law) can be substituted into the continuity equation to provide the form shown below.

$$\frac{d^2P}{dx^2} = 0 \tag{D.1}$$

Equation D.1 can be solved analytically for the pressure and mass flux distributions, as shown below. Here, C_1 and C_2 are integration constants, and x is the thickness-wise position.

$$P = C_1 x + C_2 \tag{D.2a}$$

$$\rho u = -\frac{K}{\nu} \cdot C_1 \tag{D.2b}$$

Within the FEC, the solution is now two-dimensional, due to the net addition or removal of mass within this layer. However, to simplify the problem, the y-component of the continuity equation is discretized across the FEC's inlet and outlet, represented by the subscripts *in* and *out*, as shown below.

$$\frac{\partial(\rho v)}{\partial y} \approx \frac{(\rho v)_{in} - (\rho v)_{out}}{L} \tag{D.3}$$

Here, $(\rho v)_{in}$ is known, whereas $(\rho v)_{out}$ is determined from the discretized momentum equation, shown below. Here, P_{FEC} is the pressure at the FEC outlet and $L/2$ represents the distance from the FEC outlet and the control volume's node.

$$(\rho v)_{out} = -\frac{K}{\nu}\left(\frac{P - P_{FEC}}{L/2}\right) \tag{D.4}$$

Substituting, Equations D.3 and D.4 into the 2D form of Equation D.1, the continuity equation now takes the form shown below.

$$-\frac{d^2P}{dx^2} - \frac{1}{L^2}P + \frac{1}{L^2}\left[(\rho v)_{in}\frac{\nu L}{K} - 2P_{FEC}\right] = 0 \tag{D.5}$$

Solving this equation analytically for the pressure and mass flux profiles yields Equations D.6a and D.6b, shown below.

$$P = C_3 \exp\left(\frac{x}{L}\right) + C_4 \exp\left(-\frac{x}{L}\right) - \left[\frac{\nu L}{K}(\rho u)_{in} + P_{FEC}\right] \tag{D.6a}$$

$$\rho u = -\frac{K}{\nu L}\left[C_3 \exp\left(\frac{x}{L}\right) - C_4 \exp\left(-\frac{x}{L}\right)\right] \tag{D.6b}$$

D.3 Methanol Transport

To model the methanol transport, the convective-diffusion equation, given by Equation 2.4, is applied with $S_{gen}^{MeOH} = S_{trans}^{MeOH} = 0$ in the BLs and membranes. In all layers, the diffusion coefficients are constant and the velocity is averaged across the layer's thickness, this allows

for the analytical solution shown below.

$$C_l^{MeOH} = K_1 + K_2 \exp\left(\frac{\bar{u}^{MeOH} x}{D_l^{MeOH}}\right) \tag{D.7a}$$

$$\dot{N}''^{MeOH} = \bar{u}^{MeOH} K_1 \tag{D.7b}$$

Within the membranes and in the FEC, the velocity is composed of both the bulk velocity and the electro-osmotic drag induced velocity, as shown below.

$$\bar{u}^{MeOH} = \bar{u} + \varepsilon_e \frac{n_d^{H_2O}}{C_l^{H_2O}} \frac{i}{F} \tag{D.8}$$

Following the same approach as shown in Equation D.3, the convective flux in the y-direction can be simplified to give the methanol transport equation shown in Equation D.9. The FEC outlet velocity is calculated from the mean value calculated from Equation D.4.

$$- D_l^{MeOH} \frac{d^2 C_l^{MeOH}}{dx^2} + \bar{u}^{MeOH} \frac{dC_l^{MeOH}}{dx} - \frac{(\rho v)_{out}}{\rho_l L} C_l^{MeOH} = 0 \tag{D.9}$$

The analytical methanol concentration and flux equations are given by Equations D.10a and D.10b, respectively.

$$C_l^{MeOH} = K_5 \exp(Ax) - K_6 \exp(Bx) \tag{D.10a}$$

$$\dot{N}''^{MeOH} = -K_5 (A D_l^{MeOH} - \bar{u}^{MeOH}) \exp(Ax) - K_6 (B D_l^{MeOH} - \bar{u}^{MeOH}) \exp(Bx) \tag{D.10b}$$

Here A and B are given by the following equations.

$$A = \frac{\bar{u}^{MeOH} + \sqrt{(\bar{u}^{MeOH})^2 - (4 D_l^{MeOH} v / L)}}{2 D_l^{MeOH}} \tag{D.11a}$$

$$B = \frac{\bar{u}^{MeOH} - \sqrt{(\bar{u}^{MeOH})^2 - (4 D_l^{MeOH} v / L)}}{2 D_l^{MeOH}} \tag{D.11b}$$

D.4 Oxygen Transport

Since this model assumes that oxygen is confined to the CBL, the oxygen concentration profile is thus much easier to solve than the other governing equations. The analytical solution to the convective-diffusion equation is shown below, where there is a known consumption flux at the CBL-CCL interface and known inlet concentration at the CBL-CAC interface.

$$C_g^{O_2} = C_{g,in}^{O_2} \exp\left(\frac{\bar{u}}{D_g^{O_2}}\left(x - t_{CBL}\right)\right) + \frac{S_{gen}^{O_2}}{\bar{u}}\left[1 - \exp\left(\frac{\bar{u}}{D_g^{O_2}}\left(x - t_{CBL}\right)\right)\right] \tag{D.12}$$

D.5 Electrochemical Relationships

The electrochemical relationships are the same ones as derived in Section 2.4.2. Since the charge transport equations are not considered, the activation polarization can be readily isolated as shown below for the MOR and ORR respectively. For simplicity, the agglomerate correction factor is approximated as oxygen's dissolution into the electrolyte phase, $\xi \approx k_{H,e}^{O_2}$. This is equivalent to the case where, $R_{agg} \to 0$ and $n_{agg} \to \infty$.

$$\eta_a = \frac{\bar{R}T}{\alpha_a F} \ln\left[\frac{i}{i_{a,ref}}\left(1 - \frac{K_a}{C_l^{MeOH}}\frac{i}{i_{a,ref}}\right)^{-1}\right] \tag{D.13a}$$

$$\eta_c = \frac{\bar{R}T}{\alpha_c F} \ln\left[\frac{i + i_{xover}}{i_{c,ref}}\frac{C_{g,ref}^{O_2}}{C_g^{O_2}\xi}\right] \tag{D.13b}$$

The methanol crossover flux is calculated at the CM-CBL interface, using Equation D.7b and the crossover current density is calculate from the methanol crossover flux, using the relationship shown below.

$$i_{xover} = 6F\dot{N}_{xover}^{\prime\prime MeOH} \tag{D.14}$$

To calculate the cell voltage, V_{cell}, all loss mechanisms are subtracted from the reversible

cell voltage, V_{rev}, as shown below. The Ohmic resistance, given by the last set of terms in this equation, is composed of the contact resistance of the fuel cell assembly and the ionic resistance of the membranes and FEC.

$$V_{cell} = V_{rev} - \eta_a - \eta_c - i\left(R_{contact} + \sum_i \int_0^{t_i} \frac{dx}{\kappa_i}\right) \tag{D.15}$$

D.6 Solution Procedure

In this model, each variable is assumed to be continuous, and continuity is enforced at all material interfaces. To solve the governing equations, the following procedure is applied.

1. The mass, momentum and methanol transport equations are all solved simultaneously through Gaussian elimination for a specified operating current density.

2. The oxygen concentration profile and electrochemical relationships are then determined to calculate the corresponding cell voltage.

3. If $V_{cell} > 0.1$ V, the operating current density is incremented and the whole process is repeated.

Appendix E

Uncertainty Analysis for Test Case 3

This appendix details the uncertainty analysis used to analyze the experimental data presented in Section 3.3 for Test Case 3. This analysis applies the guidelines presented in the ANSI/ASME PTC 19.1 standard [143].

E.1 Uncertainty Quantification

Following the ANSI/ASME PTC 19.1 standard, a measurement's true value of some variable x, is assumed to have an averaged measurement of x, given by $\bar{x}$, along with some overall uncertainty, U_x, as shown below.

$$x = \bar{x} \pm U_x \tag{E.1}$$

The measured $\bar{x}$, is calculated as the pooled arithmetic mean of all the measurements, as shown below. Here, x_i are the individual measurements of x, and N is the total number of measurements of x.

$$\bar{x} = \frac{\sum_i x_i}{N} \tag{E.2}$$

The overall uncertainty, U_x, is assumed to be separable into a bias (B) and a random (R) uncertainty, where the bias error is considered to be a constant offset of a measurement's true

value, and the random error is considered to be any deviations between repeated measurements that cannot be controlled. The combined uncertainty is calculated using Equation E.3, where $t_{\nu,95\%}$ is the Student t-Distribution factor for ν degrees of freedom at 95% confidence. In this work, the degrees of freedom is estimated as $\nu = N - 1$.

$$U_x = \sqrt{B_x^2 + \left(t_{\nu,95\%} R_x\right)^2} \tag{E.3}$$

To estimate the overall B_x, the root-sum-squared approach is applied, yielding the final form shown in Equation E.4. It is assumed that B_x is composed of contributions from a series of elemental errors, denoted by ϕ_i. The partial derivative, in Equation E.4, is known as the sensitivity index of the measurement x, which is multiplied by the bias error of variable ϕ_i, denoted by B_{ϕ_i}.

$$B_x = \sqrt{\sum_i \left(\frac{\partial x}{\partial \phi_i} B_{\phi_i}\right)^2} \tag{E.4}$$

In this study, the sensitivity indicies were estimated at each data point, by taking the slope between different polarization curves. For example, the slope of the local current density between two polarization curves that were collected at two different cell temperatures, with all else remaining the same, would provide the current density's sensitivity index with respect to temperature ($\partial i / \partial T$). Since each sensitivity indices's value was different when a backward, central and forward differencing approach was used, the approach which gave the highest sensitivity index was used in the analysis to provide more conservative results. This approach was applied for all other parameters.

To estimate the overall R_x, a statistical approach is applied, where the standard deviation of all repeated experiments are calculated, as shown below.

$$R_x = \sqrt{\frac{\sum_i \left(x_i - \bar{x}\right)^2}{N - 1}} \tag{E.5}$$

E.2 Elemental Errors

To estimate the bias error in a given measurement, the ANSI/ASME PTC 19.1 standard suggests that the elemental sources of error should be identified and quantified. In the case of the cell voltage and current density measurements, the examined elemental sources of error included: the cell temperature, the clamping torque, the anode, cathode and FEC flow rates and concentrations, and the half-MEAs' active areas [80, 81].

E.2.1 Error Estimation in the Temperature Control System

The bias error of the fuel cell's temperature was estimated to be a combination of the thermocouple's and temperature controller's uncertainty, as well as the thermocouple's positioning. The bias error associated with the thermocouple and the temperature controller were determined to be ±2.2°C and ±0.5°C, respectively. Whereas, the bias error associated with the thermocouple's positioning was estimated through a thermal conduction analysis through a graphite plate, with the thermocouple positioned at the midpoint, as given by the equation below. The corresponding temperature difference was estimated to be ±0.2°C. From this analysis, the estimated temperature bias is ±2.3°C; determined from the root-sum-squared of the mentioned biases.

$$\Delta T = \frac{\dot{q}(t/2)}{kA} \tag{E.6}$$

E.2.2 Error Estimation in the Fluid Control System

The methanol and sulfuric acid flow rates were calibrated volumetrically. The graduated cylinder used in this process is taken to have a bias of ±0.50 cm^3, whereas the parallax error is conservatively estimated to be ±0.15 cm^3. The parallax error was estimated by performing an experiment where the location of the meniscus is observed from different eye level positions. The relative change in apparent height of the meniscus was used to provide

the estimated parallax error. Combining these errors yields a bias of ± 0.52 cm^3 min^{-1}. The bias error of the air flow rate was estimated from the manufacturer's specifications. Following the same procedure as previously discussed, 2 graduations were estimated for the parallax error. The bias uncertainty was thus estimated to be 64 cm^3 min^{-1} for the air flow rate.

E.2.3 Error Estimation in the Fluid Concentrations

The methanol and sulfuric acid concentrations were measured volumetrically, using the equation shown below. The subscripts i and f correspond to the initial and final states of dilution, the superscript k refers to either methanol or sulfuric acid, and V corresponds to the measured volume. The effects of evaporation are neglected and the concentrations are assumed to be constant during the whole length of the experiments.

$$C_{l,f}^{k} = C_{l,i}^{k} \frac{V_i}{V_f} \tag{E.7}$$

To estimate the overall bias of the final fluid concentration, the Taylor series approach is used, yielding the result shown below.

$$\frac{B_{C_l^k}}{C_l^k} = \sqrt{\left(\frac{B_{C_{l,i}^k}}{C_{l,i}^k}\right)^2 + \left(\frac{B_{V_i}}{V_i}\right)^2 + \left(\frac{B_{V_f}}{V_f}\right)^2} \tag{E.8}$$

Since the uncertainty of the initial concentration was found to be more than 2 orders of magnitude smaller than the initial and final volumes, this source of error was deemed negligible. From the volumetric flasks used to form the dilutions, the bias was reported to be ± 0.5 cm^3, whereas the bias caused by parallax is estimated to be ± 0.15 cm^3, as before. Thus, for a 2 dm^3 solution of methanol and sulfuric acid, both at their baseline concentrations, their bias uncertainties were estimated to be ± 6.5 mol m^{-3} and ± 4.7 mol m^{-3}, respectively.

E.2.4 Error Estimation in the Active Area

Since different tested fuel cells can each have slightly different active areas, this will cause the measured current density to be erroneous. As such, the accuracy of the active area's size was determined by a ruler, which was assumed to have a bias error of ± 0.5 mm. For a 5 cm square active area, this provided a bias of ± 0.4 cm^2.

E.2.5 Summarized Bias Uncertainty

Once each elemental bias error is quantified, the sensitivity index is estimated from the experimental data, and maximum of each sensitivity index is chosen to represent the uncertainty analysis. With the inclusion of this bias, along with others, it was found that the current density and cell voltage biases were ± 84.6 A m^{-2} and ± 14.5 mV respectively.

E.3 Overall Uncertainty

To provide representative results on the repeatability of the experimental data, the averaged polarization curves from each experimental run and for each tested MEA is presented in Figure E.1 for the case with 4000 mol m^{-3} inlet methanol concentration. From this plot, it was found that MEA 1 and 2 both had very comparable performance, whereas MEA 3's performance was comparatively higher. Although the sample size of the tested MEAs is small, it is difficult to discern if this is due to the random uncertainty in the experimental setup, heat pressing procedure or if MEA 3 simply had higher performance due to a higher catalyst loading or lower internal resistance. In any case, all three sets of data are included in the final averaged results to produce to the most representative data possible. The spread in the experimental data seems to be comparable to those published in Casalegno *et al.*'s work [144].

Applying the bias and random uncertainties, discussed earlier, the overall uncertainties for the operating conditions used in Test Case 3 are presented in Figures E.2 and E.3. From these

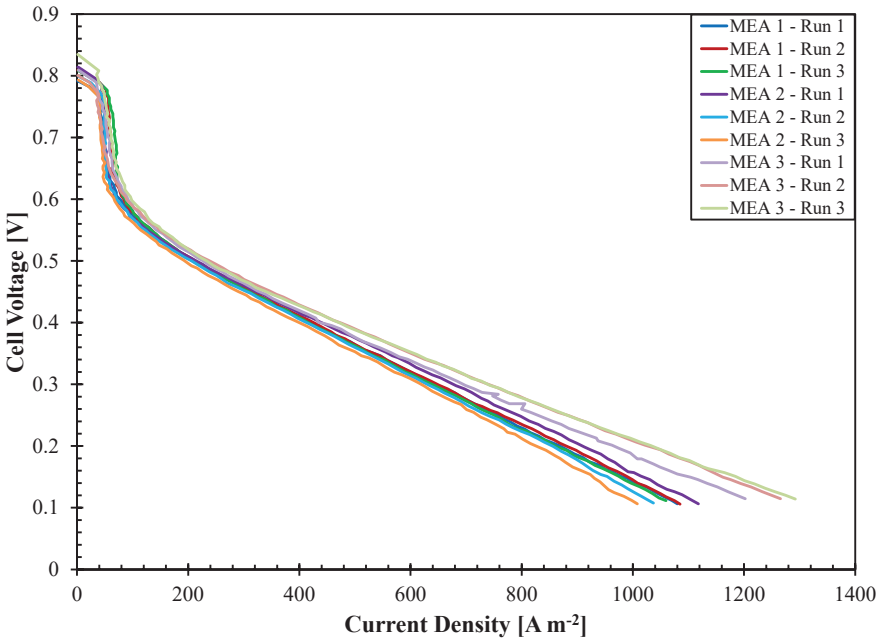

Figure E.1: Averaged polarization curves during each experimental run and tested MEA, with 4000 mol m^{-3} inlet methanol concentration. Each polarization curve presented here is the average of the 5 polarization curves collected during that experimental run.

results, it was found that the average uncertainties were ± 87 A m^{-2} and ± 18 mV. Generally, the uncertainty in the current density grew with increasing current density, whereas the cell voltage displayed the opposite trend. For a summary of the lowest, average and highest uncertainties, please refer to Table 3.4.

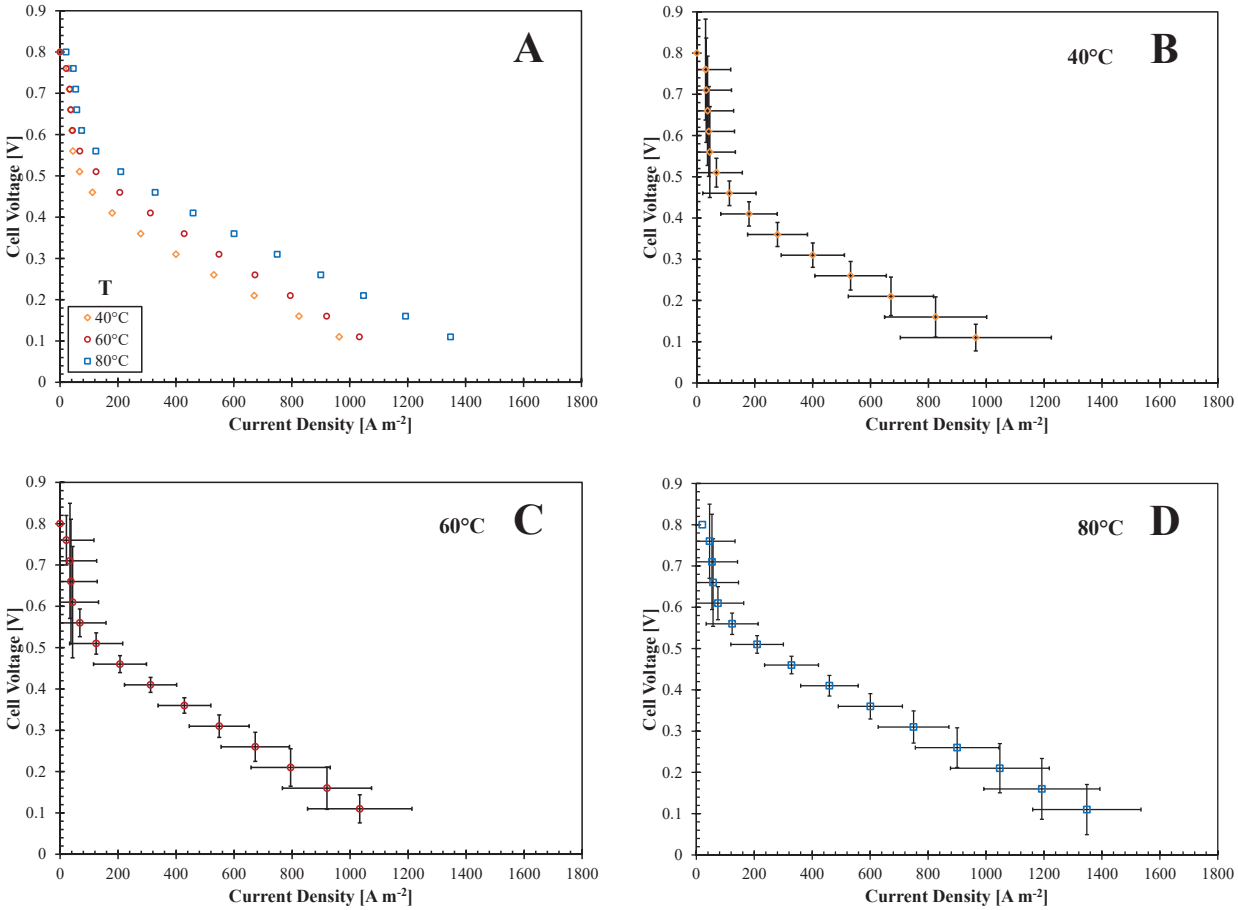

Figure E.2: Compiled experimental data with the uncertainties for polarization curves at cell temperatures of 40°C, 60°C and 80°C.

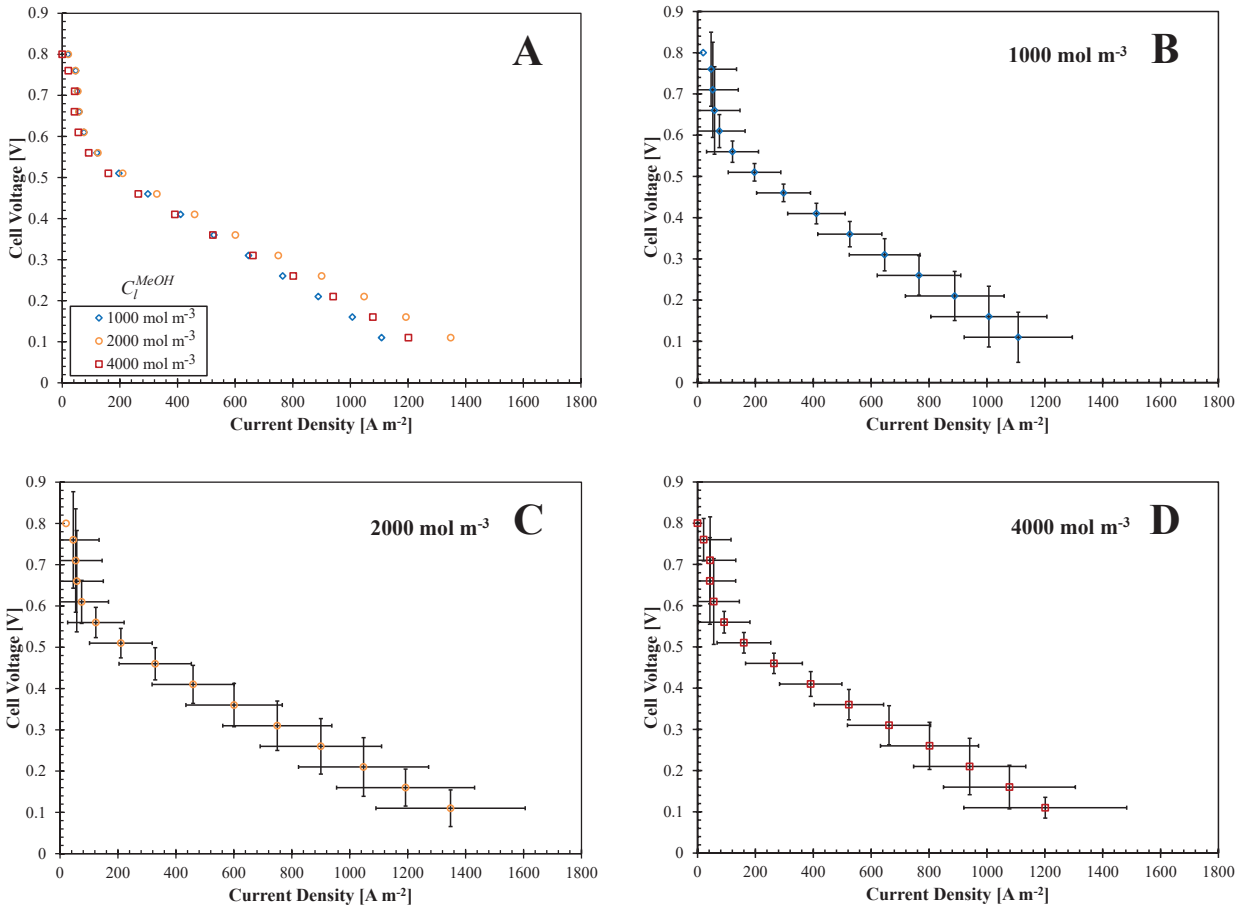

Figure E.3: Compiled experimental data with the uncertainties for polarization curves at inlet methanol concentrations of 1000 mol m^{-3}, 2000 mol m^{-3} and 4000 mol m^{-3}.

Appendix F

Model Calibration Procedure

The FE-DMFC model was calibrated to experimental data through use of an in-house optimization routine that applied the coordinate search method [145]. The objective of this calibration procedure was to minimize the difference between the experimental and modeled current densities at each cell voltage, as given by Equation F.1. Here, the superscripts *exp* and *model* correspond to the current density obtained from the experiments and model, respectively. The subscript i represents the i^{th} data point across all data sets.

$$\Theta = \min \left\{ \sum_i \frac{\left| i_i^{model} - i_i^{exp} \right|}{i_i^{exp}} \right\} \tag{F.1}$$

In this appendix, the coordinate search method, surrogate model, and the procedure used to perform the optimization routine are provided.

F.1 Coordinate Search Method

The coordinate search method begins by assuming a set point for each calibration parameter. Each calibration parameter is then individually incremented forward and then backward from the assumed set point. On each iteration, the objective function (Equation F.1) is evaluated using the surrogate model, which will be discussed in Section F.2, and the measured experimental data. Out of the calibrations variables, the location that provided

the lowest value of Θ becomes the new set point. In the event where the calibration parameters' set point provides the lowest Θ, the increment of each variable is decreased by half [145].

A challenge with the proposed optimization routine, is that the search path could become trapped in a local minimum rather than a global minimum. This leads to the issue where more than one combination of calibration parameters could yield an 'optimal' solution. This seems to be a common occurrence when calibrating fuel cell models [146–148]. The method applied to help circumvent this issue was to rerun the surrogate model for many random start locations. The converged position that provided the lowest value of Θ was used as the new set of calibration variables for the numerical simulations. It should be noted however that even if the surrogate model finds a global minimum, there is no guarantee that this optimum is indicative of the fuel cell's actual measured values. As such, a local minimum was deemed sufficient as long as the model's behaviour was consistent with those observed across multiple experimental datasets.

F.2 Surrogate Model

To reduce the number of numerical simulations needed and the time required to calibrate the model, a surrogate model was applied to help find the optimal calibration parameter values. This surrogate model consisted the evaluation of the equation shown below.

$$V_{cell} = V_{rev} - \eta_a - |\eta_c| - iR \tag{F.2}$$

The anode and cathode activation polarizations (η_a and η_c respectively), and the overall ohmic resistance (R) are calculated using the same equations as discussed previously in Sections 2.4.2 and 2.5. These equations are summarized below. The values for each non-calibration parameter was obtained from the numerical simulations and were assumed to be constant for a given V_{cell}. However, the calibration parameters are allowed to vary as needed

as dictated by the coordinate search method, discussed in Section F.1. These calibration parameters are discussed next section.

$$\eta_a = \frac{\bar{R}T}{\alpha_a F} \ln \left[\frac{i}{i_{a,ref}} \left(1 - \frac{K_a}{C^{MeOH}} \frac{i}{i_{a,ref}} \right)^{-1} \right] \tag{F.3a}$$

$$\eta_c = \frac{\bar{R}T}{\alpha_c F} \ln \left[\frac{i + i_{xover}}{i_{c,ref}} \frac{C^{O_2}_{g,ref}}{C^{O_2}_{g} \xi} \right] \tag{F.3b}$$

$$R = R_{contact} + \sum_i \left(\int_0^{t_i} \frac{dx}{\kappa_i} \right) \tag{F.3c}$$

F.3 Calibration Procedure

The calibration parameters consisted of the most uncertain parameters, these included: the electrical contact resistance ($R_{contact}$), and anode and cathode: charge transfer coefficients (α_a and α_c) and reference exchange current densities ($i_{a,ref}$ and $i_{c,ref}$). Lower and upper limits were enforced on these calibration parameters to ensure physically meaningful solutions and were chosen based on the range of values most frequently observed in literature. These limits and the final converged results are shown in Table F.1. The activation energy for the anode and cathode reactions are taken to be 35.57 and 73.20 kJ mol^{-1} respectively [21].

The calibration procedure begins with an assumed start location for each calibration parameter and a full numerical simulation is then run for each experimental dataset. Once complete, all values from the numerical simulation are used to evaluate, Equations F.2 and F.3. During this process, all parameters are held constant, with the exception of the calibration parameters, which are determined through the coordinate search approach as discussed in Section F.1. Once an optimal location is determined, the updated calibration parameters are used to for the full numerical simulation, to repeat the process. This process

Table F.1: Values of calibration parameters used in this work and their constraints enforced during the calibration process.

Symbol	Present Work	Lower Limit	Upper Limit	Units
Transfer Coefficient				
α_a	0.5000	0.2390 [21]	0.5000 [139]	–
α_c	1.0000	0.5000 [139]	1.0000 [54]	–
Exchange Current Density				
$i_{a,ref}$	0.6961	0.55×10^{-6} [149]	216 [150]	A m^{-2}
$i_{c,ref}$	0.0163	0.33×10^{-6} [149]	917 [150]	A m^{-2}
Contact Resistance				
$R_{contact}$	8×10^{-5}	0	8×10^{-5} [149]	Ω m^2

continues until the value of each calibration parameter changes by $< 10^{-4}$ between two evaluations of the full numerical simulation.